Title

The Development and Investigation of Cobalt Catalysts for the Chemical Transformations Related to Artificial Photosynthesis

Author

Ahn, Hyun Seo

Publication Date

2013

Peer reviewed|Thesis/dissertation

The Development and Investigation of Cobalt Catalysts for the Chemical Transformations Related to Artificial Photosynthesis

by

Hyun Seo Ahn

A dissertation submitted in partial satisfaction of the
requirements for the degree of
Doctor of Philosophy
in
Chemistry
in the
Graduate Division
of the
University of California, Berkeley

Committee in charge:
Professor T. Don Tilley, Chair
Professor Jeffrey R. Long
Professor Alexander Katz

Fall 2013

Abstract

The Development and Investigation of Cobalt Catalysts for the Chemical Transformations Related to Artificial Photosynthesis

by

Hyun Seo Ahn

Doctor of Philosophy in Chemistry

University of California, Berkeley

Professor T. Don Tilley

Chapter 1. Small domains of cobalt on silica (CoSBA) were prepared by the reaction of $Co[N(SiMe_3)_2]_2$ and SBA-15, resulting in a range of surface structures as the cobalt loading varied from 0.27 to 5.11 wt%. X-ray absorption spectroscopy (XAS) was employed to characterize these surface structures, which range from single-site cobalt atoms to small clusters of Co_3O_4. The CoSBA materials exhibit photochemical water oxidation catalysis, revealing distinct catalytic activities associated with characteristic types of surface structures that are dominant in particular concentration regimes. The catalytic turnover frequency for water oxidation of an isolated single-site cobalt atom (0.0143 s^{-1}) is much greater than that observed for a surface atom of a small cluster Co_3O_4 on silica (0.0006 s^{-1}). The CoSBA catalysts were recyclable for more than seven catalytic cycles (> 200 turnovers) with additional sacrificial oxidant, and no leaching of cobalt was observed. Post-catalytic analysis of CoSBA by XAS revealed that the cobalt atoms were partially oxidized to Co^{3+}, without exhibiting significant surface migration and aggregation of cobalt atoms.

Chapter 2. Single-site cobalt atoms on various oxide surfaces (TiO_2, MgO, SBA-15, AlPO, and Y-Zeolite) were prepared and evaluated as water oxidation catalysts. Superior catalytic rates were observed for cobalt sites on basic supporting oxides (TiO_2 and MgO) relative to those on acidic oxides (Y-Zeolite, AlPo, and SiO_2). Per-atom turnover frequencies of ca. 0.04 s^{-1} were achieved, giving initial rates 100 times greater than a surface atom of a Co_3O_4 nanoparticle. No correlation was observed between catalytic rates and oxygen atom affinities of the supporting oxides.

Chapter 3. Cobalt metaphosphate $Co(PO_3)_2$ nanoparticles are prepared via the *thermolytic molecular precursor* (TMP) method. A Ni foam electrode decorated with $Co(PO_3)_2$ nanoparticles is evaluated as an anode for water oxidation electrocatalysis in pH 6.4 phosphate-buffered water. Catalytic onset occurs at an overpotential of ca. 310 mV, which is 100 mV lower than that observed for Co_3O_4 nanoparticles, with a comparable surface area under identical conditions. A per-metal turnover frequency (TOF) of 0.10 - 0.21 s^{-1} is observed at η = 440 mV, which is comparable to the highest rate reported for a first-row metal heterogeneous catalyst. Post-

catalytic characterization of the catalyst resting state by XPS and Raman spectroscopy reveals that surface rearrangement occurs, resulting in an oxide-like surface overlayer.

Chapter 4. Linear trimetallic $Co^{III}/Co^{II}/Co^{III}$ cobalt complexes with bridging acyl-alkoxy ligands are electrocatalysts for the reduction of tosic acid in acetonitrile. The $–OCMe_2CH_2COMe$ complex appears to operate homogeneously, and at an onset overpotential of only 25 mV. A turnover frequency of ca. 80 s^{-1} was observed at an overptotential of 150 mV.

For my family and loved ones

The Development and Investigation of Cobalt Catalysts for the Chemical Transformations Related to Artificial Photosynthesis

Table of Contents

Acknowledgements

I had a vacation before starting graduate school here in Berkeley. It was a long and relaxing vacation, during which I dreamt of maturing into a scientist with a solid foundation. Five and a half years later I face my old self again, who asks me whether I have become that scientist. I fear to answer: a reason why I continue my training as a chemist. But I am at the end of my Ph. D. program thanks to many people who helped me through this endurance race. One of many lessons learned in graduate school is that not many achievements are earned without the aid of others.

I would like to first thank my parents: Keumsook Baek and Tae Young Ahn, they are my foundation and they have selflessly provided me with all my needs. I thank my dearest grandmother JeongRyoul who passed away when I was a child but lives in my heart. I thank my soulmate Jaran for her presence by my side and her patience with me during the hard times. I also would like to thank all my other family members for their emotional support when I was in need. Thanks to you this day was possible.

I have to thank my advisor T. Don Tilley for all of his support. Don is one of the nicest persons I came to know at Berkeley, and he provided me with a warm and comfortable environment to pursue science. All of his valuable advice will be cherished as I continue my career in science. Rosemary complemented the effort, keeping everything organized and providing wise life-related advices. I thank my undergraduate advisor Robert E. Synovec for allowing me to learn the research environment and giving me a foundation for scientific thinking.

The Tilley group has been good to me over the years. Of course I will have to first thank Tim Davenport for being an excellent student-to-student mentor and a good friend. I am lucky to have very talented fellow graduate students in the same graduating class: Miriam Bowring and Mark Lipke. I thank Rick for being a wonderful friend and a kind person to discuss chemistry and life. I wish best of luck in their research endeavors to the current fourth years: Kurt, Andy, Mike, and Allegra. I thank Micah for his voluntary editing service that contributed directly to this dissertation, and I also wish him luck in his research. I hope James can find his way through the tough project he has and further our understanding of surface catalysis (and maybe homo/heterogeneous tandem catalysis). Former Tilley Postdocs DoYoung and Changwon have been great mentors and coworkers. I thank them for their help while in the group and I wish to see them again soon.

I thank my godfather Christopher Lee. Chris, I followed your steps from Seattle to Berkeley. Please pray for me so that I can be a better scientist. Thanks to my friends and mature scientists: Ilhyung Lee, Amy Twite, Katie Lutker, and Jongwoo Lim. So many names flash through my head. I can't name each and every one of you, but thank you so much for all the support you have given me. Thank you again.

Dec. 2013, Hyun Seo Ahn

Chapter 1. Photocatalytic Water Oxidation by Very Small Cobalt Domains on a Silica Surface

Adapted with permission from Ahn, H. S.; Yano, J.; Tilley, T. D. *Energy Environ. Sci.* **2013**, 6, 3080.

Introduction

Many of the current research activities directed toward development of new sources of renewable energy focus on the photogeneration of chemical fuels (artificial photosynthesis).[1] This interest is heavily centered on the use of water as a feedstock, and low-energy pathways for its activation and conversion. In particular, the oxidative half-reaction of water to oxygen is envisioned as a potentially useful source of protons and electrons that might be used in reductive, fuel-producing reactions (e.g., the direct reduction of protons to H_2, or CO_2 reductions to hydrocarbons).[1] This has motivated considerable research directed toward discovery of efficient water oxidation catalysts,[2-20] and in particular catalysts based on abundant first-row transition metals.[10-20] Viable catalysts are generally considered to be heterogeneous and long-lived under conditions that provide turnover frequencies (TOFs) consistent with high conversion of the incident sunlight.[21]

A number of heterogeneous, first-row transition metal catalysts for the oxidation of water have been investigated,[10-20] with a particular emphasis on catalysts based on cobalt. These cobalt catalysts have taken various forms, including nanoparticles and thin films,[10-20] and the CoP_i catalyst described by Nocera and coworkers has drawn considerable attention.[10-11] In comparing various cobalt-based catalysts, it is useful to determine activity under a given set of experimental conditions, on a per-cobalt basis. Thus, a useful benchmark for cobalt-based catalysts would be the inherent activity associated with the smallest functional unit for the catalyst. With this information in hand, it should be possible to probe the influence of local environments (e.g. the nature of the support material) on catalyst efficiency. Lymar and coworkers have recently described the activity of small $[Co(OH)_2]_x$ clusters (ca. 25 Co atoms, ~2 nm) supported on silica.[19] For the CoP_i catalyst, the active site is believed to be composed of fused cobalt oxo cubane units containing ca. 7 Co atoms.[11] However, the inherent water oxidation activity for heterogeneous cobalt clusters smaller than 2 nm, or more importantly that of a single cobalt atom on a surface, remains undetermined. It is therefore important to investigate the catalytic activities of very small cobalt species on a surface, from isolated, single-site cobalt centers to clusters of several atoms, in order to better understand the structural requirements for water oxidation by heterogeneous cobalt species.

This contribution describes an investigation of the activities of small-domain cobalt species supported on mesoporous silica surfaces (SBA-15). Several surface concentration regimes are characterized by dominant surface structures, ranging from isolated single cobalt centers to small clusters of Co_3O_4 (< 2 nm). Characteristic activities for catalytic water oxidation are associated with different surface concentration regimes, with the highest being exhibited by isolated cobalt centers. All of the catalyst samples displayed prolonged activity in pH 5.5-buffered water with no leaching of metal centers over 6 h.

Results and Discussion

Synthesis and characterization of CoSBA-15 samples. The high surface area (634 m^2 g^{-1}) SBA-15 silica material used to support cobalt species was prepared by a known procedure.[22] For introduction of single-site cobalt species, the bis(amido) complex $Co[N(SiMe_3)_2]_2$[23] was employed. The choice of this molecular precursor was based on the successful use of similar complexes of Mg,[24] Ti,[25] Fe,[26] and Nd[27] for introduction of silica-supported, single-site metal centers by Anwander and coworkers. The CoSBA-15 materials were prepared by allowing a suspension of SBA-15 to react with $Co[N(SiMe_3)_2]_2$ in hexanes, followed by filtration and washing of the resulting blue solids with hexanes and then calcination at 300 °C in air to remove residual organic material. Monitoring the surface functionalization reaction by ^1H NMR spectroscopy demonstrated that this process results in elimination of 0.9(1) equiv of $HN(SiMe_3)_2$ per cobalt complex (δ = 0.082 ppm in C_6D_6, measured against a ferrocene internal standard). The grafting reactions were complete within 30 min, as evidenced by the absence of cobalt in the supernatant solution by inductively coupled plasma optical emission spectroscopy (ICP-OES). An observed decrease in the surface area of the materials after grafting (Figure 1) is similar to that observed for previously reported systems;[29-32] however, a lack of decrease in the pore size (Figure 1) suggests that the degree of silylation by $HN(SiMe_3)_2$ is minimal due to the short reaction times.[28] On the basis of these observations, it appears that the initial grafting procedure gives a mono-amido cobalt(II) species, such as the one shown in Scheme 1.

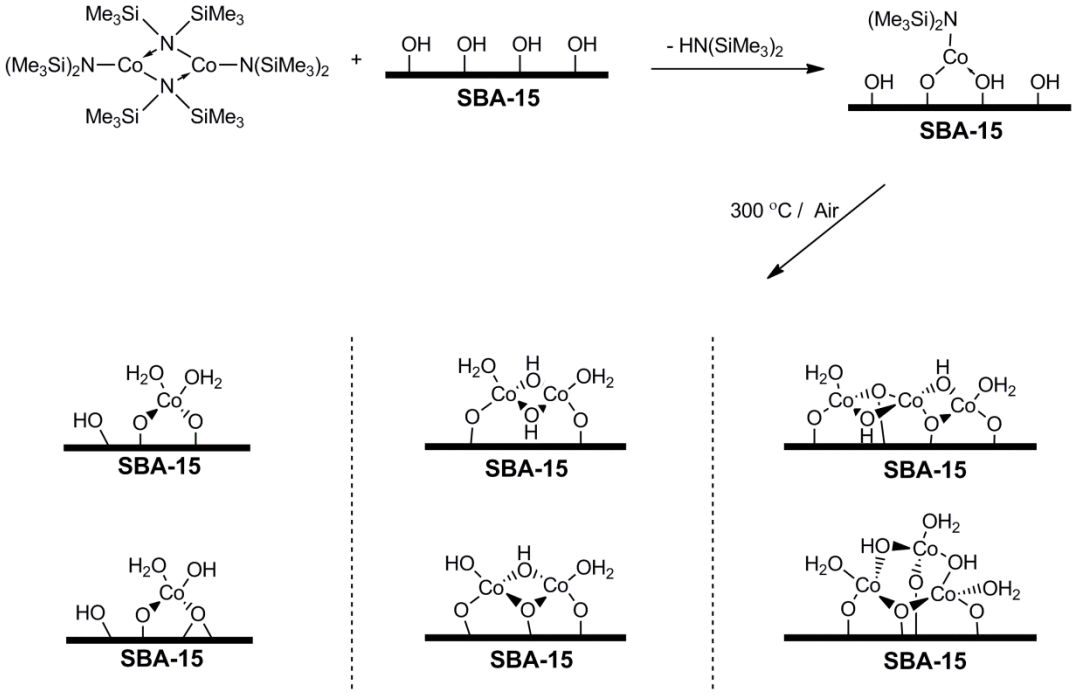

Scheme 1. Synthesis of CoSBA materials

Residual organic species were removed by calcination at 300 ℃ in air, to yield surface species closely related to the representative structures of Scheme 1. The all-inorganic nature of the CoSBA samples was verified by carbon and nitrogen elemental analyses (CHN found for CoSBA332: C, 0.10, H 0.90, N 0.06). After calcination of the grafted samples, losses in surface area with respect to the parent SBA-15 material were evident in all cases, with the highest decreases being associated with higher loadings (Figure 1). These losses of surface area can be largely attributed to blockage of the micropores in the SBA-15 framework, and have been commonly observed in similar systems.[24-27,29-32] No collapse of the ordered mesopores in SBA-15 was observed after cobalt grafting, as evidenced by the preserved average pore diameters (Figure 1) and by TEM images (Figure A8). The surface cobalt coverage was varied by control of the amount of cobalt precursor employed, to produce materials with cobalt wt % values of 0.27 (CoSBA027), 0.48 (CoSBA048), 1.06 (CoSBA106), 1.89 (CoSBA189), 2.33 (CoSBA233), 3.32 (CoSBA332), 4.16 (CoSBA416), and 5.11 (CoSBA511).

The cobalt surface species were characterized by a number of spectroscopic methods. Diffuse reflectance FTIR (DRFTIR) spectra reveal a diminished SiO-H vibration[29-32] at 3750 cm^{-1} in all samples after cobalt grafting, with the corresponding appearance of an Si-O-Co vibration[33] at 960 cm^{-1} (Figure A2). This indicates that the cobalt species are covalently bound to the silica surface *via* reactions at surface hydroxyl sites, to generate the Si-O-Co linkage. The coordination geometries of the cobalt species on CoSBA027, CoSBA048, CoSBA106, CoSBA189, CoSBA233, and CoSBA332 were probed by diffuse reflectance UV-vis spectroscopy (DRUV-vis), which indicated the presence of d-d transitions (λ_{max} = 530, 580, and 650 nm, Figure A3) consistent with cobalt(II) centers with pseudotetrahedral coordination environments.[34,35] The DRUV-vis spectra of CoSBA416 and CoSBA511 were distinctly different, in possessing a broad feature at 350 nm which is characteristic of Co_3O_4 domains (Figure A4).[36,37] The formation of Co_3O_4 in samples with higher cobalt loadings was expected due to the limited surface density of –OH sites on SBA-15 prior to reaction with the precursor (ca. 1.2 nm^{-2}, determined by a titration method described in the Appendix). The cobalt loading that corresponds to complete reaction of the surface –OH sites is 3.72 wt% cobalt. Thus, loadings above this value are expected to result in condensation of the surface cobalt species. Raman spectroscopy of the CoSBA samples corroborated the formation of Co_3O_4 spinel in CoSBA416 and CoSBA511. Raman features characteristic of cobalt oxide,[38] at 485, 505, and 691 cm^{-1}, were observed for CoSBA416 and CoSBA511, whereas the only peak observed for lower loadings was a broad feature at ca. 500 cm^{-1}, which may be assigned to a Co-O vibration (Figure A5).[33,38] The observed cobalt oxide domains were small, such that wide angle powder X-ray diffraction (pXRD) exhibited no discernible features.

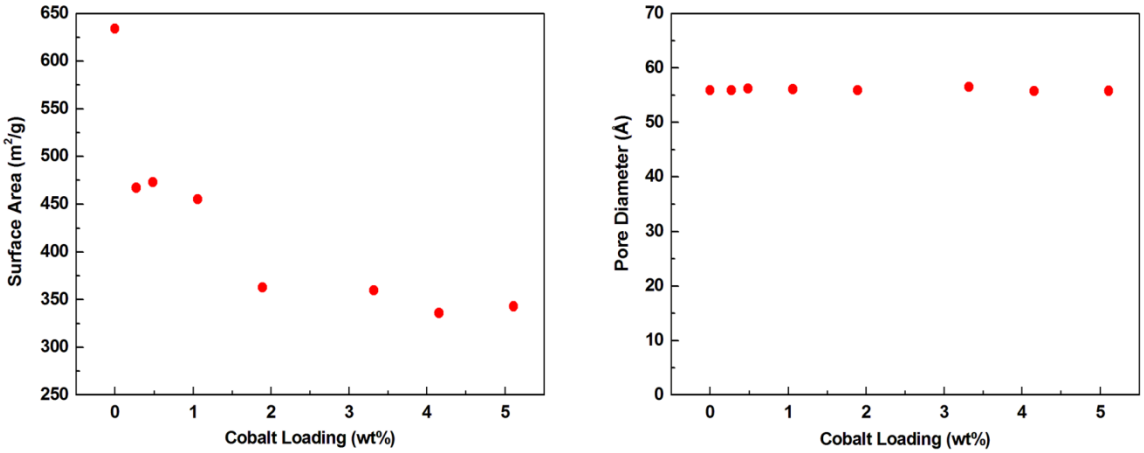

Figure 1. Gas adsorption surface area of CoSBA materials as a function of cobalt loading (left). Loss of surface area with increased loading was comparable to similar systems studied previously. The pore diameter did not change significantly with loading (right), indicating that the mesoporous structure of SBA-15 was intact after the grafting procedures.

X-ray absorption near edge structure (XANES) and extended X-ray absorption fine structure (EXAFS) spectroscopies were implemented to further investigate the oxidation states and local environments of the surface metal species. XANES spectra of the CoSBA-15 samples (Figure 2) exhibit a cobalt edge energy of ca. 7719.5 eV, suggesting an oxidation state for the surface cobalt atoms of $2+$[39-41] and corroborating the results from DRUV-vis spectroscopy. A pre-edge feature (1s to 3d transition) in the XANES spectra of the samples with lower coverages (CoSBA027, CoSBA048, CoSBA106, CoSBA189, and CoSBA332; Figure A6) was observed at ca. 7709 eV, suggesting that the cobalt centers are in tetrahedral coordination environments. However, CoSBA511 revealed an edge position at ca. 7723.2 eV, indicating a presence of more oxidized Co form, and the spectrum is similar to that observed for Co_3O_4 (Figure 2). This is consistent with evidence provided by other spectroscopies (*vide supra*), which suggest the presence of Co_3O_4 in CoSBA511. An inhomogeneous distribution of surface sites was observed in the CoSBA511 sample by XANES and EXAFS, due to the large excess of cobalt atoms compared to the available Si-OH grafting sites (*vide supra*). Small domains of fully formed Co_3O_4 were observed as displayed in the XANES spectrum in Figure 2, whereas XANES spectra similar to that of CoSBA048 (or other low concentration samples) were also obtained from different parts of the CoSBA511 sample (see Figure A7). This finding, along with the lack of an observable pXRD pattern, suggests that very small domains of Co_3O_4 are present in CoSBA511, such that it is reasonable to assume that much of the cobalt is exposed on the material's surface, and is available to participate in catalytic reactions. No blockage of SBA-15 channels was observed and no particles bigger than the resolution of the transmission electron microscopy (TEM) instrument (ca. 2 nm) were present in SBA-15 channels (Figure A8).

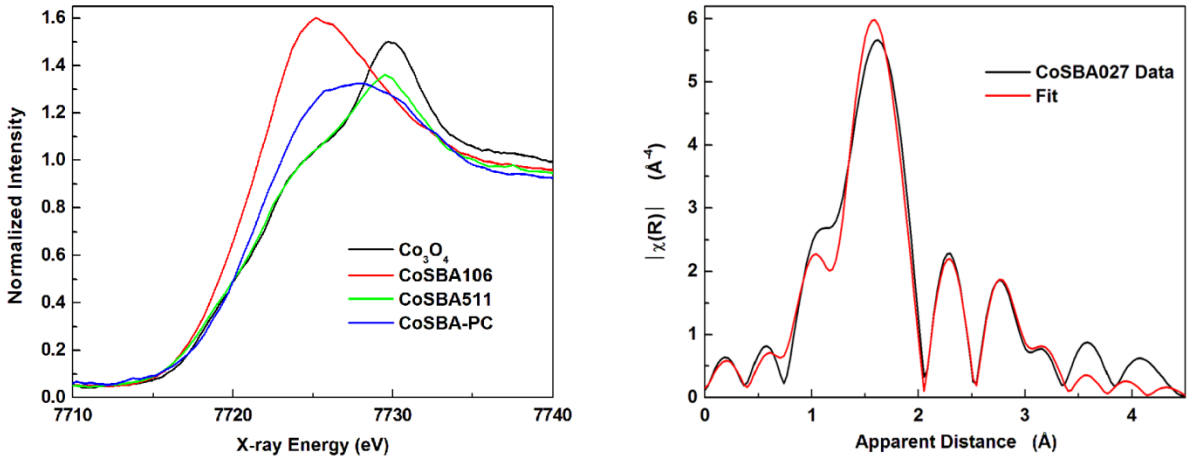

Figure 2. XANES (left) and EXAFS (right) spectra of selected CoSBA samples. CoSBA-PC denotes CoSBA106 after catalysis cycles. XANES of low loading CoSBA samples exhibited an edge energy suggestive of Co^{2+}. Similar XANES spectra were recorded for CoSBA511 and Co_3O_4, indicating that cobalt oxide has formed in CoSBA511. The EXAFS spectrum of CoSBA027 displays an excellent fit against the model, supporting the surface structures depicted in Scheme 1.

The local coordination environments of the cobalt centers in CoSBA-15 samples were investigated using EXAFS spectroscopy, which indicates that the cobalt coordination environments in CoSBA027 and CoSBA048 are very similar, as are those of CoSBA189 and CoSBA332. Overall, among eight CoSBA samples, four distinct types of surface species were identified by the EXAFS data. Surface structure types **A** (CoSBA027, CoSBA048), **B** (CoSBA106), and **C** (CoSBA189, CoSBA233, CoSBA332) are distinguished by the average number of Co-O-Co interactions obtained by the EXAFS fits, as depicted by the representative structures of Scheme 1, and the presence of Co_3O_4 (in CoSBA416 and CoSBA511) was established by the spectroscopic information described above (see the Appendix for details of the EXAFS fitting). Note that the structures depicted in Scheme 1 are consistent with the fittings of EXAFS data, and are representative of the types of species that would possess a given nuclearity. Three fitting paths (Co-O, Co-O-Co, and Co-O-Si) were employed in modeling the data, comparable to the EXAFS modeling work by Frei and coworkers on structurally similar systems on SBA-15.[47-49] Structure type **A** exhibited a Co-O-Co coordination number (CN) of 0.4, indicating a predominance of isolated, single-site cobalt centers on the surface. It is reasonable to observe a non-zero value for the number of Co-O-Co interactions at even the lowest loadings, since it is well known that some of the silica surface hydroxyl groups exist in pairs, or in closely associated groups.[42-44] Surface structure type **B** can best be described as a μ_2-oxy or μ_2-hydroxy dicobalt species, exhibiting a Co-O-Co coordination number (CN) of 1.2 at an interaction distance of ca. 2.89 Å, similar to that seen in Co_3O_4 or molecular compounds with the same structural moiety.[45,46] The formation of small clusters of structure type **C** is indicated by a calculated Co-O-Co CN of 2.3 as depicted in Scheme 1. For all structures, the best fits were

obtained with a Co-O CN of 5 and a Co-O-Si CN of 2, supporting a bipodal surface anchoring of each cobalt atom on SBA-15. The observed Co-O (ca. 2.05 Å) and Co-O-Si (ca. 3.25 Å) distances are consistent throughout all samples, with only slight variations (see the Appendix for detailed fit results, bond distances, and coordination numbers).

Photochemically driven water oxidation catalysis with CoSBA catalysts. Light-driven water-oxidation reactions were observed for the series of CoSBA materials described above as catalysts. A buffered aqueous solution at pH 5.5-5.6 ($NaHCO_3/Na_2SiF_6$) was used, and $Na_2S_2O_8$ was employed as a sacrificial electron acceptor.[3,12] A 488 nm laser with a power output of 260 mW and a focused beam diameter of 0.5 cm was used as the light source. Real-time oxygen monitoring was conducted in the headspace of the reactor using a fluorescence-based oxygen probe. The same amount of catalyst (40 mg) was used for each experiment.

All of the samples in the CoSBA series were observed to be active water oxidation catalysts, with varying activities (oxygen evolution as a function of time is shown in Figures 3 and A9). Oxygen evolution was not observed when SBA-15 without cobalt was subjected to catalytic conditions (Figure A9). To ensure that the detected O_2 was derived from water, an ^{18}O labeling experiment was performed using CoSBA048 as the catalyst. The water was enriched with 5.5 vol% of $H_2{}^{18}O$ (0.9 mL of 97 % $H_2{}^{18}O$ in 16 mL total volume), resulting in a theoretical $^{16}O_2$: $^{16}O^{18}O$: $^{18}O_2$ distribution of 89.3:10.4:0.3 (Table A1). The experimental oxygen distribution measured by mass spectrometry was 89.8:10.2:trace (the $^{18}O_2$ was detected with poor S/N and the peak integration was not reliable; see Figure A15 and Table A1). Thus, the measured isotopic distribution indicates that water was the sole source of oxygen in the reaction. A similar distribution was observed when CoSBA233 was used as the catalyst.

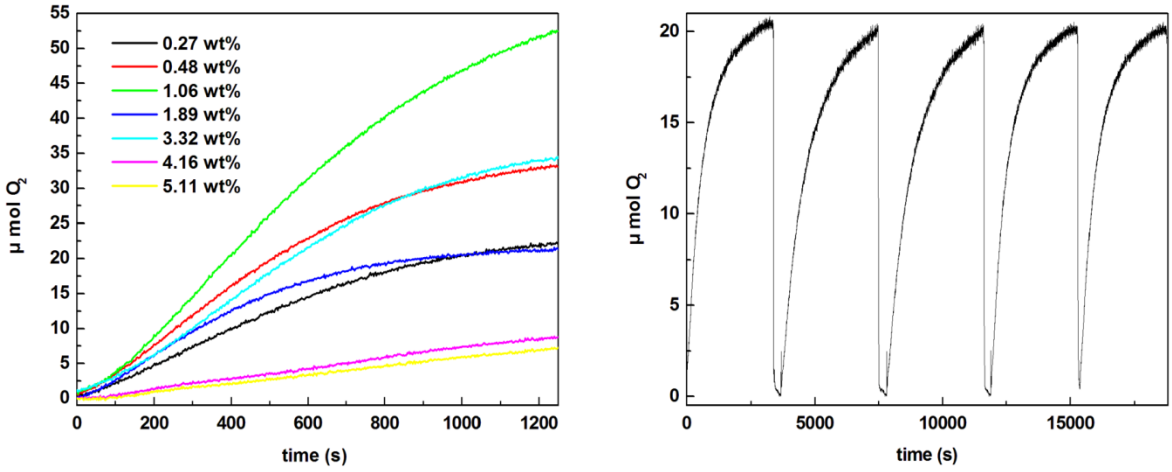

Figure 3. Oxygen evolution of CoSBA catalysts over time (left). An increase in product formation was observed with increasing surface concentration to CoSBA106, with a decrease in the overall product formation transitioning to CoSBA189, suggesting the involvement of a different catalytic species (Structure **C**, Scheme 1). The CoSBA catalysts exhibited recyclability with further additions of oxidant, and catalysis continued for more than 6 hours and 200 turnovers (right).

The spinel oxide of cobalt (Co_3O_4) is a well known water oxidation catalyst, and has been extensively studied in the past.[12-15] Thus, it is not surprising to observe catalytic activities for CoSBA416 and CoSBA511, for which small domains of Co_3O_4 exist on the SBA-15 surface. Relevant work by Frei and coworkers has demonstrated comparable catalytic activity for cobalt oxide nanorods grown inside the mesopores of SBA-15.[12] However, determinations of activities for very small cobalt domains (from single-site cobalt to clusters of several cobalt atoms) have not been reported.

On the basis of a kinetic study on water oxidation by the aqueous cobalt ion, Sutin and coworkers proposed a mechanism involving the cobalt-catalyzed, two-electron oxidation of water to H_2O_2, followed by rapid oxidation of H_2O_2 to oxygen by the available oxidant (Ru^{3+}).[16] This work suggests that a single, surface cobalt species may function as a water oxidation catalyst. Consistent with this, the smallest surface domains of cobalt are associated with the highest initial turnover frequency (TOF_i), with the material possessing the highest loading of single-site cobalt centers (structure type **A**) exhibiting the highest TOF_i value of 0.0143 s^{-1} Co^{-1} (51.5 h^{-1} Co^{-1}, Figure 4). This TOF_i of ca. 0.01 s^{-1} Co^{-1} is comparable to the rates reported for highly active first-row metal oxide-type materials.[12] It is important to note that nearly all cobalt centers in CoSBA likely participate in catalysis, whereas only a fraction of metal atoms are active in the outer-most layer of metal oxide-type catalysts. Thus, catalytic metal centers are economically utilized in the CoSBA catalysts, though they are less compact on the surface.

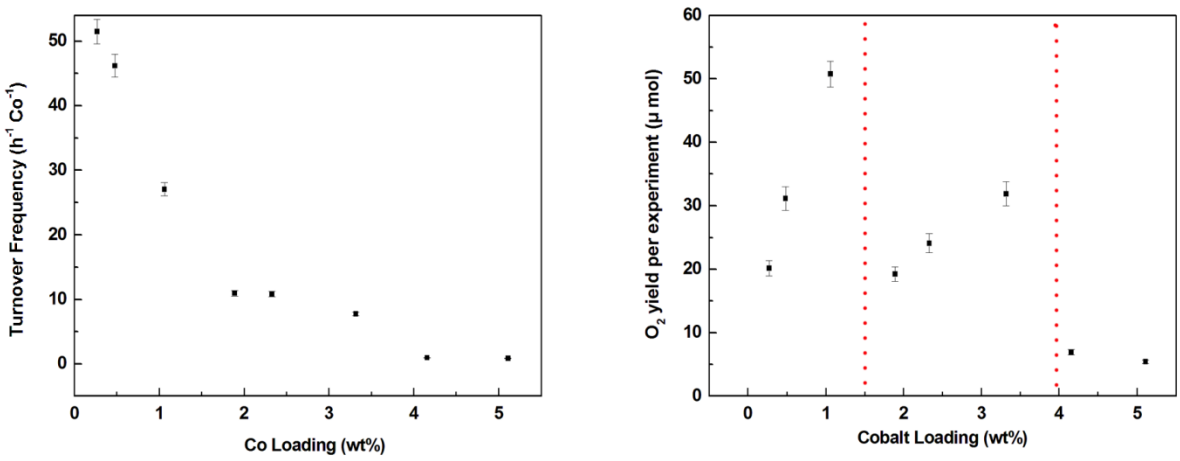

Figure 4. TOF_i plotted against increasing cobalt loading (left). TOF_i values decrease with increasing surface concentration. Examination of the total amount of O_2 produced as a function of cobalt loading (right) suggests the presence of distinct catalyst loading regimes, which correspond to the predominance of different surfaces species for each concentration range (Scheme 1). The amount of sacrificial oxidant in each experiment (151 µmol) corresponds to a theoretical maximum production of 75 µmol of O_2.

These results reveal that, on a per-metal basis, surface single-site cobalt centers are more active for water oxidation than the surface cobalt sites of cobalt oxide. The TOF_i of 0.0143 s^{-1} Co^{-1} observed for CoSBA027 is orders of magnitude greater than that estimated for a surface atom of bulk Co_3O_4 (0.0006 s^{-1} Co^{-1}, ref. 12; 0.0002 s^{-1} Co^{-1} from this work), and greater than that of many other nanostructured systems.[12] Water oxidation by these CoSBA materials continued for more than 6 h and 200 turnovers with added amounts of $Na_2S_2O_8$ (Figure 3). No leaching of cobalt ions into solution was observed by ICP-OES analysis of the post-catalytic solutions. Observation of similar TOF_i values after seven subsequent runs with the same catalyst (but with freshly added oxidant) suggests that the CoSBA catalysts are stable and long-lived under these reaction conditions. It is worth noting that the TOF_i values reported here are effective values subject to being influenced by diffusion of the $Ru(bpy)_3^{2+}$ sensitizer and the oxidant ($S_2O_8^{2-}$) and therefore cannot be directly compared to TOF values in other works obtained by different means. Internal comparisons amongst CoSBA samples of different surface nuclearities, however, are meaningful because all samples are evaluated under the same conditions.

Initial rates for water oxidation with the CoSBA catalysts, expressed in per-metal turnovers per hour, were plotted as a function of cobalt loading on the surface (Figure 4; see the Appendix for detailed turnover frequency calculations). Distinct rate behaviors for various structural types (**A**, **B**, **C**, and Co_3O_4) were observed, with single-site cobalt exhibiting the greatest catalytic activity. As shown in Figure 4, there is a clear decrease in TOF_i with increased cobalt loading. Samples of the same structural type displayed similar TOF_i values (CoSBA027 and CoSBA048 in **A** and CoSBA189, CoSBA233, and CoSBA332 in **C**; see Figure 4). The trends displayed by the loading vs. TOF_i plot (Figure 4) suggest that the various structural types

observed by EXAFS (structure types **A**, **B**, **C**, and Co_3O_4) are associated with a different water oxidation catalytic activity.

Figure 4 also presents a plot of the total O_2 yield as a function of catalyst loading (with the sacrificial oxidant as limiting reagent). This data suggests that the different types of surface species mentioned above (**A**, **B**, **C**, Co_3O_4) exhibit markedly different catalytic behaviors. Thus, the yield of O_2 increases with surface cobalt concentration through the regime associated with structure types **A** and **B**. A discontinuity in this plot appears to be associated with the structural change from structure type **B** to **C**, and then again from structure type **C** to Co_3O_4. It is proposed that the observed discontinuities are associated with changes in the predominant active species, since catalyst degradation is not observed over the course of these measurements (*vide supra*). The observed initial rates for the active sites for these catalysts span a wide range of TOF_i values: as high as 51 h^{-1} Co^{-1} for CoSBA027 (single-site) to as low as 1 h^{-1} Co^{-1} for CoSBA511 (domains of Co_3O_4).

The amount of sacrificial oxidant used (151 μmol) corresponds to the theoretical maximum O_2 yield of 75 μmol for each experiment. The maximum sacrificial oxidant efficiency (mol O_2 produced divided by the theoretical maximum) obtained was 68 % for CoSBA106, which is significantly higher than that observed for a similar system by Frei and coworkers (< 51 %).[12] This difference is attributed to a higher TOF associated with well-dispersed CoSBA catalysts, as compared to nanostructured Co_3O_4. Note that a yield of 68% is relatively high considering the competing oxidative degradation of the $Ru(bpy)_3^{2+}$ sensitizer.[3]

Structural characterization of the post-catalysis CoSBA samples. Post-catalysis samples were analyzed by X-ray absorption spectroscopy in order to probe changes in oxidation states and coordination environments. From the XANES spectrum in Figure 2, the post-catalysis samples are more oxidized than the pre-catalysis samples, both of which contain Co^{2+} and Co^{3+}. The edge energy of the post-catalysis sample was ca. 7721.2 eV, higher than that of the pre-catalysis samples and lower than that of Co_3O_4 (7723.2 eV), suggesting that the ratio of Co^{2+} to Co^{3+} is lower than 1:2.

Fitting of the EXAFS data for post catalytic CoSBA106 also suggests the presence of a more oxidized material after catalysis, in that a shorter average Co-O bond distance of ca. 1.96 Å is observed, as well as an increase in the Co-O CN to 5.6 (see the Appendix). The Co-O-Co and Co-O-Si bond lengths were also reduced to 2.66 Å and 2.77 Å, respectively. However, Co-O-Co and Co-O-Si CNs did not significantly change after catalysis, and were found to be 1.7 and 2, respectively. The observed preservation of Co-O-Co and Co-O-Si CNs indicates that despite some changes in the average cobalt oxidation state, after many catalytic turnovers there is minimal surface restructuring and/or agglomeration of cobalt species.

Conclusions

The investigation described above presents a molecular approach to the creation of highly dispersed cobalt centers on a silica support. The high dispersion of the surface-bound cobalt, especially at low loadings, has allowed determination of the water oxidation activity, under the specific conditions employed, for structures approaching, and including, the single-cobalt-atom regime. These catalysts exhibit significant stabilities that allow comparisons of observed catalytic activities as a function of cobalt surface densities. On the basis of efficiencies for O_2 production, the catalysts seem to be differentiated into ranges of loadings corresponding to differences in predominant surface structures. This work has allowed an estimate for the TOF_i value associated with a mono-cobalt species on the surface of silica of ca. 0.01-0.02 s^{-1}.

Similar ultra-low surface concentration regimes may exist with other metals on surfaces, and thus parallel studies on first-row metals of interest (Mn, Ni, etc) are planned. Variations in the support material, for structurally similar and chemically distinct surface species, are also of interest. Additionally, the CoSBA systems described here are amenable to post-synthetic surface modifications,[29-30] which should allow further investigations on the influence of a reaction center's local environment on catalytic performance.

Experimental

General. All manipulations were conducted under an inert nitrogen atmosphere using standard Schlenk techniques or a Vacuum Atmospheres drybox, unless otherwise stated. Chemicals were purchased from Aldrich and used as received. Dry, oxygen free solvents were used throughout. The compound $Co[N(SiMe_3)_2]_2$[23] and mesoporous SBA-15[22] were synthesized as reported in the literature. Nitrogen adsorption isotherms were obtained using a Quantachrome Autosorb 1, with samples outgassed at 120 ℃ for at least 20 h prior to data collection. The BET method was used for surface area determinations, and the BJH method was used for pore size distribution calculations.[50-51] Carbon, hydrogen, and nitrogen elemental analyses were performed at the College of Chemistry microanalysis laboratory at the University of California, Berkeley. DR-FTIR spectra were obtained on a Thermo Nicolet 6700 FTIR spectrometer. The DRUV-Vis spectra were acquired using a Perkin-Elmer Lambda 9 spectrometer equipped with a 60 mm integrating sphere, a slit width of 4 nm, and at a collection speed of 120 nm/min. Samples were run using MgO as a reference background. Powder X-ray diffraction (PXRD) patterns were recorded on a Bruker D-8 GADDS X-ray diffractometer using Co Kα radiation (λ = 1.7902 Å). The pH measurements were conducted using a Thermo Orion 2 star pH meter. Transmission electron microscopy (TEM) was carried out on a Philips Tecnai 12 transmission electron microscope operating at 200 kV. Raman experiments were performed on an epi-illumination confocal Raman microscope (LabRam HR, Horiba Jobin, Yvon) with a HeNe laser (1 mW) at 633 nm as an excitation source. Inductively coupled plasma optical emission spectroscopy (ICP-OES) for cobalt ion detection in post catalytic solutions was performed on a Perkin-Elmer ICP-OES Optima 7000 DV (detection limit for Co ions: 0.25 ppb). Standard solutions were purchased from Perkin-Elmer and used as received. Heat treatments were conducted in a Lindberg 1200 ℃ three-zone furnace. Solution ^{1}H NMR spectra were recorded at 300 MHz using a Bruker AV-300 spectrometer. Chemical shifts for ^{1}H NMR spectra were referenced internally to the residual solvent proton signal relative to tetramethylsilane. A Stanford Research Systems residual gas analyzer 300 was used for the detection of evolved gases in the ^{18}O isotopic labeling experiments.

Syntheses of CoSBA materials. In a typical synthesis, $Co[N(SiMe_3)_2]_2$ (32 mg, 84 μmol) in 25 mL of hexanes was added to a hexanes suspension of SBA-15 (1 g in 25 mL). The green solution of $Co[N(SiMe_3)_2]_2$ instantaneously turned light blue as it came in contact with SBA-15. The resulting solution was stirred under nitrogen for 0.5 h, to yield a light blue solid and a clear supernatant. The CoSBA material was then washed thoroughly with hexanes and air dried. The dried material was then calcined under flowing air (110 cc/min) to 300 ℃ for 6 h to remove residual organics.

X-ray Absorption Spectroscopy (XAS) data collection. The combination of XANES/EXAFS spectra were collected at BL 10.3.2 in the Advanced Light Source (ALS) at LBNL, and at BL 7-

3 at the Stanford Synchrotron Radiation Lightsource (SSRL). At the ALS, the synchrotron ring operated at 1.9 GeV at a 500 mA beam current. Energy resolution of the focused incoming X-rays at BL 10.3.2 was achieved using a Si(111) double-crystal monochromator. Fluoresence spectra were collected with a 7-element Ge detector, and transmission spectra were obtained with a I_1 ion chamber filled with N_2 gas. An incident X-ray beam of 0.1 mm (H) x 0.02 mm (V) dimensions was used for the XANES and EXAFS experiments. At SSRL, the electron energy was set at 3.0 GeV with an average current of 450 mA. A Si(220) double-crystal monochromater was used. Spectra were collected in fluorescence mode in a chamber filled with N_2 gas. Energy calibrations are based on the rising edge energy of Co foil at 7709.0 eV (ALS) and at 7709.5 eV (SSRL). Each spectrum is the average of $6-9$ scans. All measurements were done at room temperature.

Water oxidation catalysis experiments and oxygen detection. Light-driven water-oxidation reactions were performed in buffered water at pH 5.5-5.6 ($NaHCO_3/Na_2SiF_6$) employing $Na_2S_2O_8$ as a sacrificial electron acceptor. The sensitizer used for the experiments was $[Ru(bpy)_3]Cl_2$. Water was degassed to remove oxygen, by bubbling nitrogen through it for 1 h prior to experiments. A gas-tight glass cell with an internal volume of 37.6 mL was used. In a typical experiment, 40 mg of catalyst was used in 15 mL of buffered water along with 18 mg of $[Ru(bpy)_3]Cl_2$, 100 mg of Na_2SO_4 and 36 mg of $Na_2S_2O_8$. A 488 nm laser with a power output of 260 mW, focused at a beam diameter of 0.5 cm, was used as the light source. The head-space oxygen concentration was monitored in real time by a multi-frequency fluorescence oxygen probe (Ocean Optics FOSPOR-R). The oxygen probe was freshly calibrated prior to being used in an experiment by a five-point calibration method at the following oxygen concentrations (vol. %) in helium: 0, 1.68, 3.62, 6.38, and 20.

References

(1) Gray, H. B. *Nat. Chem.* **2009**, 1, 7.
(2) Romain, S.; Vigara, L.; Llobet, A. *Acc. Chem. Res.* **2009**, 42, 1944.
(3) Youngblood, W. J.; Lee, S.-H. A.; Maeda, K.; Mallouk, T. E. *Acc. Chem. Res.* **2009**, 42, 1966.
(4) Duan, L.; Bozoglian, F.; Mandal, S.; Stewart, B.; Privalov, T.; Llobet, A.; Sun, L. *Nat. Chem.* **2012**, 4, 418.
(5) Xu, Y.; Fisher, A.; Duan, L.; Tong, L.; Gabrielsson, E.; Å kermark, B.; Sun, L. *Angew. Chem. Int. Ed.* **2010**, 49, 8934.
(6) Tong, L.; Duan, L.; Xu, Y.; Privalov, T.; Sun, L. *Angew. Chem. Int. Ed.* **2011**, 50, 445.
(7) Blakemore, J. D.; Schley, N. D.; Balcells, D.; Hull, J. F.; Olack, G. W.; Incarvito, C. D.; Eisenstein, O.; Brudvig, G. W.; Crabtree, R. H. *J. Am. Chem. Soc.* **2010**, 132, 16017.
(8) Hong, D.; Yamada, Y.; Nagatomi, T.; Takai, Y.; Fukuzumi, S. *J. Am. Chem. Soc.* **2012**, 134, 19572.
(9) Chen, Z. F.; Concepcion, J. J.; Jurss, J. W.; Meyer, T. J. *J. Am. Chem. Soc.* **2009**, 131, 15580.
(10) Kanan, M. W.; Nocera, D. G. *Science* **2008,** 321, 1072.
(11) Kanan, M. W.; Yano, J.; Surendranath, Y.; Dincă, M.; Yachandra, V. K.; Nocera, D. G. *J. Am. Chem. Soc.* **2010**, 132, 13692.
(12) Jiao, F.; Frei, H.; *Angew. Chem. Int. Ed.* **2009**, 48, 1841.
(13) Dau, H.; Christian, L.; Reier, T.; Risch, M.; Roggan, S.; Strasser, P. *ChemCatChem* **2010**, 2, 724.
(14) Esswein, A. J.; McMurdo, M. J.; Ross, P. N.; Bell, A. T.; Tilley, T. D. *J. Phys. Chem. C* **2009**, 113, 15068.
(15) Chou, N. H.; Ross, P. N.; Bell, A. T.; Tilley, T. D. *ChemSusChem* **2011**, 4, 1566.
(16) Brunschwig, B. S.; Chou, M. H.; Creutz, C.; Ghosh, P.; Sutin, N. *J. Am. Chem. Soc.* **1983**, 105, 4832.
(17) Jiao, F.; Frei, H. *Energy Environ. Sci.* **2010**, 3, 1018.
(18) Ahn, H. S.; Tilley, T. D. *Adv. Funct. Mater.* **2013**, 23, 227.
(19) Zidki, T.; Zhang, L.; Shafirovich, V.; Lymar, S. V. *J. Am. Chem. Soc.* **2012**, 134, 14275.
(20) Kay, A.; Cesar, I.; Grätzel, M. *J. Am. Chem. Soc.* **2006**, 128, 15714.
(21) Sathrum, A. J.; Kubiak, C. P. *J. Phys. Chem. Lett.* **2011**, 2, 2372.
(22) Zhao, D.; Huo, Q.; Feng, J.; Chmelka, B. F.; Stucky, G. D. *J. Am. Chem. Soc*. **1998**, 120, 6024.
(23) Burger, H.; Wannagat, U. *Monatsh. Chem.* **1963**, 94, 1007.
(24) Deschner, T.; Klimpel, M.; Tafipolsky, M.; Scherer, W.; Törnroos, K. W.; Anwander, R. *Dalton Trans.* **2012**, 41, 7319.
(25) Deschner, T.; Bjørn-Tore, L.; Widenmeyer, M.; Anwander, R. *J. Mater. Chem.* **2011**, 21, 5620.
(26) Deschner, T.; Törnroos, K. W.; Anwander, R. *Inorg. Chem.* **2011**, 50, 7217.
(27) Anwander, R.; Roesky, R. *J. Chem. Soc., Dalton Trans.* **1997**, 137.

(28) Deschner, T.; Liang, Y.; Anwander, R. *J. Phys. Chem. C* **2010**, 114, 22603.
(29) Cordeiro, P. J.; Tilley, T. D. *Langmuir* **2011**, 27, 6295.
(30) Yoon, C. W.; Hirsekorn, K. F.; Neidig, M. L.; Yang, X.; Tilley, T. D. *ACS Catal.* **2011**, 1, 1665.
(31) Fujdala, K. L.; Tilley, T. D. *J. Catal.* **2003**, 216, 265.
(32) Brutchey, R. L.; Ruddy, D. A.; Andersen, L. K.; Tilley, T. D. *Langmuir* **2005**, 21, 9576.
(33) Nakamoto, K. *Infrared and Raman Spectra of Inorganic and Coordination Compounds*, Wiley, Hoboken, 2009.
(34) Taylor, C. M.; Watson, S. P.; Bryngelson P. A.; Maroney, M. J. *Inorg. Chem.* **2003**, 42, 312.
(35) Goodgame, D. M. L.; Goodgame, M. *Inorg. Chem.* **1965**, 4, 139.
(36) Takada, S.; Fujii, M.; Kohiki, S. *Nano Lett.* **2001**, 1, 379.
(37) Taghavimoghaddam, J.; Knowles, G. P.; Chaffee, A. L. *Top Catal.* **2012**, 55, 571.
(38) Yang, J.; Liu, H.; Martens, W. N.; Frost, R. L. *J. Phys. Chem. C* **2010**, 114, 111.
(39) Lim, S.; Ciuparu, D.; Chen, Y.; Pfefferle, L.; Haller, G. L.; *J. Phys. Chem. B* **2004**, 108, 20095.
(40) Ciuparu, D.; Chen, Y.; Lim, S.; Haller, G. L.; Pfefferle, L.; *J. Phys. Chem. B* **2004**, 108, 503.
(41) Lim, S.; Ciuparu, D.; Pak, C.; Dobek, F.; Chen, Y.; Harding, D.; Pfefferle, L.; Haller, G. L. *J. Phys. Chem. B* **2003**, 107, 11048.
(42) Richmond, M. K.; Scott, S. L.; Alper, H. *J. Am. Chem. Soc.* **2001**, 123, 10521.
(43) Fleischman, S. D.; Scott, S. L. *J. Am. Chem. Soc.* **2011**, 133, 4847.
(44) Brinker, C. J., Scherer, G. W. *Sol-Gel Science*, Academic Press, Boston, 1990.
(45) Dai, X.; Kapoor, P.; Warren, T. H. *J. Am. Chem. Soc.* **2004**, 126, 4798.
(46) King, P.; Cléra, R.; Wernsdorfer, W.; Anson, C. E.; Powell, A. K. *Dalton Trans.* **2004**, 2670.
(47) Nakamura, R.; Frei, H. *J. Am. Chem. Soc.* **2006**, 128, 10668.
(48) Soo, H. S.; Macnaughtan, M. L.; Weare, W. W.; Yano, J.; Frei, H. *J. Phys. Chem. C* **2011**, 115, 24893.
(49) Weare, W. W.; Pushkar, Y.; Yachandra, V. K.; Frei, H. *J. Am. Chem. Soc.* **2008**, 130, 11355.
(50) Brunauer, S.; Emmett, P. H.; Teller, E.; *J. Am. Chem. Soc*. **1938**, 60, 309.
(51) Barrett, E. P.; Joyner, L. G.; Halenda, P. P. *J. Am. Chem. Soc*. **1951**, 73, 373.

Chapter 1. Appendix

Quantification of surface Si-OH sites on SBA-15

Quantification of surface Si-OH sites on SBA-15 was conducted following a published method from this laboratory.[A1] The reaction of $Mg(CH_2Ph)_2 \cdot 2THF$ with silica surface produces surface bound magnesium species and an equivalent of toluene, which then can be quantified by ^1H NMR spectroscopy. An average of 1.2 nm^{-2} Si-OH groups was measured in the SBA-15 samples used in this report.

Calculation of the theoretical maximum loading of cobalt on SBA-15

As described above, ca. 1.2 nm^{-2} Si-OH groups are surface accessible in the SBA-15 material used in this work. With the specific surface area of 634 $m^2 \cdot g^{-1}$, the total number of Si-OH sites is ca. 7.61 x 10^{20}. Because each surface grafted cobalt species is bipodal and consumes two Si-OH sites, the maximum possible number of cobalt atoms that can be surface bound is 3.80 x 10^{20}. Multiplying this number by the atomic mass of cobalt and dividing by the Avogadro's number yields 0.0372, that is the theoretical maximum weight fraction of cobalt per gram of SBA-15 material. Expressed in a mathematical form:

$$1.2 \ \frac{\text{SiOH}}{\text{nm}^2} \ \times \left[6.34 \ \times \ 10^{20} \ \frac{\text{nm}^2}{\text{g}}\right] \times \ \frac{\text{Surface Co}}{2 \ \text{SiOH}} \ = \ [3.80 \ \times \ 10^{20}] \ \text{Co/g}$$

$$[3.80 \ \times 10^{20} \ ] \frac{\text{Co}}{\text{g}} \ \times \ 58.933 \ \frac{\text{g}}{\text{mol Co}} \ \times \ \left[\frac{1}{6.022 \ \times 10^{23}}\right] \ \frac{\text{mol Co}}{\text{Co}}$$

$$= \ 0.0372 \ \ \text{mass fraction of Co per gram of material}$$

Turnover frequency (TOF) calculation

Turnover frequencies (TOF) for CoSBA catalysts were calculated by first converting the amount of oxygen formed into turnover numbers (TON) by dividing the amount of O_2 by the total number of cobalts in the catalysis reaction. This is the absolute lower limit for TOF, since all cobalt atoms in the reaction vessel are assumed to participate in the reaction. These TON values were then plotted against time, as shown in Figure A1, and the slope of the tangent line to the initial linear growth region of the plot (shown in blue lines in Figure A1) was taken to be the TOF of the catalyst. Typically 250 – 300 data points were selected in determining the slope. A sample calculation is as follows:

$$45\ \mu\text{mol}\ O_2 \times \left[0.040\ \text{g catalyst} \times 0.0048\ \text{wt\% Co} \times \frac{1 \times 10^6\ \mu\text{mol Co}}{58.933\ \text{g Co}}\right]^{-1} = 13.8\ \text{Turnovers}$$

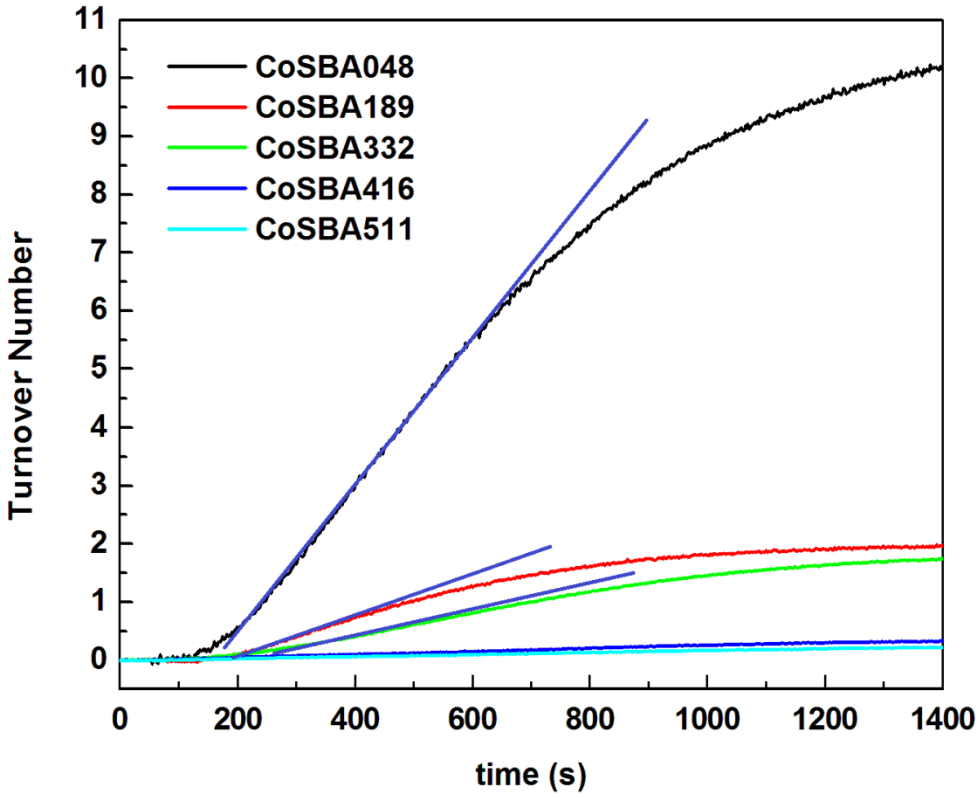

Figure A1. Catalytic turnover numbers as functions of time for selected CoSBA samples. Tangent lines to the initial onset of catalyses were depicted in blue, the slope of which represents the TOF_i of the catalyst ($TON \cdot time^{-1}$).

EXAFS Curve Fitting

X-ray absorption data treatment and EXAFS fitting were performed using Athena and Artemis programs in the Ifeffit software package. The goodness of the fits was evaluated by the EXAFS R-factors (R_f), which indicate the difference between data and theory. Evaluation of different fits to others was conducted by using the reduced χ_v^2 as described in literature.[A2-A4]

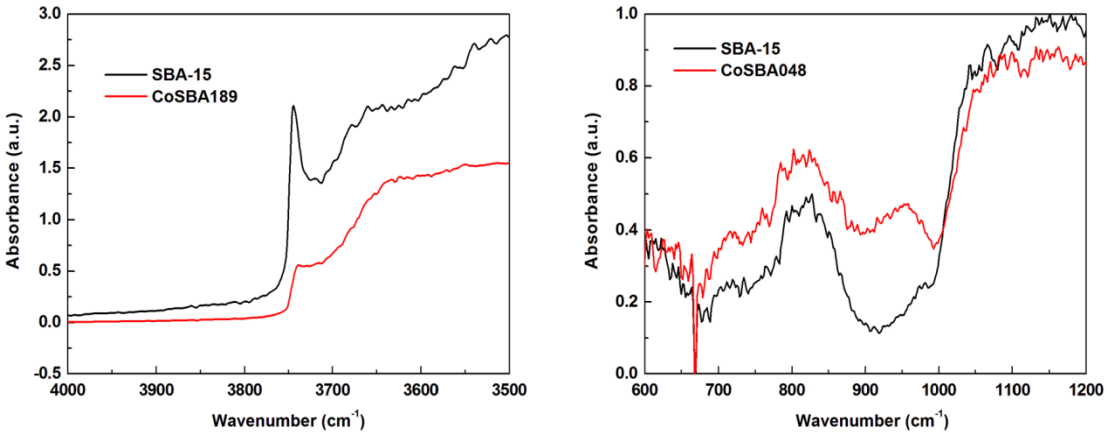

Figure A2. Selected regions in the diffuse reflectance FTIR spectra of CoSBA materials are displayed referenced to the parent SBA-15. Diminishing of SiO-H vibration at ca. 3750 cm^{-1} with concomitant appearance of Co-O-Si vibration at ca. 940 cm^{-1}suggests that the cobalt centers on CoSBA materials are covalently binding to the surface via the consumption of surface Si-OH groups.

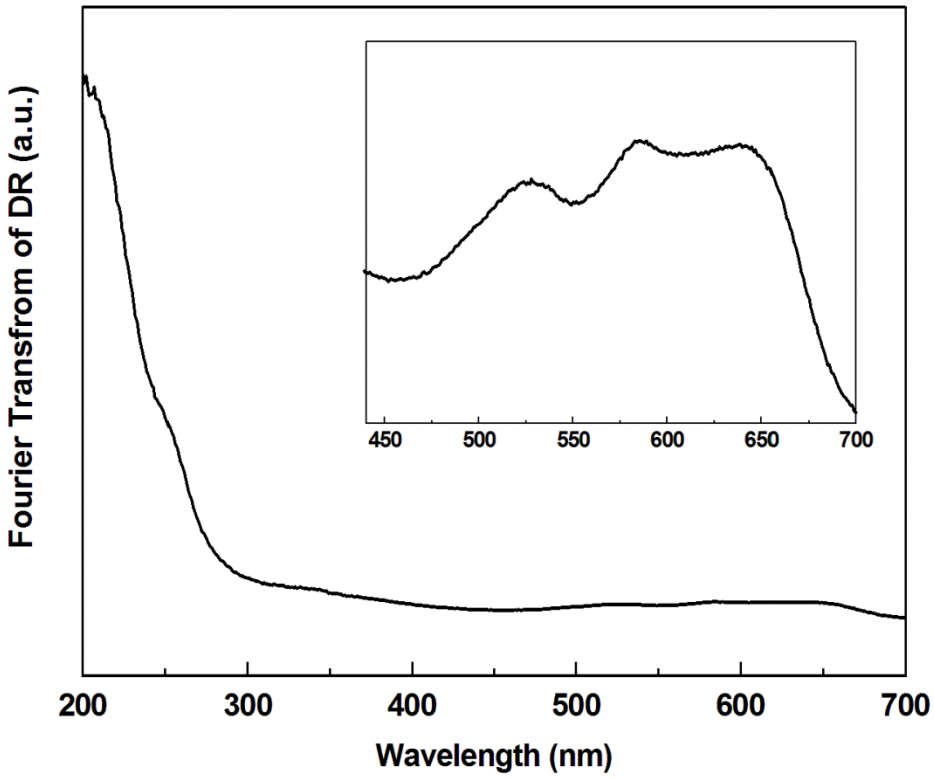

Figure A3. Diffuse reflectance UV-vis spectrum of CoSBA189 is displayed. The three peaks in the d-d transition region at 530, 580, and 650 nm are indicative of T_d Co^{II} centers.

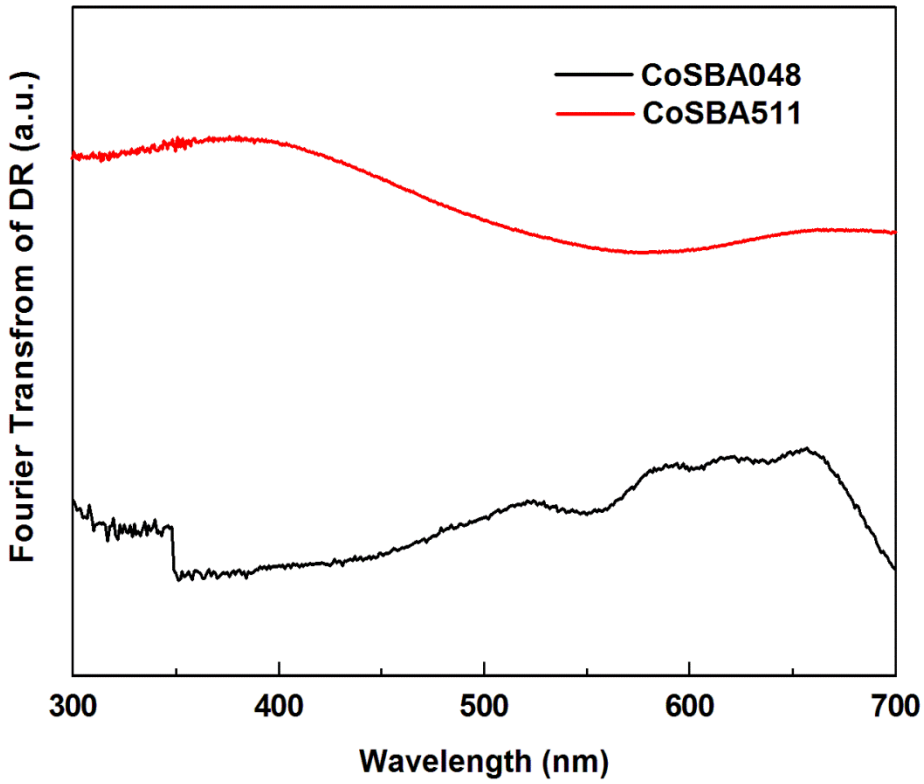

Figure A4. Diffuse reflectance UV-vis spectrum of CoSBA511 is displayed along with that of CoSBA048. The broad band centered around 350 nm is characteristic of Co_3O_4.

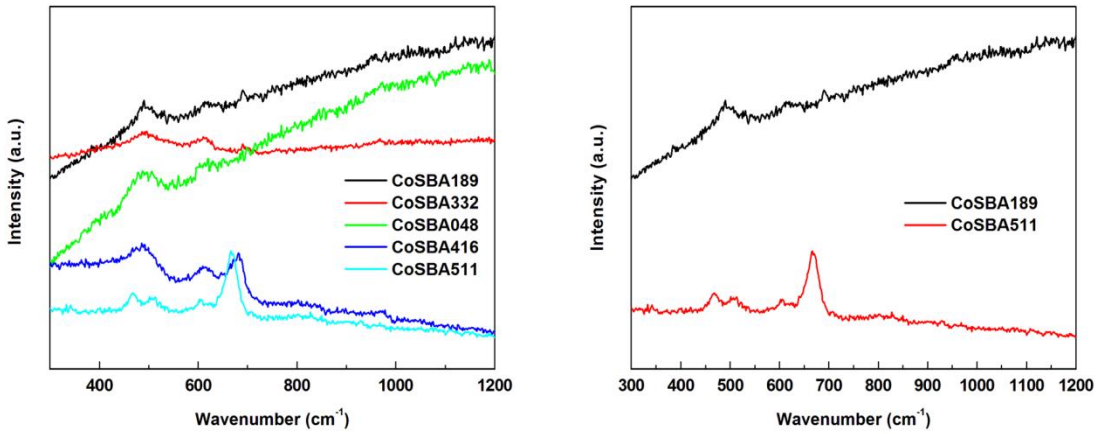

Figure A5. Raman spectra of CoSBA materials. Broad vibration centered at 500 cm^{-1} was observed for CoSBA samples of lower loading, where as peaks at 485, 505, and 691 cm^{-1} (indicative of Co_3O_4) were observed for CoSBA416 and CoSBA511.

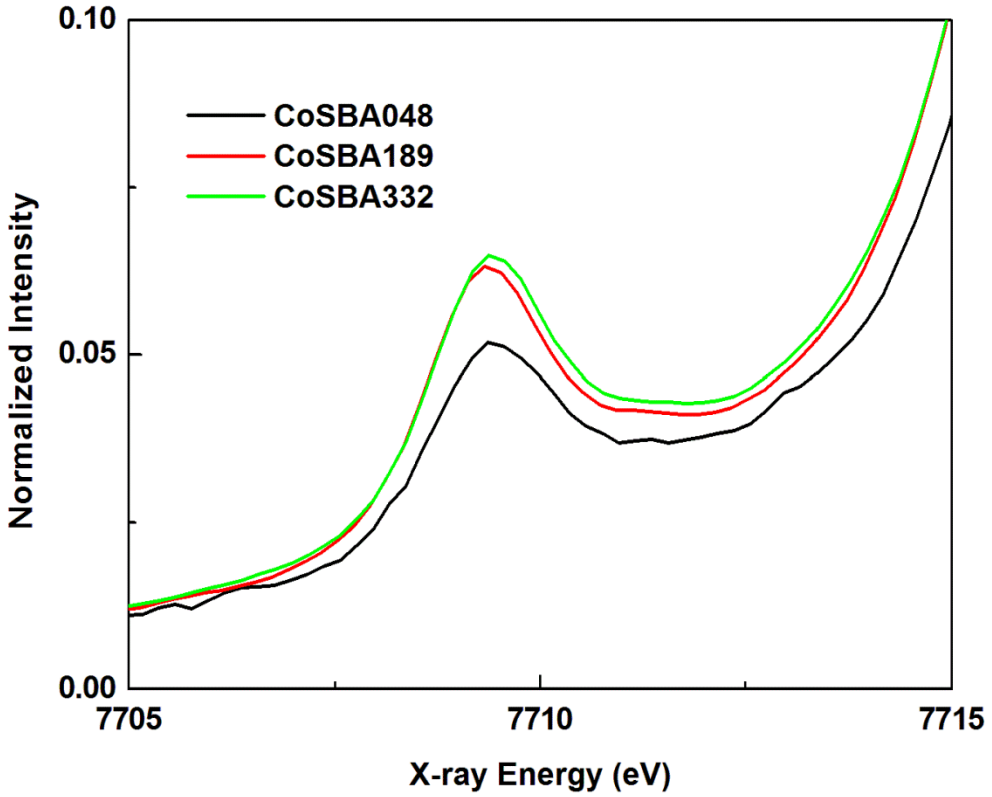

Figure A6. Pre-edge feature at 7709 eV was observed in the XANES spectra of low loading CoSBA samples, indicating the Co^{II} centers are in noncentrosymmetric (T_d) coordination environments. (CoSBA048, 189, and 332 shown, since these samples collected at the ALS showed more clearly the pre-edge peaks than those of CoSBA027 and CoSBA106 collected at SSRL).

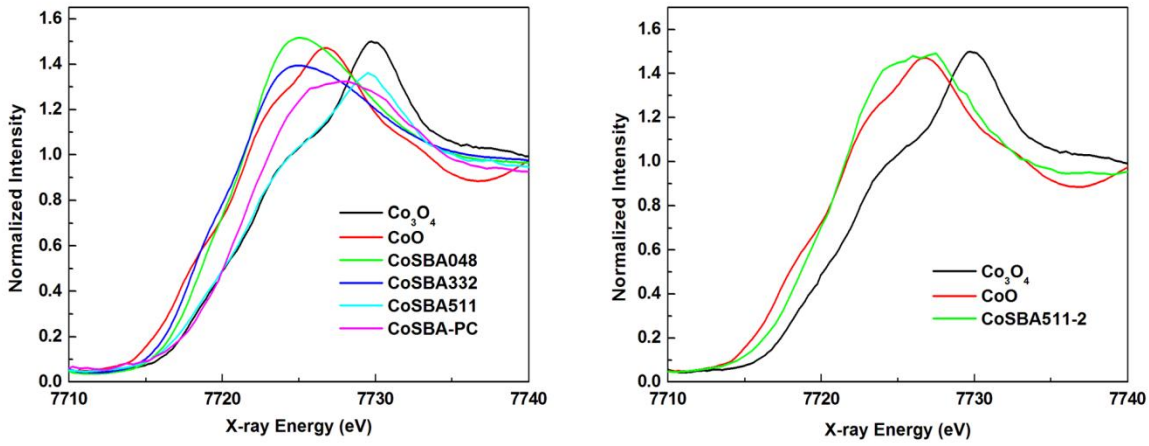

Figure A7. XANES spectra of CoSBA materials are displayed on the left. XANES of CoSBA511 closely resembles that of Co_3O_4, suggesting that small domains of Co_3O_4 were formed. On the right, however, XANES of a different part of CoSBA511 resembles those of lower loading CoSBA samples, exhibiting inhomogeneity in the material unlike any other CoSBA materials.

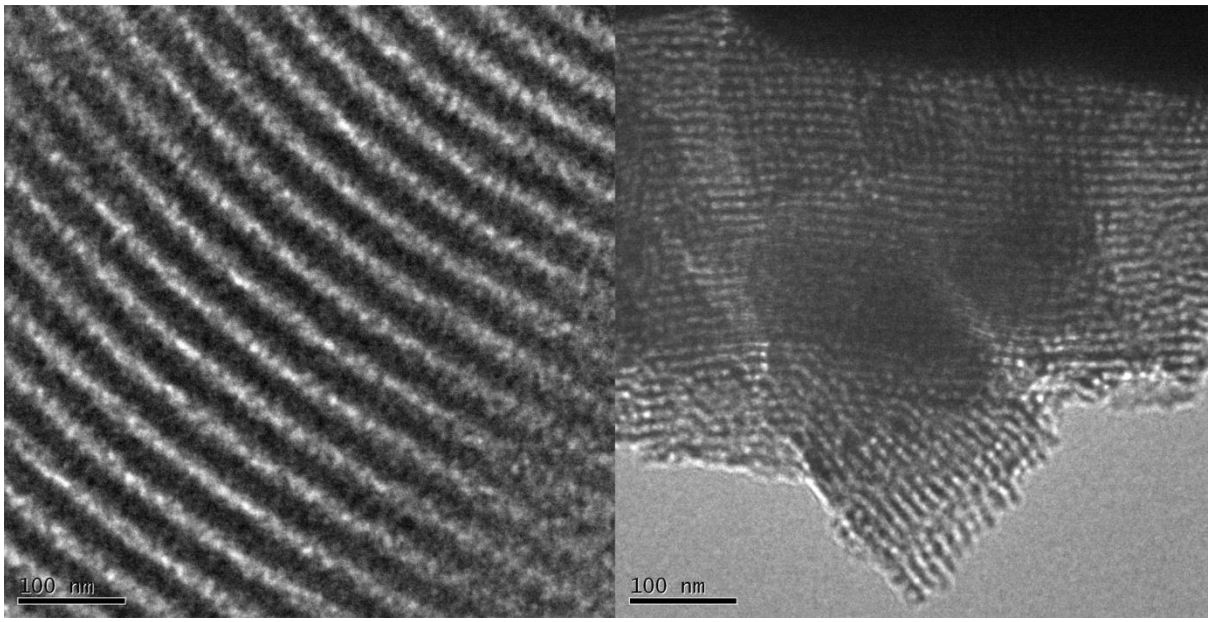

Figure A8. TEM images of CoSBA416 and CoSBA511 samples. Even at the highest of loadings no blockage of pores or visible particle formation was observed.

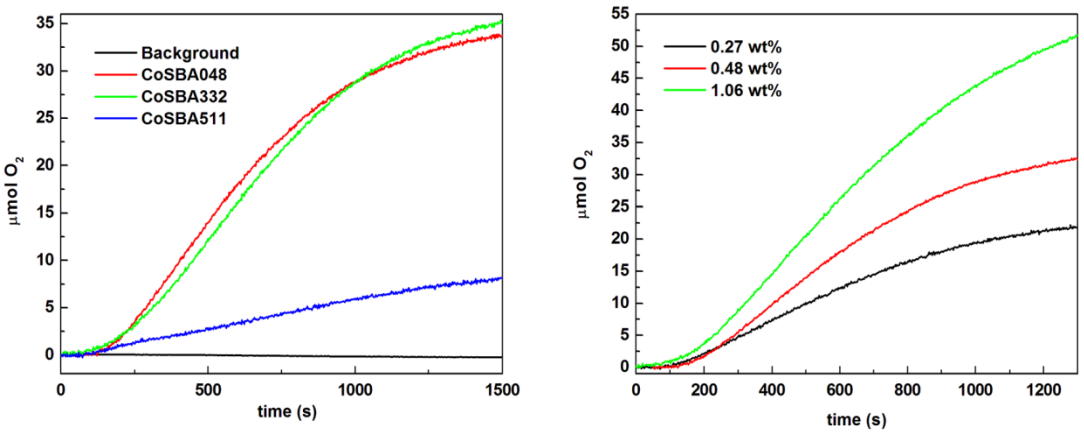

Figure A9. Oxygen evolution with time is plotted above. As seen on the right, overall product formation grows linearly with increasing surface concentration of cobalt. On the left, it is seen that the background (SBA-15) slowly drops below zero over time due to the evolution of CO_2 from bicarbonate buffer and the decomposition of $Ru(bpy)_3^{2+}$, assuring that the reaction vessel was gas-tight and the oxygen penetration from the atmosphere was negligible.

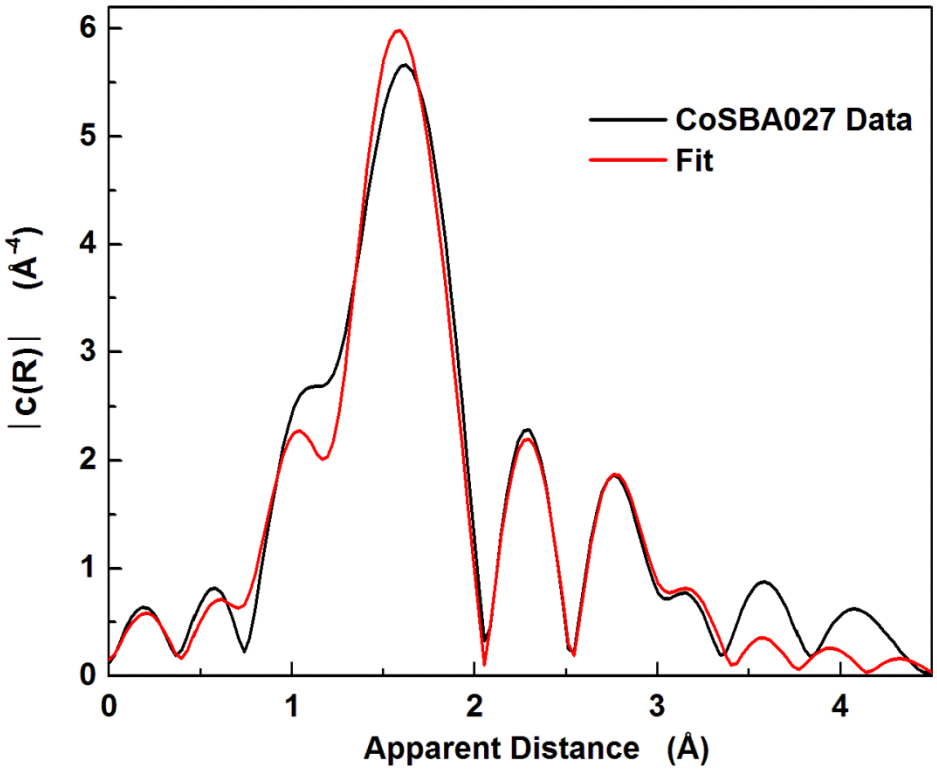

Figure A10. EXAFS fit of CoSBA027 is displayed (also shown in Figure 3). The EXAFS R-factor (R_f) for the fit is 0.0016 and the reduced χ_v^2 is 32.9. Co-O distance in this model is 2.07 Å with a coordination number (CN) of 5. Co-Si distance in this model is 3.26 Å with a CN of 2. Co-Co distance in this model is 2.82 Å with a CN of 0.4.

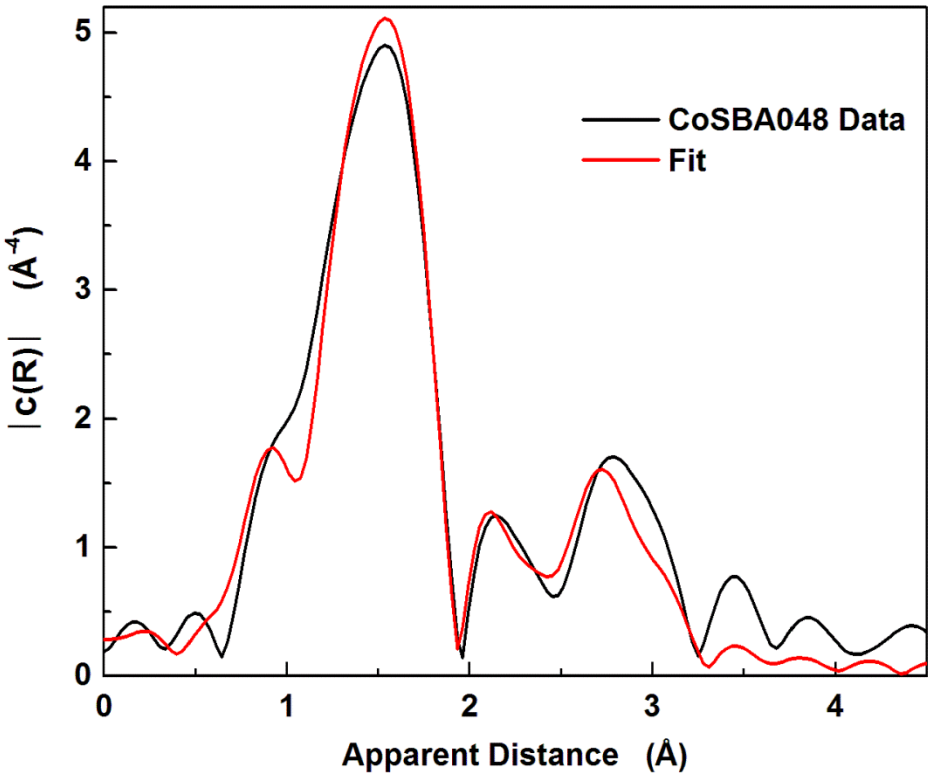

Figure A11. EXAFS fit of CoSBA048 is displayed. The EXAFS R-factor (R_f) for the fit is 0.0053 and the reduced χ_v^2 is 42.8. Co-O distance in this model is 2.04 Å with a coordination number (CN) of 5. Co-Si distance in this model is 3.27 Å with a CN of 2. Co-Co distance in this model is 2.93 Å with a CN of 0.5.

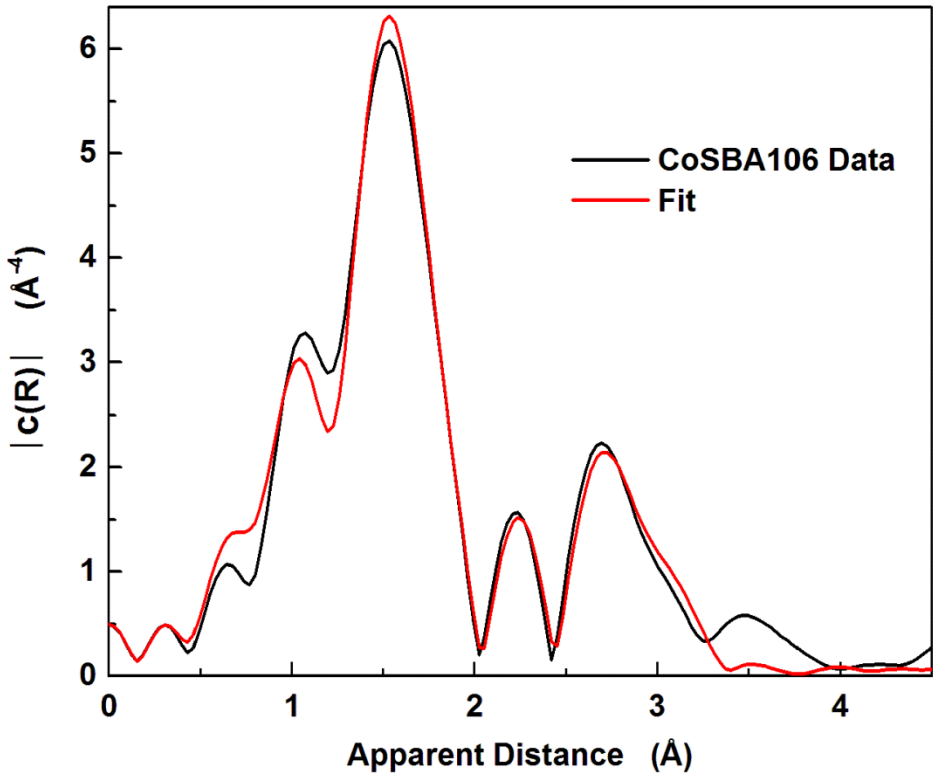

Figure A12. EXAFS fit of CoSBA106 is displayed. The EXAFS R-factor (R_f) for the fit is 0.0043 and the reduced χ_v^2 is 9.3. Co-O distance in this model is 2.09 Å with a coordination number (CN) of 5. Co-Si distance in this model is 3.29 Å with a CN of 2. Co-Co distance in this model is 2.89 Å with a CN of 1.2.

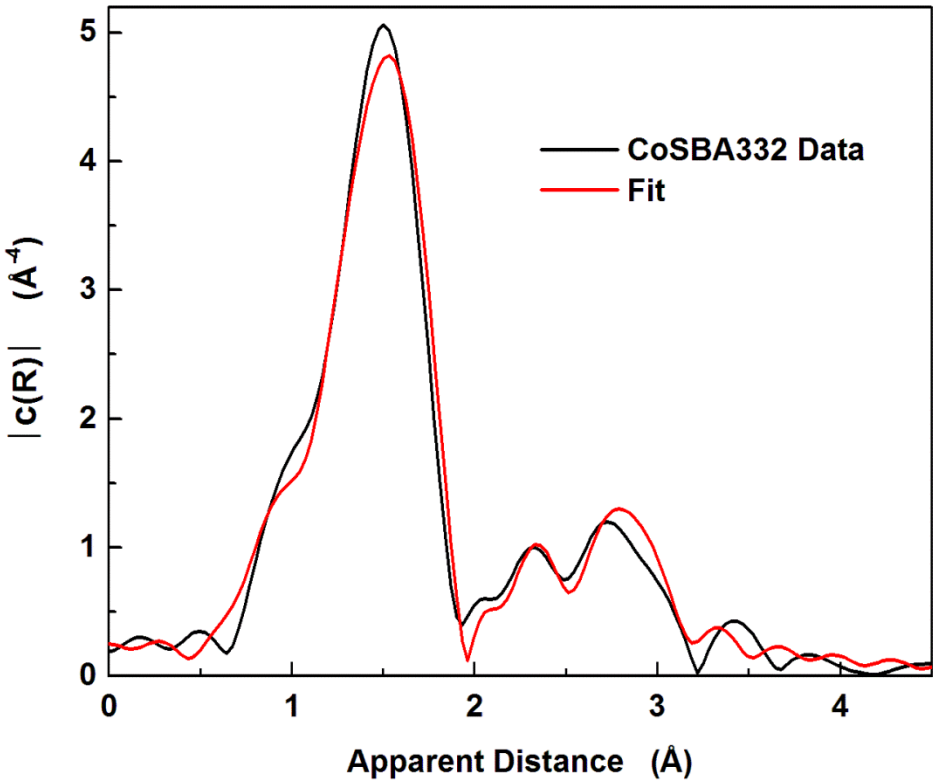

Figure A13. EXAFS fit of CoSBA332 is displayed. The EXAFS R-factor (R_f) for the fit is 0.0068 and the reduced χ_v^2 is 65.7. Co-O distance in this model is 2.02 Å with a coordination number (CN) of 5. Co-Si distance in this model is 3.12 Å with a CN of 2. Co-Co distance in this model is 3.04 Å with a CN of 2.3.

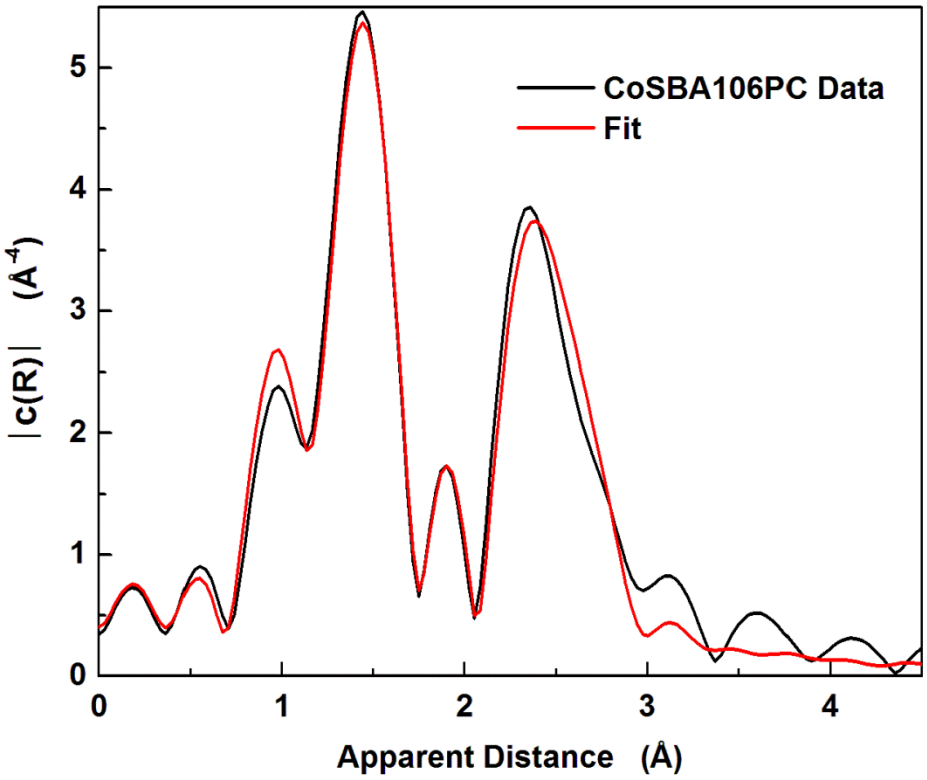

Figure A14. EXAFS fit of CoSBA106 after catalysis is displayed. The EXAFS R-factor (R_f) for the fit is 0.0070 and the reduced χ_v^2 is 28.0. Co-O distance in this model is 1.96 Å with a coordination number (CN) of 5.6. Co-Si distance in this model is 2.77 Å with a CN of 2. Co-Co distance in this model is 2.66 Å with a CN of 1.6.

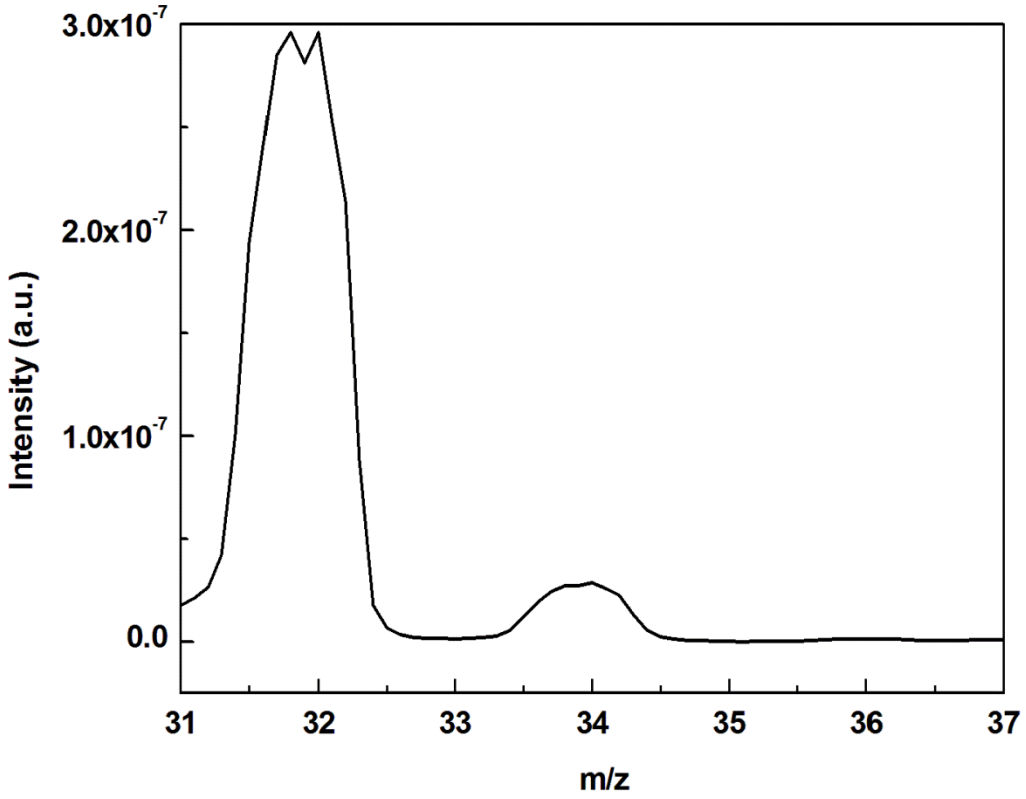

Figure A15. Mass spectrograph of evolved oxygen in an experiment with $H_2{}^{18}O$ (5.5 vol %) employing CoSBA048 as the catalyst. The observed ratio of $^{32}O_2$ and $^{34}O_2$ from the MS data is 8.77, well corresponding to a predicted value from a 5.5 vol % $H_2{}^{18}O$ solution of 8.59. The agreement between the calculated and the observed ratios of $^{32}O_2$ and $^{34}O_2$ indicates that the sole source of O_2 was water.

Table A1. Isotopic product distribution and calculated yields of an ^{18}O labeling experiment.

	$H_2{}^{18}O/H_2{}^{16}O$ v/v %	$^{16}O_2$	$^{16}O^{18}O$	$^{18}O_2$
Measured	5.5 ± 0.9	89.8 ± 7.9	10.2 ± 2.1	trace*
Calculated		89.3	10.4	0.3

*****Note: $^{18}O_2$ detected had poor S/N such that the integration of the peak was not reliable.

Table A2. EXAFS curve fitting results of CoSBA samples.

Fit	**Path**	**R (Å)**	**N**	**σ^2 (Å^{-2})**	**ΔE_0 (eV)**	**Reduced χ_v^2**	**R_f (%)**
CoSBA027	Co-O	2.07 (0.014)	5.0	0.009 (0.002)	5.2 (1.1)	32.9	1.6
	Co-Si	3.26 (0.033)	2.0	0.005 (0.004)			
	Co-Co	2.82 (0.030)	0.4	0.007 (0.003)			
CoSBA048	Co-O	2.04 (0.011)	5.0	0.010 (0.001)	2.0 (1.0)	42.8	5.3
	Co-Si	3.27 (0.024)	2.0	0.007 (0.003)			
	Co-Co	2.93 (0.044)	0.5	0.006 (0.004)			
CoSBA106	Co-O	2.09 (0.009)	5.0	0.010 (0.001)	0.3 (0.7)	9.3	4.3
	Co-Si	3.29 (0.017)	2.0	0.016 (0.007)			
	Co-Co	2.89 (0.007)	1.2	0.003 (0.001)			
CoSBA332	Co-O	2.02 (0.012)	5.0	0.010 (0.002)	3.6 (1.1)	65.7	6.8
	Co-Si	3.12 (0.036)	2.0	0.016 (0.004)			
	Co-Co	3.04 (0.031)	2.3	0.004 (0.003)			
CoSBA106PC	Co-O	1.96 (0.020)	5.6	0.011 (0.003)	3.2 (2.0)	28.0	7.0
	Co-Si	2.77 (0.056)	2.0	0.004 (0.002)			
	Co-Co	2.66 (0.016)	1.6	0.015 (0.010)			

Fitting region : $1 \leq R\ (Å) \leq 5.5$, $2.5 \leq k\ (Å^{-1}) \leq 11.5$

References

(A1) Fujdala, K. L.; Tilley, T. D. *J. Am. Chem. Soc.* **2001**, 123, 10133.
(A2) Newville, M.; Boyanov, B. I.; Sayers, D. E. *J. Synchrotron Rad*. **1999**, 6, 264.
(A3) Newville, M. *J. Synchrotron Rad*. **2001**, 8, 322.
(A4) Ravel, B.; Newville, M. *J. Synchrotron Rad*. **2005**, 12, 537.

Chapter 2. Water Oxidation by Single-Site Cobalt Centers on Various Oxide Surfaces: The Effects of Oxide Surface Acidity and Oxygen Atom Affinity on Catalysis

Introduction

Achieving artificial photosynthesis in a robust and economically-viable device is one of science's prime technical challenges.[1] One significant hurdle is the development of efficient water oxidation catalysts, especially those employing only first-row, earth-abundant transition metals.[2-4] As a result, the mechanisms of existing water oxidation catalysts are studied in great detail to identify bottlenecks[5,6] and elucidate structural requirements.[7] However, many of the proposed mechanisms remain speculative. We recently reported the development and evaluation of small-domain cobalt catalysts on SBA-15 silica and found that a single-site cobalt is not only active for water oxidation catalysis but exhibits higher turnover frequency (TOF) than a surface cobalt atom on Co_3O_4.[7] A similar single-site cobalt on an FTO surface was also found by Meyer and co-workers to catalyze water oxidation.[8] In addition, Mattioli and Guidoni recently reported theoretical work that suggests the lowest-energy pathway for oxygen evolution on a multi-atom cobalt oxide cluster involves geminal coupling of a cobalt-oxo with a hydroxyl or an aquo ligand.[9] A similar pathway may be viable on a single-site cobalt on a heteroatom oxide support. Herein we report the syntheses of single-site cobalt atoms on various oxide surfaces (MgO, TiO_2, AlPO, SBA-15, and Y-Zeolite) and evaluation of their ability to catalyze water oxidation. Single-site cobalts supported on basic supporting oxides (TiO_2 and MgO) exhibited superior catalysis relative to those on acidic oxides (Y-Zeolite, AlPo, and SiO_2). However, no dependence of catalytic performance on the oxygen atom affinities of the supporting oxides was observed.

Results and Discussion

Single-site cobalt catalysts on various supporting oxides were prepared using a previously published method with minor modifications.[7] The bis(amido) complex $Co[N(SiMe_3)_2]_2$[10] was employed as a precursor to introduce cobalt centers on the oxide surfaces by mixing a hexanes solution of the complex with a hexanes suspension of the appropriate oxide (Scheme 1). The resulting material was thoroughly washed with hexanes and then calcined at 300 °C in air to remove residual organic material. The all-inorganic nature of the catalyst samples was verified by carbon, hydrogen, and nitrogen elemental analyses (CHN found for all samples: C < 0.14, H < 0.90, N < 0.10).

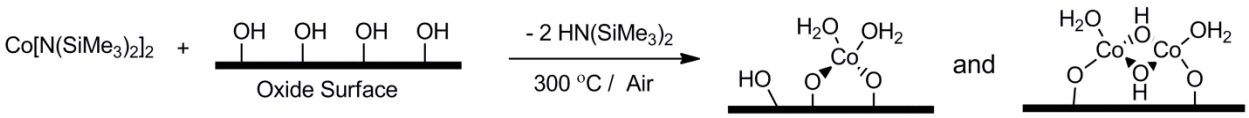

Scheme 1. Synthesis of single-site cobalts on oxide surfaces

The supporting oxide materials employed in this work (TiO_2, MgO, SBA-15, AlPO, and Y-Zeolite) were chosen to span a wide range of surface acidities and oxygen atom affinities. Surface acidities of the oxides were estimated by the solids' reported proton affinities,[11] and

oxygen atom affinities were estimated by the E–O bond dissociation energies (E = Si, Al, P, Ti, and Mg; average of the two constituents was assumed for AlPO and Y-Zeolite).[12] Low precursor loadings were chosen for all samples to ensure the single-site nature of the cobalt catalytic centers.[7] Cobalt content in all samples were verified by inductively coupled plasma optical emission spectroscopy (ICP-OES). The synthesized samples of cobalt on MgO (CoMgO, 0.24 wt% Co), TiO_2 ($CoTiO_2$, 0.26 wt% Co), AlPO (CoAlPO, 0.22 wt% Co), SBA-15 (CoSBA, 0.27 wt% Co),[13] and Y-Zeolite (CoYZ, 0.31 wt% Co) contained predominantly single sites on the surface as evidenced by the extended X-ray absorption fine structure (EXAFS) spectra (Figures A1-A4). All of the samples' EXAFS spectra contain no significant peaks at apparent distances greater than 2.5 Å which indicates that second coordination shell interactions with neighboring cobalt atoms are negligible and suggests that most of the catalytic centers are single sites.

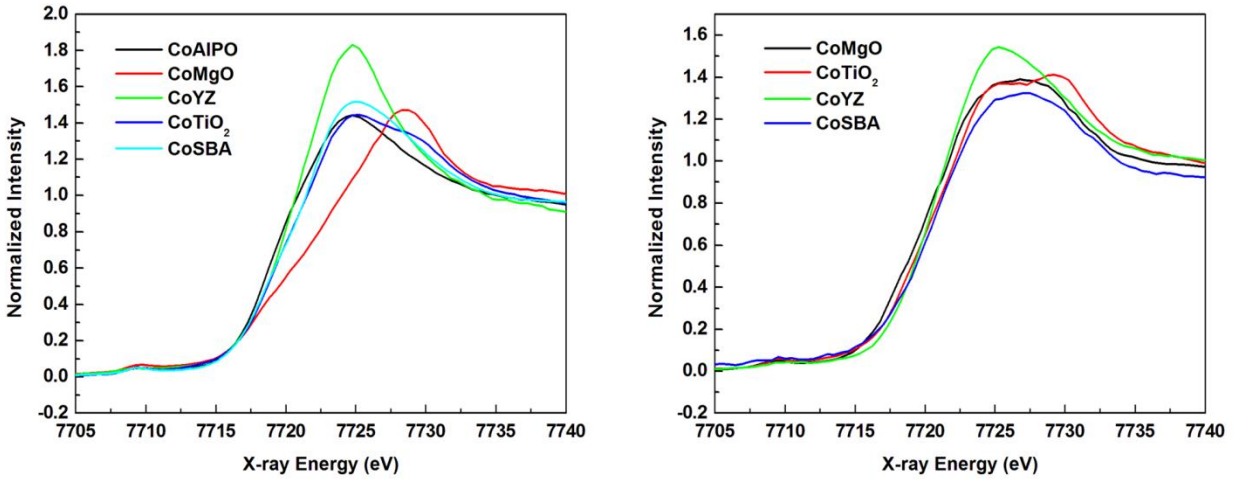

Figure 1. XANES spectra surface-bound cobalt catalysts (left). Notably, CoMgO exhibits a high edge energy compared to the other samples, indicating a higher average oxidation state. XANES spectra of the samples after catalysis are shown on the right. All of the samples reveal similar oxidation state (a mixture of 2+ and 3+) in their resting states. Post-catalysis XANES spectrum for CoAlPo was not collected due to the material's instability during catalysis.

As in CoSBA materials,[7] the cobalt atoms in CoMgO, $CoTiO_2$, CoAlPO, and CoYZ are covalently bound to the surface via Co–O–E type linkages. The samples' IR spectra after grafting display a diminished intensity of the EO–H vibration[14] at ca. 3580 cm^{-1} and new Co–O–E vibrations (1090 cm^{-1} for MgO, 1098 cm^{-1} for AlPO, 980 cm^{-1} for TiO_2, and 960 cm^{-1} for YZ).[15] UV-Vis spectroscopy and X-ray absorption near edge structure (XANES) spectroscopy were employed to probe the oxidation states of the surface cobalt centers. The d-d transitions characteristic the pseudotetrahedral Co^{2+} centers[16,17] are found in the UV-vis spectra of CoYZ, $CoTiO_2$, CoSBA,[13] and CoAlPO samples (ca. 550, 600, and 640 nm; Figures A5-A7). XANES spectra of these materials further confirm the +2 oxidation states of cobalt atoms with cobalt edge energies found at ca. 7719.5 eV (Figure 1).[18] On the other hand, the UV-Vis spectrum of CoMgO exhibits a peak at 430 nm (Figure A8), characteristic of Co^{3+} centers on an oxide.[19] In

addition, the XANES spectrum of CoMgO (Figure 1) displays an edge energy of ca. 7722 eV, which suggests that the overall oxidation state of the cobalt centers is between 2+ and 3+. (Compare to edge energy for $Co^{II}Co^{III}_2O_4$ at ca. 7723 eV; Figure A9.) All samples in this study contain a pre-edge feature in their XANES spectra at ca. 7709 eV (a 1s to 3d transition) that indicates the presence of non-centrosymmetric Co^{2+} centers, which is consistent the aforementioned spectroscopic observations.

Photochemical water oxidation experiments were conducted employing CoMgO, $CoTiO_2$, CoAlPO, CoYZ, and CoSBA as catalysts. A buffered aqueous solution at pH 5.5-5.6 ($NaHCO_3/Na_2SiF_6$) was used with $Na_2S_2O_8$ as a sacrificial electron acceptor.[4] A 488 nm laser with a power output of 260 mW and a focused beam diameter of 0.5 cm was used as the light source. The headspace oxygen concentration was monitored in real-time using a fluorescence-based oxygen probe. The same amount of catalyst (40 mg) was used for each experiment. CoMgO, CoYZ, $CoTiO_2$, and CoSBA produced oxygen at good catalytic rates (Figure 2). All of these catalysts can be recycled and achieve turnover numbers greater than 50 with additional portions of $Na_2S_2O_8$. No cobalt leaching was observed by ICP-OES after 25 turnovers. The CoAlPO material deactivated after about 3 turnovers as it decomposed and dissolved into solution. The generation of locally-concentrated low pH sites during catalysis is likely responsible for the AlPO degradation.

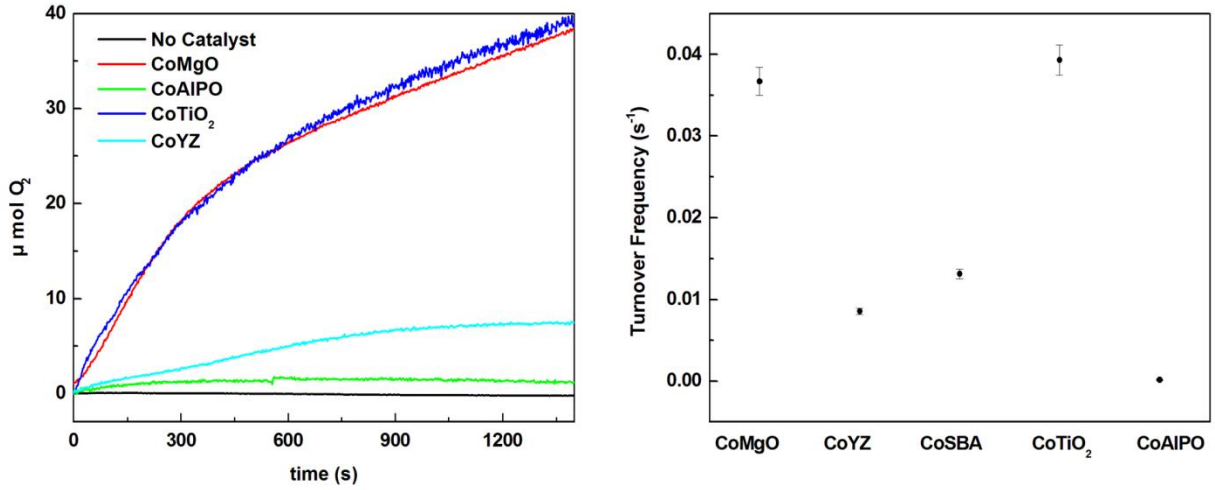

Figure 2. Oxygen evolution of surface-bound single-site cobalt catalysts over time (left) and the initial turnover frequencies of the catalysts (right).

The catalysts' initial turnover frequencies (TOF_i s) are also plotted in Figure 2.[13] Notably, the TOF_i s of CoMgO and $CoTiO_2$ are three times greater than that of CoSBA and ca. 100 fold greater than that of a surface atom of a Co_3O_4 nanoparticle.[7] Surface acidities of the supporting oxides appear to correlate with the TOF_i (Figure 3), as catalysis on more basic oxides (MgO and TiO_2) exhibited catalytic rates significantly greater than those on acidic oxides (SBA-15 and Y-Zeolite). The evolution of protons during water oxidation and the subsequent drop in the local

pH around the catalytic center is presumably alleviated by the basic sites in MgO and TiO_2, resulting in their superior catalytic performance.

Recent work by Mattioli and Guidoni suggests that the rate determining step for oxygen evolution by a cobalt cluster involves the formation of a high-valent oxo, which then couples to a hydroxo or an aqua ligand on the same cobalt to generate the O–O bond.[9] From this proposed mechanism, we hypothesized that for a single-site cobalt catalyst bound to an oxide surface, the oxide's oxygen atom affinity may affect the rate of catalysis because it would facilitate O–O bond formation and O_2 release. The oxygen atom affinities of the oxides employed in this work have been estimated by the E–O bond dissociation energies (E = Si, Al, P, Ti, and Mg; average of the two constituents was assumed for AlPO and Y-Zeolite).[12] However, a plot of the catalysis rates as a function of surface oxide oxygen atom affinities (Figure 3) displays no apparent relationship between TOF_i and oxygen atom affinity.

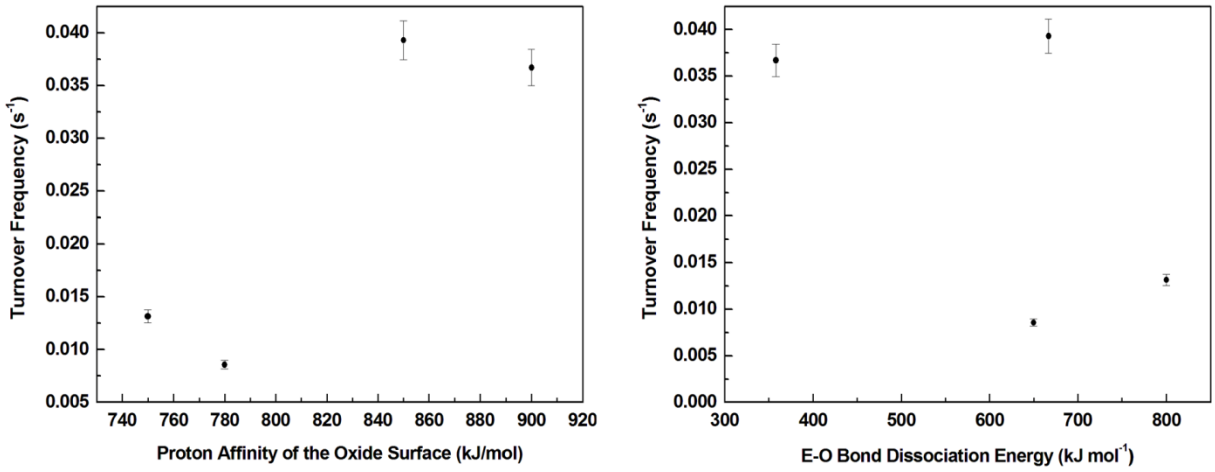

Figure 3. TOF_i s of the catalysts were plotted as functions of the properties of supporting oxides: surface acidity (left) and oxygen atom affinity (right). The data for CoAlPO was not included due to its instability during catalysis.

The cobalt centers' oxidation states were analyzed after catalysis by XANES spectroscopy (Figure 1). All of the catalytically active samples (CoSBA, $CoTiO_2$, CoMgO, and CoYZ) revealed a similar edge energy of ca. 7721 eV, lower than that of Co_3O_4 (7723.2 eV, Figure A9), suggesting that the ratio of Co^{2+} to Co^{3+} is lower than 1:2. The overall mixed Co^{2+}-Co^{3+}oxidation state in these catalysts' resting states corroborates many proposed mechanisms that suggest oxidation of Co^{2+} to Co^{3+} precedes the rate determining step, which is believed to be further oxidation of a Co^{3+} species.[9,20] Notably, compared to the oxidation state before catalysis, the cobalt centers in CoMgO are overall reduced after catalysis, confirming that Co^{2+} is involved in the catalytic cycle.

Conclusions

A molecular method for introducing cobalt single-sites on a supporting oxide has been expanded beyond silica to a variety of other surfaces. Water oxidation catalysis by single-site cobalt centers on various oxides was observed and quantified. Cobalt centers supported on basic oxides (MgO and TiO_2) exhibited superior catalytic performance compared to those on acidic oxides (Y-Zeolite and SiO_2). A cobalt center on MgO exhibited a TOF_i of 0.04 s^{-1}, which is three times greater than that of a cobalt atom on SBA-15 and 100 times greater than that of a Co_3O_4 surface atom.[7] No apparent correlation between the catalytic TOF_i and the oxygen atom affinities of the surface oxides was observed. XANES spectroscopy of the resting oxidation states of the catalysts revealed mixed oxidation states of Co^{2+} and Co^{3+} that indicatethe rate determining step requires a further oxidation of Co^{3+}, as is suggested in many proposed mechanisms.[9,20]

Experimental

General. All manipulations were conducted under an inert nitrogen atmosphere using standard Schlenk techniques or in a Vacuum Atmospheres drybox, unless otherwise stated. Chemicals were purchased from Aldrich and used as received. Dry, oxygen-free solvents were used throughout. The complex $Co[N(SiMe_3)_2]_2$[10], mesoporous SBA-15[21], and mesoporous AlPO[22] were synthesized as reported in the literature. Porous TiO_2, MgO, (Aldrich) and Y-Zeolite (Zeolyst) were purchased and used without further purification. Carbon, hydrogen, and nitrogen elemental analyses were performed at the College of Chemistry's Microanalytical Laboratory at the University of California, Berkeley. DR-FTIR spectra were obtained using a Thermo Nicolet 6700 FTIR spectrometer. The DRUV-Vis spectra were acquired using a Perkin-Elmer Lambda 9 spectrometer equipped with a 60 mm integrating sphere, a slit width of 4 nm, and at a collection speed of 120 nm/min. All samples were run using MgO as a reference background. Powder x-ray diffraction (PXRD) patterns were recorded on a Bruker D-8 GADDS X-ray diffractometer using Co K_α radiation (λ = 1.7902 Å). The pH measurements were conducted using a Thermo Orion 2 Star pH meter. Inductively coupled plasma optical emission spectroscopy (ICP-OES) for cobalt ion detection in post catalytic solutions was performed on a Perkin-Elmer ICP-OES Optima 7000 DV (detection limit for Co ions: 0.25 ppb). Standard solutions were purchased from Perkin-Elmer and used as received. Heat treatments were conducted in a Lindberg 1200 ℃ three-zone furnace.

Syntheses of surface-supported cobalt catalysts. Catalyst synthesis was performed following a previously published procedure with minor modifications.[7] In a typical synthesis, $Co[N(SiMe_3)_2]_2$ (16 mg, 42 μmol) in 25 mL of hexanes was added to a hexanes suspension of the material support (1 g in 25 mL; AlPO, SBA-15, TiO_2, MgO, and Y-Zeolite). The green solution of $Co[N(SiMe_3)_2]_2$ instantaneously changed color as it came in contact with the hexanes-suspended material. Reactions with SBA-15 and AlPO resulted in light blue colored mixtures; MgO and TiO_2 gave grey-green mixtures, and the Y-Zeolite gave a pale brown mixture. The reaction mixtures were stirred under nitrogen for 0.5 h. The solid was collected, washed thoroughly with hexanes, and air dried. The dried materials were then calcined under flowing air (110 cc/min) to 300 ℃ for 6 h to remove residual organics.

X-ray Absorption Spectroscopy (XAS) data collection. The combination of XANES and EXAFS spectra were collected at BL 10.3.2 in the Advanced Light Source (ALS) at LBNL, and at BL 7-3 at the Stanford Synchrotron Radiation Lightsource (SSRL). At the ALS, the synchrotron ring operated at 1.9 GeV at a 500 mA beam current. Energy resolution of the focused incoming X-rays at BL 10.3.2 was achieved using a Si(111) double-crystal monochromator. Fluorescence spectra were collected with a 7-element Ge detector, and transmission spectra were obtained with a I_1 ion chamber filled with N_2 gas. An incident X-ray beam of 0.1 mm (H) x 0.02 mm (V) dimensions was used for the XANES and EXAFS

experiments. At SSRL, the electron energy was set at 3.0 GeV with an average current of 450 mA. A Si(220) double-crystal monochromater was used. Spectra were collected in fluorescence mode in a chamber filled with N_2 gas. Energy calibrations are based on the rising edge energy of Co foil at 7709.0 eV (ALS) and at 7709.5 eV (SSRL). Each spectrum is the average of 6 to 9 scans. All measurements were done at room temperature.

Water oxidation catalysis experiments and oxygen detection. Light-driven water-oxidation reactions were performed in a buffered aqueous solution at pH 5.5-5.6 ($NaHCO_3$/Na_2SiF_6) employing $Na_2S_2O_8$ as a sacrificial electron acceptor. The sensitizer used for the experiments was $[Ru(bpy)_3]Cl_2$. To remove oxygen, water was sparged with nitrogen for 1 h prior to experiments. A gas-tight glass cell with an internal volume of 37.6 mL was used as the reaction vessel. In a typical experiment, 40 mg of catalyst was suspended in 15 mL of buffered water along with 18 mg of $[Ru(bpy)_3]Cl_2$, 100 mg of Na_2SO_4, and 36 mg of $Na_2S_2O_8$. A 488 nm laser with a power output of 260 mW, focused at a beam diameter of 0.5 cm, was used as the light source. The head-space oxygen concentration was monitored in real time by a multi-frequency fluorescence oxygen probe (Ocean Optics FOSPOR-R). Before each experiment, the oxygen probe was calibrated using a five-point calibration method at the following oxygen concentrations (vol. %) in helium: 0, 1.68, 3.62, 6.38, and 20.

References

(1) Gray, H. B. *Nat. Chem.* **2009**, 1, 7.
(2) Dau, H.; Christian, L.; Reier, T.; Risch, M.; Roggan, S.; Strasser, P. *ChemCatChem* **2010**, 2, 724.
(3) Romain, S.; Vigara, L.; Llobet, A. *Acc. Chem. Res.* **2009**, 42, 1944.
(4) Youngblood, W. J.; Lee, S.-H. A.; Maeda, K.; Mallouk, T. E. *Acc. Chem. Res.* **2009**, 42, 1966.
(5) Surendranath, Y.; Kanan, M. W.; Nocera, D. G. *J. Am. Chem. Soc.* **2010**, 132, 16501.
(6) Zhong, D. K.; Gamelin, D. R. *J. Am. Chem. Soc.* **2010**, 132, 4202.
(7) Ahn, H. S.; Yano, J.; Tilley, T. D. *Energy Environ. Sci.* **2013**, 6, 3080.
(8) Kent, C. A.; Concepcion, J. J.; Dares, C. J.; Torelli, D. A.; Rieth, A. J.; Miller, A. S.; Hoertz, P. G.; Meyer, T. J. *J. Am. Chem. Soc.* **2013**, 135, 8432.
(9) Mattioli, G.; Giannozzi, P.; Bonapasta, A. A.; Guidoni, L. *J. Am. Chem. Soc.* **2013**, 135, 15353.
(10) Burger, H.; Wannagat, U. *Monatsh. Chem.* **1963**, 94, 1007.
(11) Glazneva, T. S.; Kotsarenko, N. S.; Paukshtis, E. A. *Kinet. Catal.* **2008**, 49(6), 859.
(12) Luo, Y. R. *Comprehensive Handbook of Chemical Bond Energies*, CRC Press, Boca Raton, FL, 2007.
(13) Note that the CoSBA data was adopted from the previously reported manuscript in ref. 7.
(14) Yoon, C. W.; Hirsekorn, K. F.; Neidig, M. L.; Yang, X.; Tilley, T. D. *ACS Catal.* **2011**, 1, 1665.
(15) Nakamoto, K. *Infrared and Raman Spectra of Inorganic and Coordination Compounds*, Wiley, Hoboken, 2009.
(16) Taylor, C. M.; Watson, S. P.; Bryngelson P. A.; Maroney, M. J. *Inorg. Chem.* **2003**, 42, 312.
(17) Goodgame, D. M. L.; Goodgame, M. *Inorg. Chem.* **1965**, 4, 139.
(18) Lim, S.; Ciuparu, D.; Pak, C.; Dobek, F.; Chen, Y.; Harding, D.; Pfefferle, L.; Haller, G. L. *J. Phys. Chem. B* **2003**, 107, 11048.
(19) Takada, S.; Fujii, M.; Kohiki, S. *Nano Lett.* **2001**, 1, 379.
(20) Brunschwig, B. S.; Chou, M. H.; Creutz, C.; Ghosh, P.; Sutin, N. *J. Am. Chem. Soc.* **1983**, 105, 4832.
(21) Zhao, D.; Huo, Q.; Feng, J.; Chmelka, B. F.; Stucky, G. D. *J. Am. Chem. Soc*. **1998**, 120, 6024.
(22) Wang, L. M.; Tian, B. Z.; Fan, J.; Liu, X. Y.; Yang, H. F.; Yu, C. Z.; Tu, B.; Zhao, D. Y. *Micropor. Mesopor. Mater.* **2004**, 67, 123.

Chapter 2. Appendix

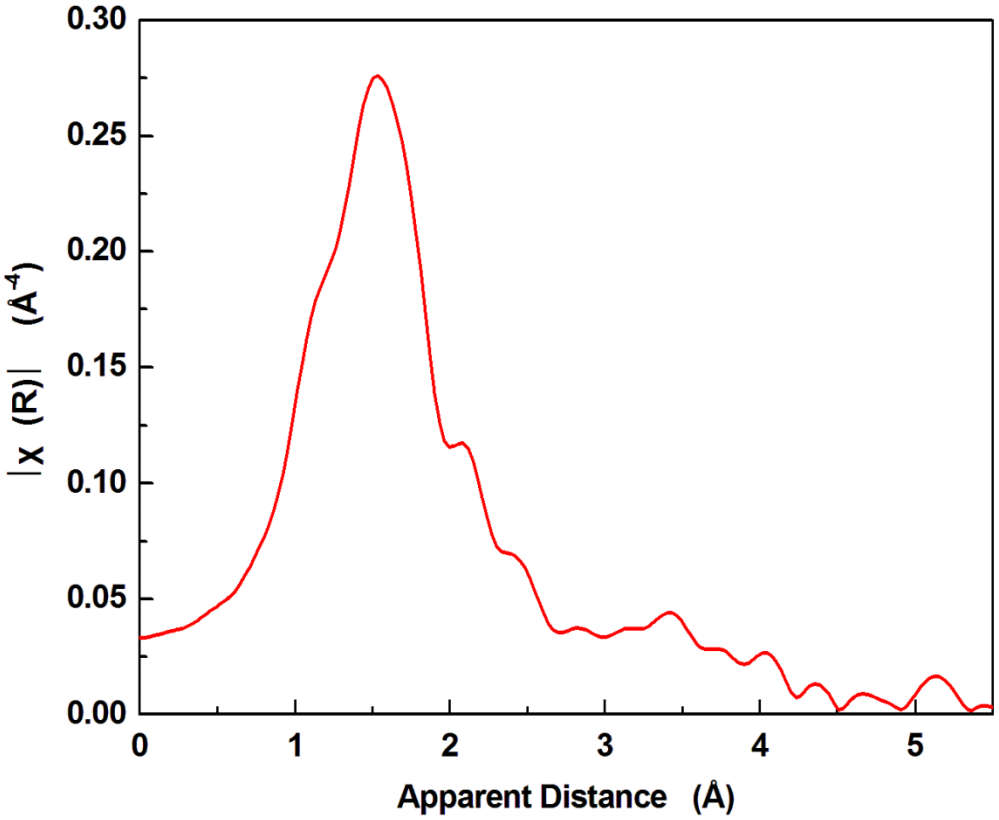

Figure A1. The EXAFS spectrum of CoAlPO.

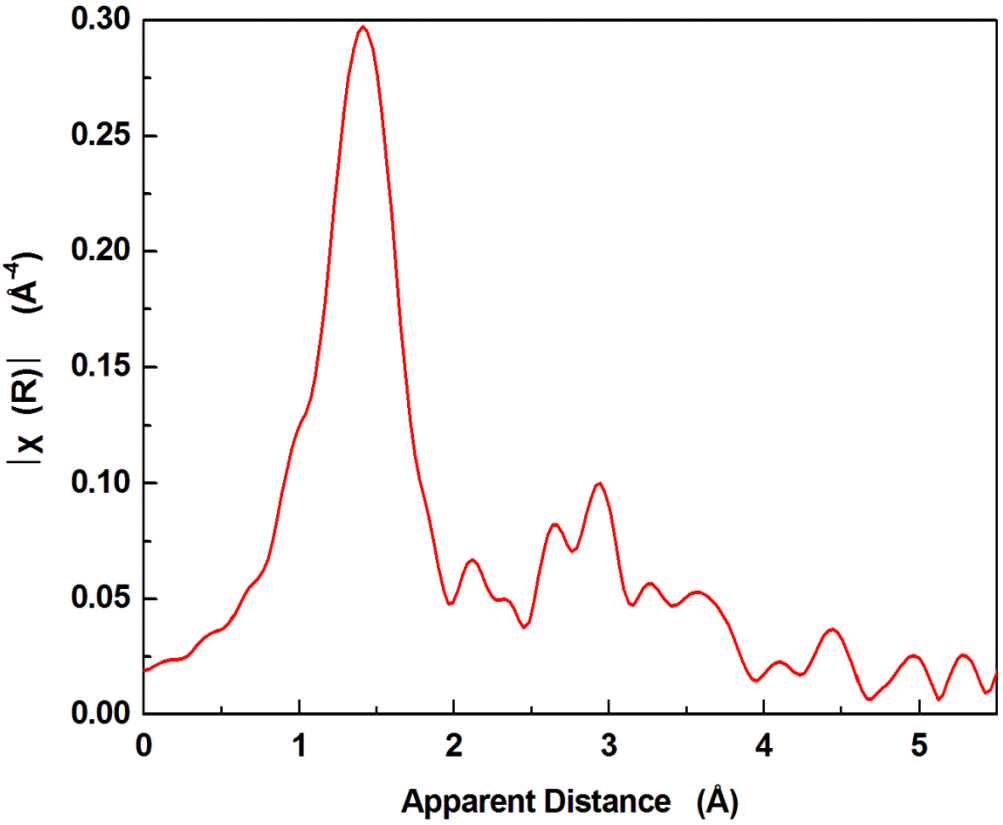

Figure A2. The EXAFS spectrum of CoMgO.

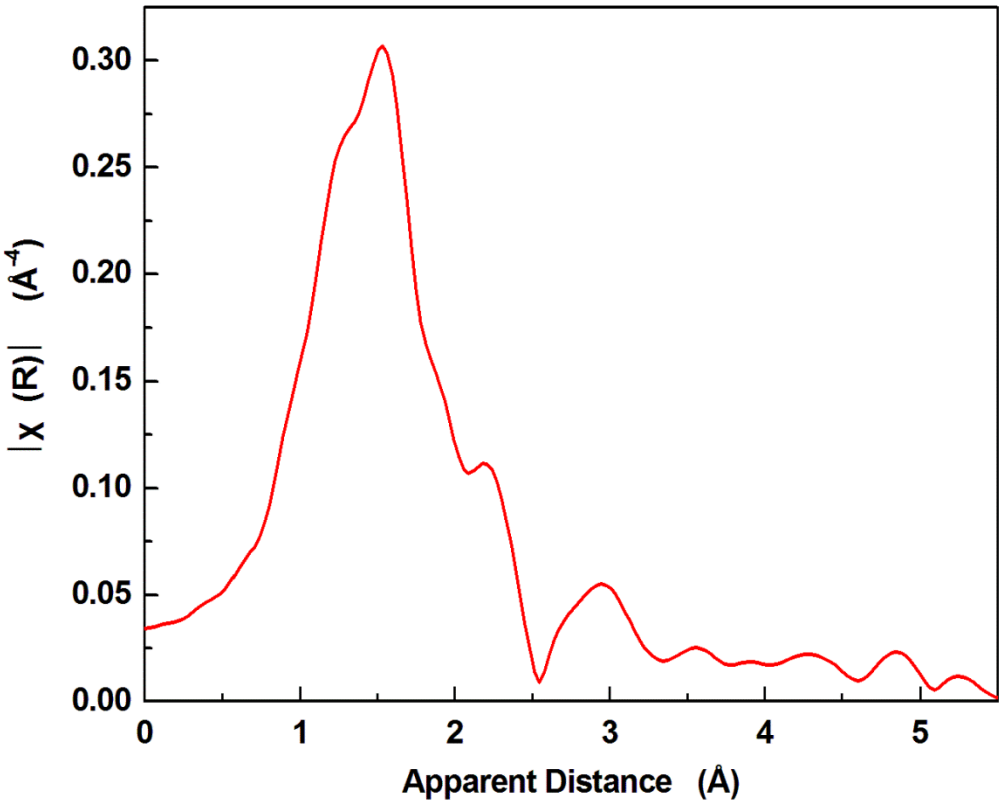

Figure A3. The EXAFS spectrum of $CoTiO_2$.

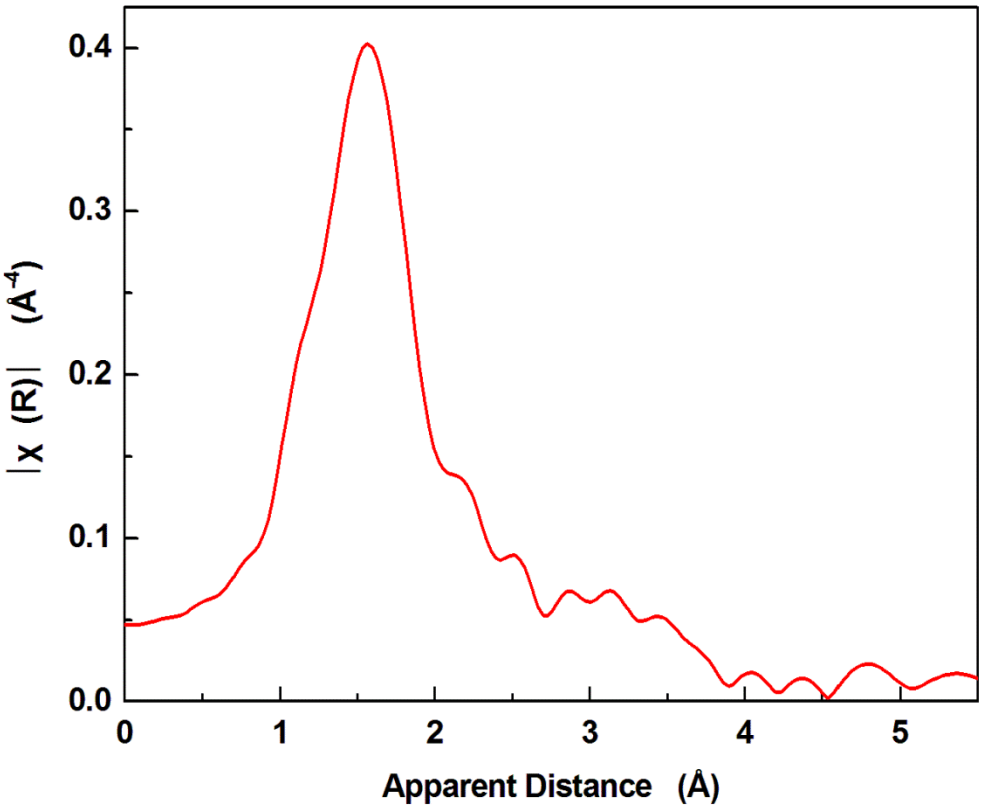

Figure A4. The EXAFS spectrum of CoYZ.

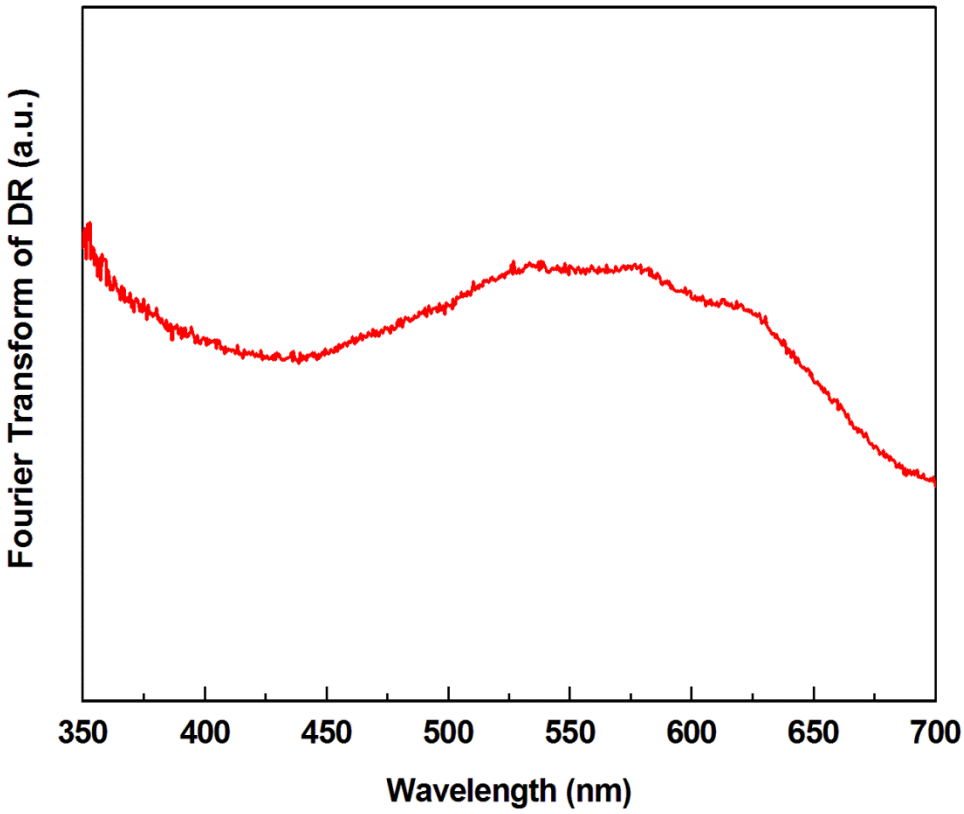

Figure A5. The d-d transition region of the DRUV-vis spectrum of CoAlPO.

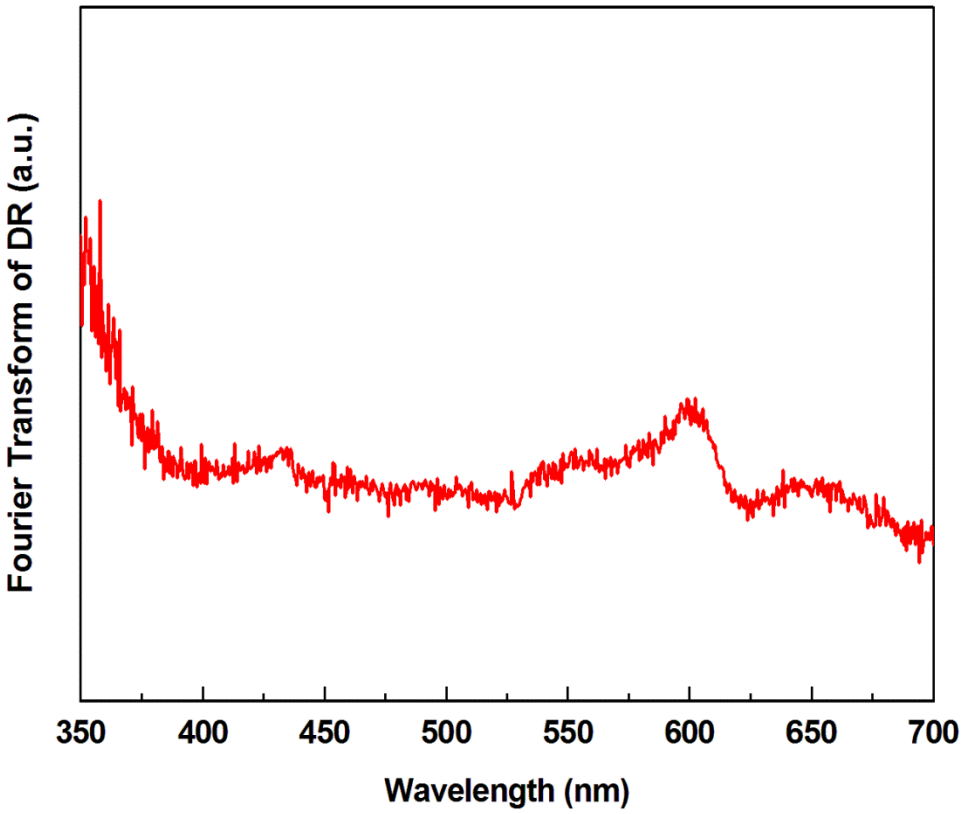

Figure A6. The d-d transition region of the DRUV-vis spectrum of $CoTiO_2$.

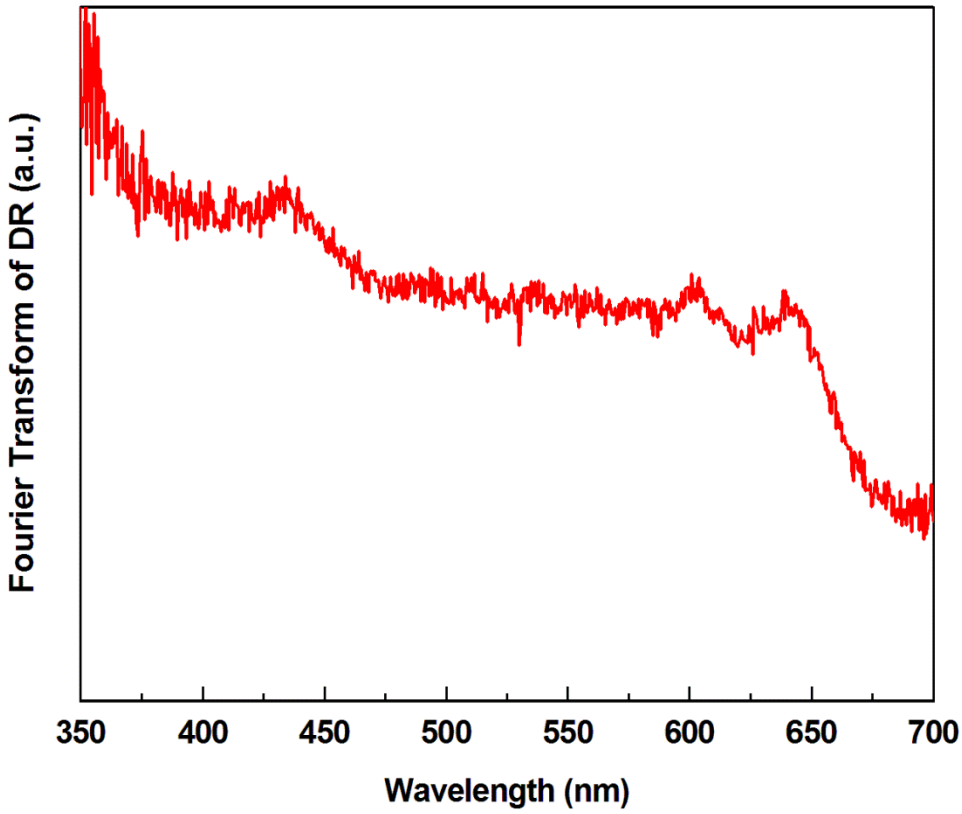

Figure A7. The d-d transition region of the DRUV-vis spectrum of CoYZ.

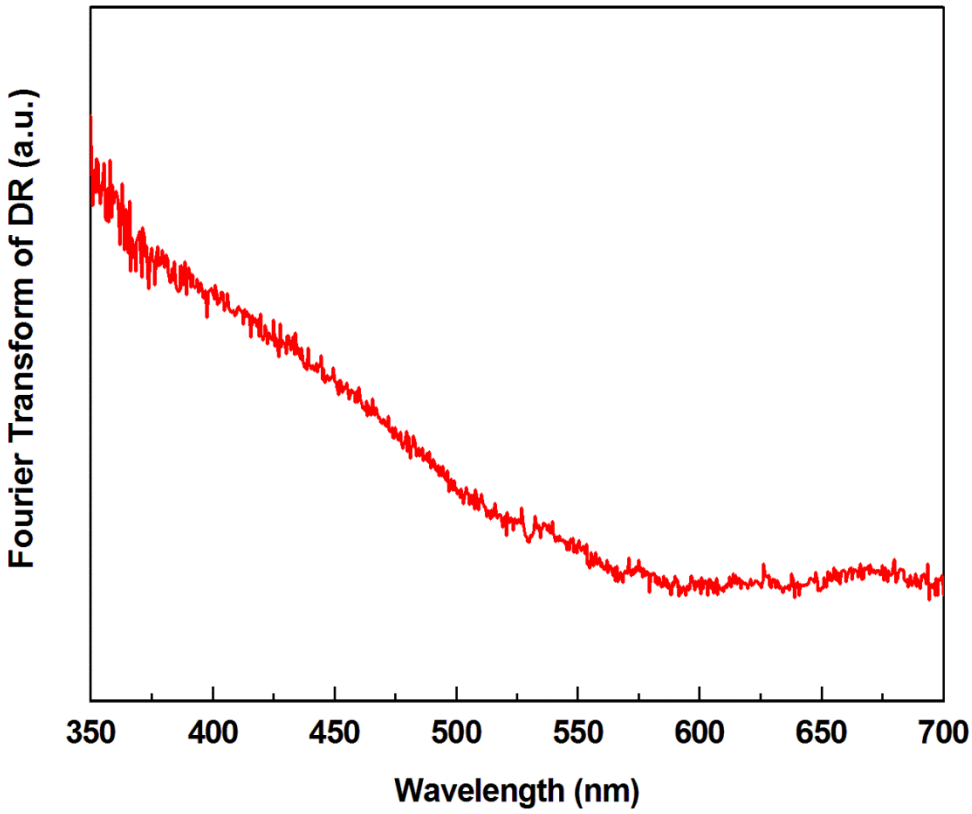

Figure A8. The d-d transition region of the DRUV-vis spectrum of CoMgO.

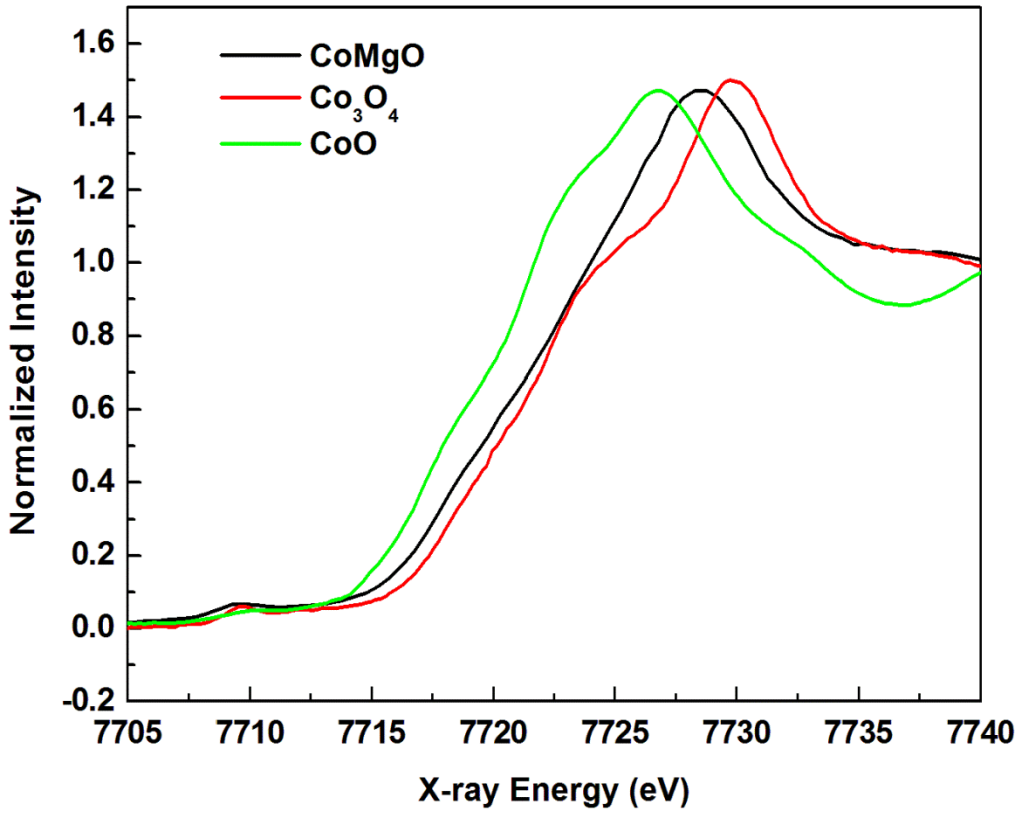

Figure A9. The EXAFS spectra of CoMgO (pre-catalysis) compared to those of CoO and Co_3O_4.

Chapter 3. Electrocatalytic Water Oxidation at Neutral pH by a Nanostructured $Co(PO_3)_2$ Anode

Adapted with permission from Ahn, H. S.; Tilley, T. D. *Adv. Funct. Mater.* **2013**, 23, 227.

Introduction

There is growing interest in development of environmentally benign means for the conversion of solar energy to chemical energy in the form of transportable, storable fuels.[1] Potentially viable artificial photosynthetic systems might involve the oxidation of water to yield oxygen and protons, which may then be employed in an electrocatalytic reduction to produce a chemical fuel (e.g., H_2, CH_4, CH_3OH, etc.). A key technical challenge for enabling such systems is the discovery of efficient catalysts for the oxidative half-reaction that splits water to oxygen and protons. Molecular and heterogeneous catalysts have been developed for this reaction, and many of the most promising results have been provided by compounds and oxides of iridium and ruthenium.[2-10] However, the large-scale application of artificial photosynthesis should be based on less expensive, more abundant metals such as manganese, iron and cobalt.[11-22] Along these lines, considerable attention is being focused on materials and compounds of these metals, and particular interest in cobalt was sparked by a recent report by Nocera and coworkers on a cobalt phosphate material containing oxy-hydroxide layers that operates as an electrocatalytic water-splitting catalyst under neutral pH.[12] Especially given the different electrochemical and chemical properties of this material with respect to those of simple oxides of cobalt such as Co_3O_4 and CoO, it is of interest to investigate additional cobalt materials that incorporate inorganic anions other than oxide.[12,15]

This laboratory has had a long-standing interest in the use of single-source molecular precursors for the synthesis of materials with well-defined stoichiometries. This approach, termed the *thermolytic molecular precursor* (TMP) method, allows synthetic control over a material's phase, composition, and nanostructure.[23] It may be employed in solid- and solution-state transformations to materials, and is amenable to solution processing at low temperatures.[23-26] Previous investigations in this area have targeted phosphate materials of zinc[23b,25d,27,28] and aluminum[23e,25d-e,27-29] with precursor metal complexes of the $-O_2P(O^tBu)_2$ ligand. Well-defined molecular precursors to cobalt phosphate materials are rare, but examples have been reported by Murugavel and coworkers, for conversion to the cobalt phosphates $Co(PO_3)_2$ and $Co_2P_2O_7$.[25a,c] Given the interest in cobalt phosphate materials of controlled stoichiometry and structure, it seems that the TMP approach may provide routes to new water oxidation catalysts with tailored properties.

Herein, we report a nanostructured cobalt metaphosphate material, derived from thermal processing of a molecular precursor, as an electrocatalyst for water oxidation. This nanostructured cobalt metaphosphate catalyst $Co(PO_3)_2$ displays improved stability in neutral pH relative to cobalt oxide, and surpasses it in per-metal efficiency by an order of magnitude at pH 6.4 while exhibiting a lower onset overpotential.

Results and Discussion

Synthesis of $Co(PO_3)_2$ from the single-source molecular precursor $\{Co[O_2P(O^tBu)_2]_2\}_n$ (1)

The polymeric precursor complex $\{Co[O_2P(O^tBu)_2]_2\}_n$ (**1**) was synthesized in high yield by a modification of the literature procedure,[25c] from $CoCl_2 \cdot 6H_2O$ and $KO_2P(O^tBu)_2$ in acetonitrile. The UV-vis spectrum of **1** (Figure A1) is consistent with the presence of Co(II) in a pseudo-tetrahedral environment,[34] and the reported X-ray crystal structure reveals polymeric chains of Co(II) centers bridged alternately by three and then one $-O_2P(O^tBu)_2$ ligand. Compound **1** has not been investigated as a thermolytic precursor to cobalt-based materials, but the related tetra-cobalt species $Co_4(\mu_4\text{-}O)[O_2P(O^tBu)_2]_6$ was shown by Murugavel and coworkers to thermally decompose at 350 ℃ to amorphous $Co_4P_6O_{19}$, which then converts at 850 ℃ to a mixture of $Co(PO_3)_2$ and $Co_2P_2O_7$.[25a,c]

Compound **1** serves as a low-temperature precursor to cobalt metaphosphate, $Co(PO_3)_2$ (*vide infra*), due to the facile thermal elimination of isobutene from the di-*tert*-butyl phosphate ligand.[23] As observed by thermal gravimetric analysis (TGA, Figure A6), precursor **1** undergoes clean thermolysis under a stream of air, with a sharp mass loss of ca. 50% at 138 ℃. The final ceramic yield was 44.4%, which closely corresponds to the calculated yield for $Co(PO_3)_2$ of 45.4%. The identity of the material after thermolysis was confirmed by powder X-ray diffraction (PXRD, Figure A7).[35] This thermolytic decomposition behavior is quite similar to that of the analogous zinc precursor $\{Zn[O_2P(O^tBu)_2]_2\}_n$.[23b] Structural transformations during thermolysis are not apparent by differential scanning calorimetry (DSC, Figure A5), which reveals no significant features to 600 ℃, suggesting that oxide formation and phase separation are unlikely. Characterization of the material by PXRD, UV-Vis spectroscopy, and Raman spectroscopy revealed no evidence for other structures, e.g. oxides or phosphates of cobalt (See the Appendix).

For use of precursor **1** in the preparation of $Co(PO_3)_2$, solution-based methods were investigated as routes to nanoparticles, which should provide a high surface area for the electrocatalytic anode material. Thermal decomposition of a precursor solution in a pressure vessel was selected as the method of catalyst preparation based on the desired properties of the material to be used in electrocatalysis (i.e. high surface area and ease of electrode fabrication). An ethanol solution of precursor **1** (0.5 mM, 15 mL) was placed in a 25 mL pressure reactor, which was then positioned in an oven preset at 240 ℃. The thermal decomposition process is illustrated in Equation 1.

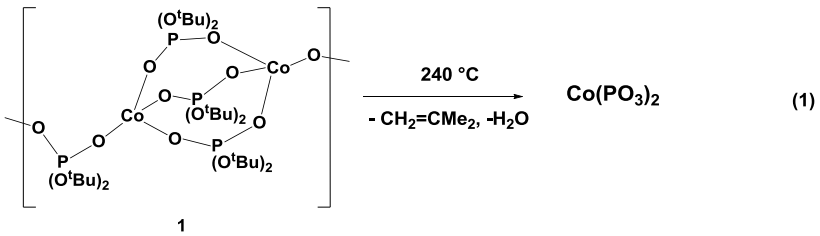

1 (1)

After 12 h, a blue powder that separated from solution was washed with water and acetone, to provide a quantitative yield of nanostructured $Co(PO_3)_2$. The isolated material exhibited a web-like morphology (Figure 1) with an appreciable surface area (20 – 30 m^2/g), and was readily dispersed in an alcohol solvent for solution depositions onto a Ni-foam electrode surface. In a typical electrode fabrication, a 1 mg/mL dispersion of $Co(PO_3)_2$ in ethanol or isopropanol was drop-cast onto Ni-foam (area 1 cm^2) or glassy carbon (3 mm diameter, 0.07 cm^2 area) electrodes. Materials with a higher surface area (up to 160 $m^{2/}g$) were synthesized by addition of a surfactant (e.g., cetrimonium bromide, and Pluronic P123) to the precursor solution prior to thermolysis. However, the resulting materials generally exhibited larger individual (and presumably porous) particles that were difficult to incorporate onto the surface of an electrode.

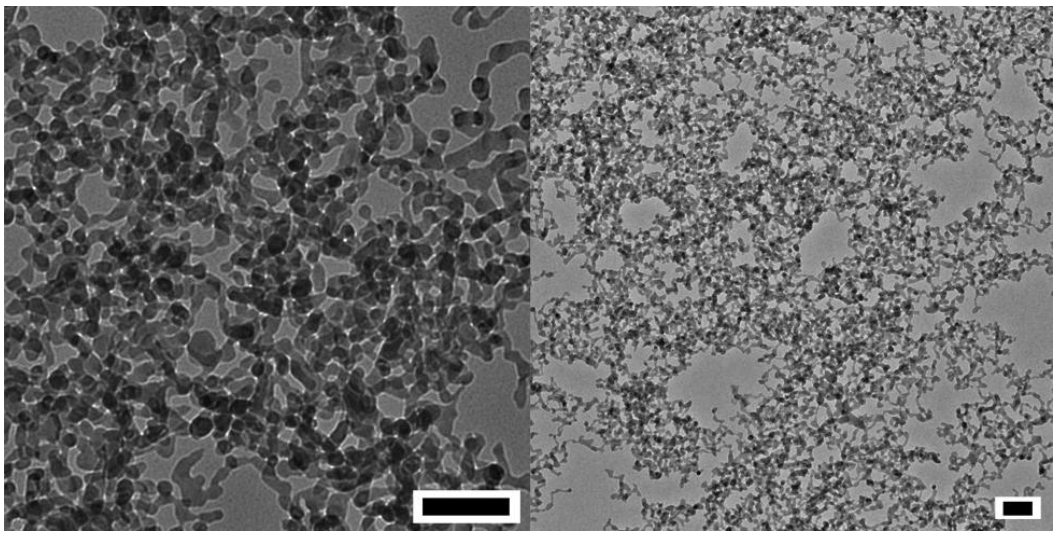

Figure 1. Typical transmission electron microscopy image of web-like $Co(PO_3)_2$. Both scale bars are 100 nm.

Electrocatalytic water oxidation with $Co(PO_3)_2$ nanoparticles

Electrochemical experiments including linear sweep voltammetry (LSV), cyclic voltammetry (CV), and controlled potential electrolysis (CPE) were performed in a two-compartment H-cell with a three-electrode configuration in 0.1 M phosphate-buffered solution with a measured pH of 6.4. Similar electrocatalytic results (*vide infra*) were obtained in acetate buffer at pH 5.6; however, the $Co(PO_3)_2$ catalyst exhibited instability in strongly acidic and basic conditions (pHs lower than 3 and higher than 11). The working electrodes consisted of the catalyst particles deposited onto Ni foam (scanning electron microscopy image shown in Figure A8) or glassy carbon, which were used in combination with a polished platinum wire counter electrode and a Ag/AgCl reference electrode. Over the potential range investigated (up to 1.1 V vs. Ag/AgCl), the Ni foam electrode exhibits no discernible features (Figure 2), such that background corrections were unnecessary, as determined previously in studies with Co_3O_4

nanoparticles.[18] No background correction was applied for electrolysis on the glassy carbon electrode, as it also exhibited no discernible features in the potential range investigated (Figure A10).

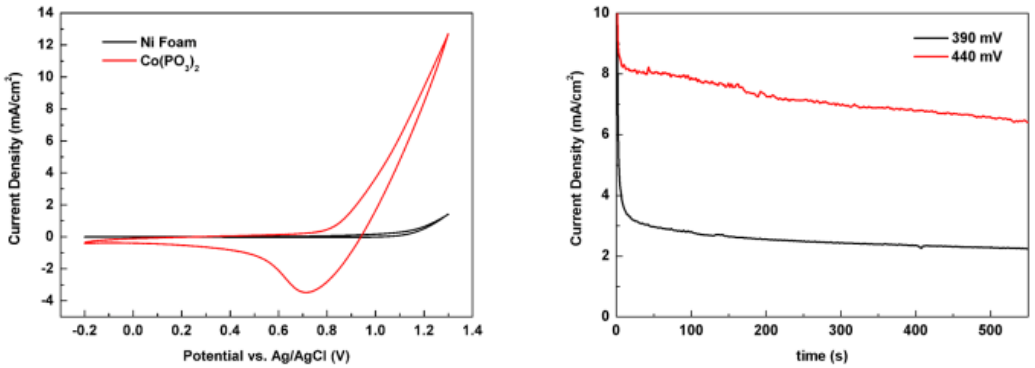

Figure 2. Cyclic voltamogram of nanostructured $Co(PO_3)_2$ at a scan rate of 100 mV/s (left). The CV of blank Ni foam is shown as a reference. Current evolution over time by CPE at overpotentials of 390 mV and 440 mV is shown on the right. The slight drop in current density over time is due to loss of surface area by bubble formation.

As seen in the cyclic voltammogram of the cobalt metaphosphate catalyst on Ni foam (Figure 2), the Co^{II}/Co^{III} and the Co^{III}/Co^{IV} transitions (at ca. 0.7-1.0 V vs. Ag/AgCl) commonly observed prior to catalytic water oxidation[12,18,19] were not well resolved at scan rates higher than 10 mV/s. However, this transition was partially resolved in LSV experiments at a low scan rate of 1 mV/s (Figure A9). From this scan, a charge integration of the presumed Co^{II}/Co^{III} and Co^{III}/Co^{IV} transitions corresponds to ca. four times the number of cobalt atoms in the sample. This appears to be due to the fact that this oxidation is not cleanly separated from water oxidation, unlike in the case of Co_3O_4, and this is consistent with the observed lower onset potential for $Co(PO_3)_2$ (*vide infra*). A similar superpositioning of catalyst and water oxidation was observed for catalyst deposited on glassy carbon electrodes (Figures A10 and A11).

To further examine the onset of electrocatalytic water oxidation for this material, LSV on a flat glassy carbon electrode was utilized at 1 mV/s scan rate. As seen in Figure 3, catalytic current was observed at ca. 0.95 V vs. Ag/AgCl, along with vigorous oxygen bubble formation. Note that the oxidative feature occurring at ca. 0.86 V is the oxidation of the catalyst preceding water oxidation. The catalytic onset potential for the nanostructured $Co(PO_3)_2$ catalyst was determined by the intercept of lines extrapolated from the exchange current and catalysis current in the high overpotential (Tafel) region (See the Appendix for detailed calculations). The onset overpotential determined by this method was 313 mV, which is significantly lower than those associated with Co_3O_4 and CoPi (*vide infra*). The onset potential for a Ni foam electrode decorated with nanostructured $Co(PO_3)_2$ was estimated by measuring steady state currents by CPE at incremental potentials (240 mV to 440 mV in 10 mV increments, Table A1). The resulting overpotential of ca. 300 mV is in good agreement with that determined from a glassy

carbon electrode. An overpotential of ca. 310 mV for the onset of water oxidation catalysis is low for a cobalt-based system.[12-19]

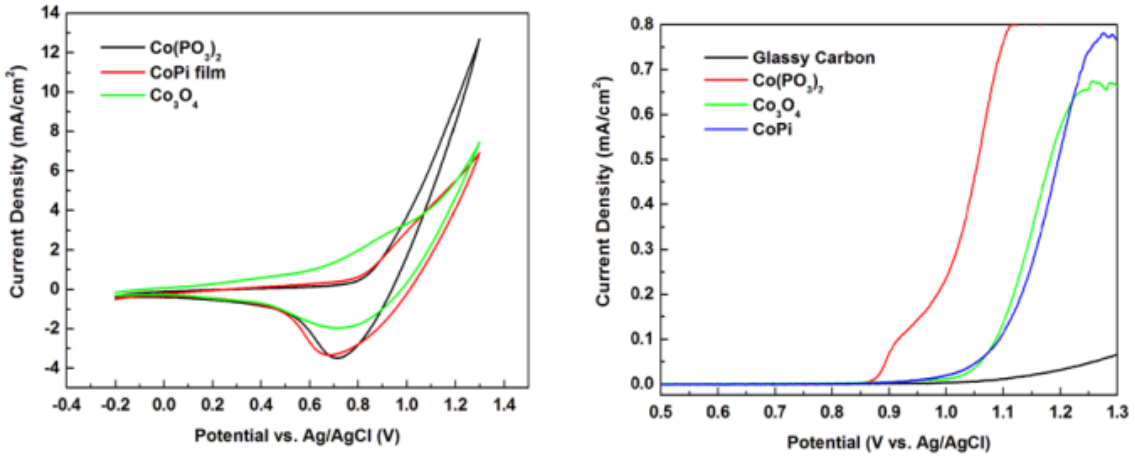

Figure 3. Comparison of CVs of three different materials at a scan rate of 100 mV/s (left). All of them were deposited on Ni foam and the sample loadings were 0.9 mg for Co_3O_4, 1.1 mg for $Co(PO_3)_2$, and 1.2 mg for the CoPi catalyst. LSV of the catalysts in comparison are shown on the right. Catalytic onset of the nanostructured $Co(PO_3)_2$ catalyst at a significantly lower potential was observed. The nonlinearity of the catalytic current at high overpotentials is due to large changes in the electrode area arising from vigorous bubble formation.

For direct comparisons, the same electrochemical experiments were conducted with Co_3O_4 nanoparticles[33] of a similar surface area (d = ca. 20 nm by TEM, BET surface area = 25 m^2/g), and with the cobalt phosphate thin film catalyst (CoPi) described by Nocera and coworkers.[12a] A cyclic voltammogram comparing the electrocatalytic behavior of all three catalysts on Ni foam is shown in Figure 3. The three systems exhibit distinct electrocatalytic behaviors, indicating that despite possible similarities in the composition of the surface layer, the catalytically active sites appear to be distinctly different under oxidizing potentials. Comparisons of the three electrode materials described here must be made on the basis of surface areas, because in general electrocatalytic activity exhibits a strong correlation to the electrode surface area.[18a] The three electrodes compared here were prepared such that their electrochemically active surface areas, as determined by double layer capacitance measurements, were very similar (See the Appendix).[36] Scanning electron microscopy (SEM) images of $Co(PO_3)_2$ and Co_3O_4 particles on Ni foam (Figure A8) reveal similar surface coverages by the respective nanoparticles, corroborating similarities in the capacitances observed electrochemically.

Catalytic onsets for the Co_3O_4 and CoPi catalysts were also determined from the Tafel and exchange current data (Figures 3 and A11 and Table A1). The onset potentials determined in this way, for the Co_3O_4 nanoparticles and the CoPi catalyst, were 414 mV and 434 mV, respectively (100-120 mV greater than that achieved by the cobalt metaphosphate catalyst). A

shift of ca. 100 mV in the onset potential is significant, and implies that the nanostructured $Co(PO_3)_2$ catalyst is inherently more efficient.

Prolonged catalytic activities at higher overpotentials ($\eta \geq 300$ mV) were also investigated by CPE on a Ni foam electrode. Sustained current densities of 0.17, 0.62, 3.30, and 8.01 mA/cm^2 (based on projected electrode surface area) were recorded at η = 300, 340, 390, and 440 mV, respectively (Figures 2 and A12), over at least 8 h. Despite fluctuations in the electrode areas due to excessive bubble formation, several mA of current was observed at moderate overpotentials, which indicates rapid catalysis. A per-metal turnover frequency (TOF) range for the catalyst was calculated from the current densities obtained via CPE and the number of surface sites estimated from the known crystal structures for $Co(PO_3)_2$ and Co_3O_4, the latter of which more closely models the surface active species (*vide infra*) and represents a higher density of surface-exposed cobalt atoms (See the Appendix for detailed calculations). From these measurements, TOF ranges of the cobalt metaphosphate catalyst were determined to be 0.002 - 0.005, 0.008 - 0.016, 0.044 - 0.086, and 0.10 - 0.21 s^{-1} at η = 300, 340, 390, and 440 mV, respectively. These TOF values are higher than those of most cobalt-based water oxidation catalysts operating at similar overpotentials, and an order of magnitude higher than that of Co_3O_4 nanoparticles of similar surface area at pH 6.4.[12-19] The $Co(PO_3)_2$ anode was reevaluated using CV and LSV methods after 1 h of catalysis at 440 mV overpotential, and the voltammograms (both CV and LSV) were unchanged, indicating that the electrochemical behavior was not altered during catalysis. It is worth noting that the nanostructured $Co(PO_3)_2$ catalyst decomposed in strongly acidic and basic conditions (pHs lower than 3 and higher than 11), whereas long-term stability of Co_3O_4 under water oxidation conditions in basic solutions has been reported.[17-19] Different catalysts are associated with characteristic pH ranges for which optimal catalytic performance and stability is observed, and the nanostructured $Co(PO_3)_2$ catalyst is most effective at near neutral pHs.

Oxygen detection experiments were conducted to determine the Faradaic efficiencies associated with the catalytic current. Electrolysis experiments were conducted in a gas-tight H-cell, while the headspace oxygen concentration was monitored by a multi-frequency fluorescence oxygen probe. Faradaic efficiencies of 98 ± 4 % were obtained at η = 440 mV, indicating that within experimental error all of the current is consumed for oxygen evolution (Figure 4).

The high overpotential (Tafel) region of the current-voltage plot is shown in Figure 4. The Tafel slope for the $Co(PO_3)_2$ catalyst is 74.1 mV/dec, suggesting that it operates by a mechanism similar to that of metal oxides. The actual Tafel slope may be lower, since the electrode surface area is reduced during catalysis by bubble formation. Attempts to make similar measurements on Co_3O_4 nanoparticles were unsuccessful due to the limited stability of this material at the experimental pH of 6.4.[17]

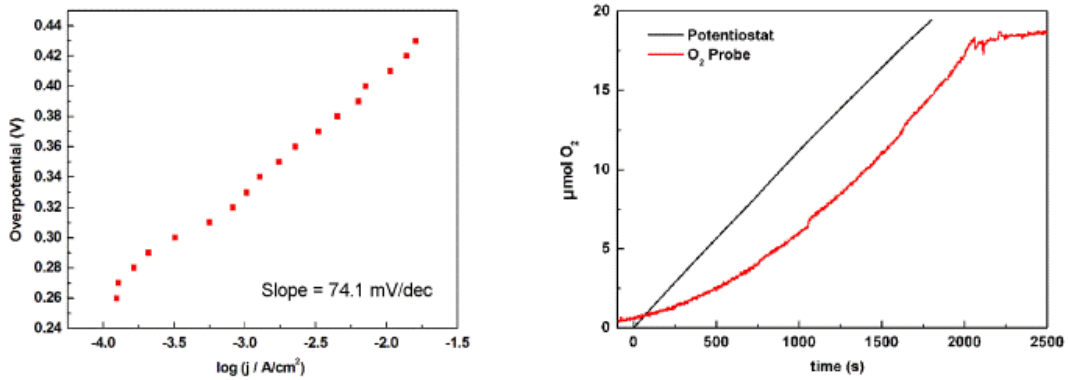

Figure 4. Tafel plot of $Co(PO_3)_2$ (left), with a slope of 74.1 mV/dec (η = applied voltage – thermodynamic potential). A test of Faradic efficiency by simultaneous detection of headspace O_2 with CPE is presented on the right. Faradaic efficiencies of 98 ± 4 % were recorded over multiple experiments. The time lag between the two curves is due to adhesion of bubbles on the porous electrode, giving rise to detection delay by the probe in the reactor headspace.

Post-catalytic characterization of the catalyst

To investigate structural changes associated with the electrocatalysis, the catalysts were examined after catalytic runs. Raman spectroscopy was performed on the catalyst prior to application of an oxidizing bias, and again after a potential of 1.1 V (vs. Ag/AgCl) had been applied over the course of one hour (Figure 5). Before electrocatalysis, the Raman spectrum exhibited only bands attributed to cobalt metaphosphate at 475, 665, 980, and 1095 cm^{-1} (Figure 5).[38] After catalysis, Raman bands for the metaphosphate are less prominent, and a broad feature at 597 cm^{-1}, assigned to Co-O stretches, indicates the presence of surface CoO_x species.[39]

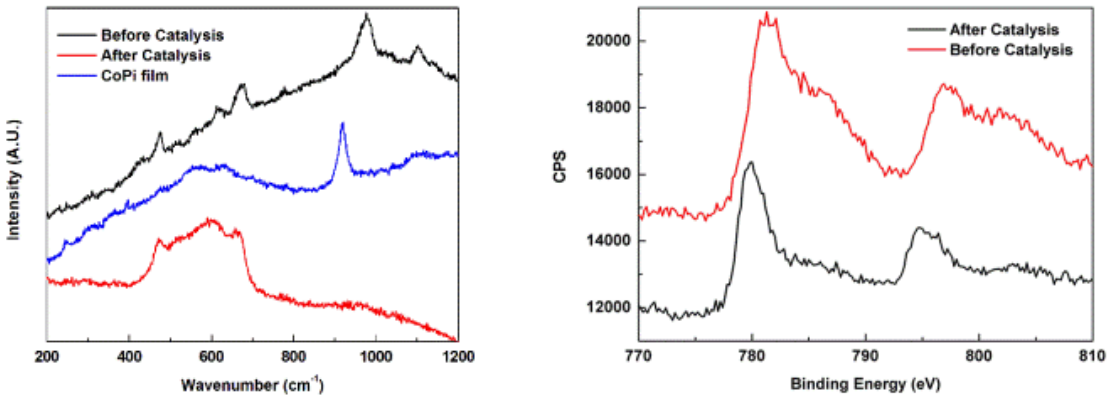

Figure 5. Raman spectra of $Co(PO_3)_2$ as synthesized and after being utilized in catalysis are displayed alongside that of the CoPi film catalyst (left). The cobalt 2p region of the XPS spectrum of $Co(PO_3)_2$ prior to and after catalysis exhibits diminished shoulder peaks due to the oxidation of cobalt centers (right).

Given the similar compositions of the CoPi and $Co(PO_3)_2$ catalysts, it was of interest to compare their structural features after catalysis. The post-catalytic Raman spectra of these catalysts exhibit distinct differences (Figure 5). Weak and broad bands at ca. 550 and 620 cm^{-1} are observed for the CoPi catalyst, similar to Co-O stretches seen in Co_3O_4.[17,39c] Note that the surface-bound active sites for the CoPi catalyst are thought to consist of cubane-like cobalt oxide clusters, as evidenced by X-ray absorption spectroscopy.[12e,f] The most distinctive feature in the post-catalytic $Co(PO_3)_2$ sample is a broad peak at 597 cm^{-1}, which has previously been assigned to the presence of amorphous CoO_x species.[39] Diminishment of the peak at 980 cm^{-1} due to PO_4^{3-} tetrahedral is also consistent with surface enrichment by CoO_x layer species (*vide infra*). Thus, the active surface species in this material may be small CoO_x domains, perhaps similar to those associated with the CoPi catalyst, supported by the underlying $Co(PO_3)_2$ structure. The distinct differences in the electrocatalytic behaviors for the CoPi and $Co(PO_3)_2$ catalysts (*vide supra*) may therefore be attributed to the influence of active site-support interactions, which may lead to different structures for the surface-bound sites under catalytic conditions.

Evidence for cobalt oxide species in the post-catalytic material was also found by X-ray Photoelectron Spectroscopy (XPS, Figures 5 and A13). Prior to catalysis, $2p_{1/2}$ and $2p_{3/2}$ XPS peaks for Co at 780.0 and 795.2 eV, with broad shoulders at 786.0 and 801.6 eV, are observed (Figure 5). The broad shoulder features indicate that most of the Co centers of the $Co(PO_3)_2$ nanoparticles are in the Co(II) oxidation state.[40,41] After catalysis, the shoulder peaks at 786.0 and 801.6 eV are greatly diminished, indicating that most of the Co centers detected had been converted to higher oxidation states.[40] Analysis of the post-catalytic material by XPS also indicates the presence of phosphate at or near the surface, as shown by a phosphorous 2p peak at 133 eV (Figure A13).[38] The stoichiometry of the post-catalysis material was estimated by integration of the XPS spectrum, which gave a Co:P:O ratio of 4:1:9.9 (Table A2). These values reflect enrichment of cobalt and oxygen at the surface; for comparison the measured ratio for pre-catalytic $Co(PO_3)_2$, determined by XPS analysis, is 1:1.9:6.8. These results from Raman and XPS studies are consistent with a restructuring of the surface with formation of oxide-like species during electrocatalysis. The Pourbaix diagram for Co in phosphate-buffered solutions[15b,42] suggest that $Co(PO_3)_2$ nanoparticles will not be completely stable under electrocatalytic conditions at pH 6.4, and that surface formation of $Co(OH)_2$ should occur, followed by conversion to oxide species under an oxidizing bias. The post-catalytic material was examined by several methods. Analysis by XRD proved difficult due to strong attachment of the catalyst particles onto the electrode. Inductively coupled plasma optical emission spectroscopy (ICP-OES) revealed that the cobalt and phosphorous compositions were 27.7 and 28.4 wt%, respectively, in agreement with the expected composition of $Co(PO_3)_2$ (27.2 wt% Co and 28.6 wt% P). A negligible incorporation of potassium from the buffer solution (0.7 wt%) also suggests that the transformation to an oxide-like species occurs only at the surface while the bulk $Co(PO_3)_2$ structure remains. The post-catalytic material also exhibits the Raman peak at 665 cm^{-1} (Figure 3), characteristic of $Co(PO_3)_2$ and previously assigned to a symmetric stretching frequency for

bridging P-O groups in long-chain polyphosphates.[38a] This also suggests that the underlying $Co(PO_3)_2$ structure is unaltered during catalysis and surface transformations.

It should be noted that the oxide species observed by Raman spectroscopy and XPS, detected without applied potential, are likely not those directly involved in catalysis. Under the oxidizing potentials used for catalysis, the Pourbaix diagram of cobalt in phosphate-buffered water[15b,42] predicts the formation of high oxidation state species such as CoO_2 and $Co(OH)_3$. Similar chemical species, presumed to be present at the surface of the $Co(PO_3)_2$-based anode during catalysis, may then transform in the absence of the oxidizing bias to the cobalt oxide species detected by spectroscopy. Surface rearrangement phenomena in Co_3O_4 and CoPi water oxidation systems have been investigated by various researchers, and the formation of a double layer, hydroxide-type structure, Co(O)OH, has been observed by Raman and X-ray absorption spectroscopies.[12e,15b,17] It is likely that a similar surface transformation is occurring in the nanostructured $Co(PO_3)_2$ catalyst, based on the Raman and XPS data. However, given the distinct behavior of the nanostructured $Co(PO_3)_2$ catalyst (in terms of catalytic rate and onset overpotential), it is possible that the observed enhancement is due to a synergistic effect of the underlying $Co(PO_3)_2$ structure on the catalytically active surface CoO_x species. In situ vibrational and X-ray absorption spectroscopies should further reveal the structure of the active species, and such experiments are planned for the near future.

Conclusions

The studies described above demonstrate a convenient molecular precursor route to nanostructured cobalt metaphosphate materials. In addition, nanoparticles of $Co(PO_3)_2$ have been shown to function as an electrocatalyst for water oxidation, at a relatively low overpotential of about 310 mV. A per-metal turnover frequency of 0.10 - 0.21 s^{-1} at η = 440 mV is comparable to the highest rate reported for a first-row metal heterogeneous system for water oxidation,[11-19,21c,22] and this represents a substantially higher rate than that observed for Co_3O_4 and CoPi catalysts of similar surface areas at pH 6.4 (0.011 and 0.0026 s^{-1}, respectively, at similar overpotentials).[12d,43]

Spectroscopic studies indicate that the surface of the $Co(PO_3)_2$-based electrocatalyst undergoes restructuring during electrocatalysis, resulting in bound CoO_x species supported by the underlying $Co(PO_3)_2$ structure. The anion in the catalyst material, as well as the nature of the interaction between the catalytic, surface-bound species and the support material appear to play roles in water oxidation catalysis, as evidenced by the distinct electrocatalytic behaviors observed for Co_3O_4, CoPi, and $Co(PO_3)_2$. Thus, investigations of cobalt-based inorganic materials with a range of anions should help to develop structure-function relations and point the way to more efficient catalysts.

Experimental

General. Nitrogen adsorption isotherms were obtained using a Quantachrome Autosorb 1, with samples outgassed at 120 ℃ for at least 20 h prior to data collection. The BET method was used for surface area determination and the BJH method was used for pore size distribution calculations.[30,31] TGA-DSC measurements were conducted using a Seiko Exstar6000 brand TG/DTA6300 analyzer coupled to a Pfeiffer Thermostar mass spectrometer. Carbon, hydrogen, and nitrogen elemental analyses were performed at the College of Chemistry microanalysis laboratory at the University of California, Berkeley. DR-FTIR spectra were obtained on a Mattson FTIR spectrometer. The DRUV-Vis spectrum was acquired using a Perkin-Elmer Lambda 9 spectrometer equipped with a 60 mm integrating sphere, a slit width of 4 nm, and at a collection speed of 120 nm/min. Samples were run using MgO as a reference background. Powder X-ray diffraction (PXRD) patterns were recorded on a Bruker D-8 GADDS X-ray diffractometer using Co Kα radiation (λ = 1.7902 Å). pH measurements were conducted using a Thermo Orion 2 star pH meter. Electrochemical data were recorded on a Bioanalytical Systems model EC epsilon computer-controlled potentiostat. Unless otherwise stated, all measurements were conducted in a two-compartment H-cell with a three-electrode configuration. Electrochemistry experiments were performed on solutions buffered with 0.1 M phosphate (NaH_2PO_4/Na_2HPO_4 measured pH of 6.4) referenced to a Ag/AgCl reference electrode. Ag/AgCl electrodes were calibrated relative to Potassium Ferricyanide in order to correct for any potential drifts. Solution resistance in CV and LSV experiments was corrected for by the iR compensation algorithm, using software in the EC epsilon potentiostat. Polished platinum wire was used as an auxiliary electrode, and catalyst deposited onto Ni foam or glassy carbon was used as a working electrode. The catalyst was loaded onto the Ni foam by drop-casting of a 1 mg/mL solution (in ethanol) to achieve a loading of 1 ± 0.1 mg/cm^2 (confirmed by determining the change in mass with an analytical balance). For electrolysis on a flat electrode, glassy carbon with a 3 mm diameter was utilized, also by drop-casting catalysts. Transmission electron microscopy (TEM) was performed on a Hitachi H-7650 TEM operating at 120 kV. Scanning electron microscopy (SEM) was performed on a JEOL Field Emission SEM operating at 5 kV. Raman experiments were performed on an epi-illumination confocal Raman microscope (LabRam HR, Horiba Jobin, Yvon) with HeNe laser (1mW) at 633 nm as an excitation source. Inductively coupled plasma optical emission spectroscopy (ICP-OES) for cobalt ion detection in post catalytic solutions was performed on a Perkin-Elmer ICP-OES Optima 7000 DV. Standard solutions were purchased from Perkin-Elmer and used as received. X-ray photoelectron spectroscopy (XPS) was performed on a Perkin-Elmer PHI 5300 ESCA system with a Mg anode driven at 100 W. The compound $KO(O)P(O^tBu)_2$ was prepared according to literature procedures.[32] Cobalt oxide (Co_3O_4) nanoparticles used in comparison experiments were prepared according to literature procedures.[33] The CoPi water oxidation catalyst was prepared according to a literature procedure,[12a] via direct deposition onto the electrode substrate.

Synthesis of $\{Co[O_2P(O^tBu)_2]_2\}_n$ (1). The synthesis of $\{Co[O_2P(O^tBu)_2]_2\}_n$ was conducted using a modified preparation reported by Murugavel et. al.[25a,25c] In a typical synthesis, $KO(O)P(O^tBu)_2$ (4.97 g, 20 mmol) was dissolved in acetonitrile (ca. 25 mL). An acetonitrile (15 mL) solution of $CoCl_2 \cdot 6H_2O$ (2.38 g, 10 mmol) was then added. An instant color change to blue and precipitation of KCl was observed. Product was obtained in greater than 80% yield by crystalization from slowly evaporating diethyl ether under N_2. Anal. Calcd: C, 40.26; H, 7.60; Co, 12.34. Found: C, 40.13; H, 7.82; Co, 12.11. IR (DRIFTS, KBr, cm^{-1}) 1564 (m), 1419 (w), 1375 (w), 1367 (m), 1191 (m), 1174 (s), 1072 (s), 993 (m), 916 (w), 831 (w), 700 (w), 547 (w).

Synthesis of $Co(PO_3)_2$. Nanometer sized web-like $Co(PO_3)_2$ material was synthesized by thermal decomposition of **1** in a pressure reactor. An ethanol solution of **1** (ca. 0.5 mM, 15 mL) was placed in a Teflon-lined Parr Instrument 4744 general purpose pressure reactor, which was then sealed and placed in an oven heated to 240 ℃ for 8 h. The resulting material was removed from the reactor, washed with water, acetone, and ethanol multiple times with centrifugation. The resulting material was dispersed in ethanol or isopropanol (1 mg/mL) for working electrode fabrication.

References

(1) Lewis, N. S.; Nocera, D. G. *Proc. Nat. Acad. Sci.* **2006**, 103, 15729.

(2) (a) Kiwi, J.; Grätzel, M. *Angew. Chem. Int. Ed*. **1978**, 17, 860. (b) Lehn, J. M.; Sauvage, J. P.; Ziessel, R. *Nouv. J. Chim*. **1980**, 4, 355. (c) Harriman, A.; Pickering, I. J.; Thomas, P. A.; Christensen, J. *Chem. Soc. Faraday Trans. 1* **1988**, 84, 2795.

(3) (a) Hara, M.; Waraksa, C. C.; Lean, J. T.; Lewis, B. A.; Mallouk, T. E. *J. Phys. Chem. A* **2000**, 104, 5275. (b) Hara, M.; Lean, J. T.; Mallouk, T. E. *Chem. Mater*. **2001**, 13, 4668. (c) Morris, N. D.; Suzuki, M.; Mallouk, T. E. *J. Phys. Chem. A* **2004**, 108, 9115. (d) Hoertz, P. G.; Kim, Y. I.; Youngblood, W. J.; Mallouk, T. E. *J. Phys. Chem. B* **2007** 111, 6845.

(4) (a) Nakagawa, T.; Beasley, C. A.; Murray, R. W. *J. Phys. Chem. C* **2009**, 113, 12958. (b) , T.; Bjorge, N. S.; Murray, R. W. *J. Am. Chem. Soc.* **2009**, 131, 15578.

(5) Yagi, M.; Tomita, E.; Sakita, S.; Kuwabara, T.; Nagai, K. *J. Phys. Chem. B* **2005**, 109, 21489.

(6) (a) Hull, J. F.; Balcells, D.; Blankmore, J. D.; Incarvito, C. D.; Eisenstein, O.; Brudvig, G. W.; Crabtree, R. H. *J. Am. Chem. Soc.* **2009**, 131, 8730. (b) Blakemore, J. D.; Schley, N. D.; Balcells, D.; Hull, J. F.; Olack, G. W.; Incarvito, C. D.; Eisenstein, O.; Brudvig, G. W.; Crabtree, R. H. *J. Am. Chem. Soc.* **2010**, 132, 16017.

(7) King, N. C.; Dickinson, C.; Zhou, W.; Bruce, D. W. *Dalton Trans.* **2005**, 1027.

(8) (a) Sens, C.; Romero, I.; Rodríguez, M.; Llobet, A.; Parella, T.; Benet-Buchholz, J. *J. Am. Chem. Soc*. **2004**, 126, 7798. (b) Romain, S.; Bozoglian, F.; Sala, X.; Llobet, A. *J. Am. Chem. Soc.* **2009**, 131, 2768.

(9) (a) Tong, L.; Duan, L.; Xu, Y.; Privalov, T.; Sun, L. *Angew. Chem. Int. Ed.* **2010**, 49, 1. (b) Duan, L.; Xu, Y.; Zhang, P.; Wang, M.; Sun, L. *Inorg. Chem.* **2010**, 49, 209. c) Xu, Y.; Fisher, A.; Duan, L.; Tong, L.; Gabrielsson, E.; Åkermark, B.; Sun, L. *Angew. Chem. Int. Ed.* **2010**, 49, 8934.

(10) (a) Concepcion, J. J.; Jurss, J. W.; Templeton, J. L.; Meyer, T. J. *J. Am. Chem. Soc.* **2008**, 130, 16462. (b) Chen, Z. F.; Concepcion, J. J.; Jurss, J. W.; Meyer, T. J.; *J. Am. Chem. Soc.* **2009**, 131, 15580.

(11) Brunschwig, B. S.; Chou, M. H.; Creutz, C.; Ghosh, P.; Sutin, N. *J. Am. Chem. Soc.* **1983**, 105, 4832.

(12) (a) Kanan, M. W.; Nocera, D. G. *Science* **2008,** 321, 1072. (b) Surendranath, Y.; Dincă, M.; Nocera, D. G. *J. Am. Chem. Soc.* **2009**, 131, 2615. (c) Kanan, M. W.; Surendranath, Y.; Nocera, D. G. *Chem. Soc. Rev*. **2009**, 38, 109. (d) Surendranath, Y.; Kanan, M. W.; Nocera, D. G. *J. Am. Chem. Soc.* **2010**, 132, 16501. (e) Kanan, M. W.; Yano, J.; Surendranath, Y.; Dincă, M.; Yachandra, V. K.; Nocera, D. G. *J. Am. Chem. Soc.* **2010**, 132, 13692. f) Risch, M.; Khare, V.; Zaharieva, I.; Gerencser, L.; Chernev, P.; Dau, H. *J. Am. Chem. Soc.* **2009**, 131, 6936. g) Esswein, A. J.; Surendranath, Y. S.; Reece, S. Y.; Nocera, D. G. *Energy Environ. Sci.* **2011**, 4, 499.

(13) (a) Zhong, D. K.; Sun, J.; Inumaru, H.; Gamelin, D. R. *J. Am. Chem. Soc.* **2009**, 131, 6086. (b) Zhong, D. K.; Gamelin, D. R. *J. Am. Chem. Soc.* **2010**, 132, 4202.

(14) (a) Steinmiller, E. M. P.; Choi, K. S. *Proc. Natl. Acad. Sci. U.S.A.* **2009**, 106, 20633. (b) Seabold, J. A.; Choi, K. S. *Chem. Mater.* **2011**, 23, 1105. (c) McDonald, K. J.; Choi, K. S. *Chem. Mater.* **2011**, 23, 1686.

(15) (a) Gerken, J. B.; Landis, E. C.; Hamers, R. J.; Stahl, S. S. *ChemSusChem* **2010**, 3, 1176.

(b) Gerken, J. B.; McAlpin, J. G.; Chen, J. Y. C.; Rigsby, M. L.; Casey, W. H.; Britt, R. D.; Stahl, S. S. *J. Am. Chem. Soc.* **2011**, 133, 14431.
(16) Jiao, F.; Frei, H. *Angew. Chem. Int. Ed.* **2009**, 48, 1841.
(17) Yeo, B. S.; Bell, A. T. *J. Am. Chem. Soc.* **2011**, 133, 5587.
(18) (a) Esswein, A. J.; McMurdo, M. J.; Ross, P. N.; Bell, A. T.; Tilley, T. D. *J. Phys. Chem. C* **2009**, 113, 15068. (b) Chou, N. H.; Ross, P. N.; Bell, A. T.; Tilley, T. D. *ChemSusChem* **2011**, 4, 1566.
(19) Singh, R. N.; Mishra, D.; Sinha, A. S. K.; Singh, A. *Electrochem. Commun.* **2007**, 9, 1369.
(20) (a) Yin, Q.; Tan, J. M.; Bessen, C.; Geletii, Y. V.; Musaev, D. G.; Kuznetsov, A. E.; Luo, Z.; Hardcastle, K. I.; Hill, C. L. *Science*, **2010**, 328, 342. (b) Huang, Z.; Luo, Z.; Geletii, Y. V.; Vickers, J. W.; Yin, Q.; Wu, D.; Hou, Y.; Ding, Y.; Song, J.; Musaev, D. G.; Hill, C. L.; Lian, T. *J. Am. Chem. Soc.* **2011**, 133, 2068.
(21) (a) Wu, J.-Z.; Angelis, F. D.; Carrell, T. G.; Yap, G. P. A.; Sheats, J.; Car, R.; Dismukes, G. C. *Inorg. Chem.* **2006**, 45, 189. (b) Brimblecombe, R.; Wiegers, G. F.; Dismukes, G. C.; Spiccia, L. *Angew. Chem. Int. Ed.* **2008**, 47, 7335. (c) Hocking, R. K.; Brimblecombe, R.; Chang, L.; Singh, A.; Cheah, M. H.; Glover, C.; Casey, W. H.; Spiccia, L. *Nat. Chem.* **2011**, 3, 461.
(22) Poulsen, A. K.; Rompel, A.; McKenzie, C. J. *Angew. Chem. Int. Ed.* **2005**, 44, 6916.
(23) (a) Terry, K. W.; Lugmair, C. G.; Tilley, T. D. *J. Am. Chem. Soc.* **1997**, 119, 9745. (b) Lugmair, C. G.; Tilley, T. D.; Rheingold, A. L. *Chem. Mater.* **1997**, 9, 339. (c) Lugmair, C. G.; Tilley, T. D. *Inorg. Chem.* **1998**, 37, 6304. (d) Lugmair, C. G.; Tilley, T. D.; Rheingold, A. L. *Chem. Mater.* **1999**, 11, 1615. (e) Kriesel, J. W.; Sanders, M. S.; Tilley, T. D. *Adv. Mater.* **2001**, 13, 331. (f) Kriesel, J. W.; Sanders, M. S.; Tilley, T. D. *Chem. Mater.* **2001**, 13, 3554. g) Fujdala, K. L.; Tilley, T. D. *J. Catal.* **2003**, 216, 265; h) Fujdala, K. L.; Brutchey, R. L.; Tilley, T. D. in *Topics in Organometallic Chemistry*, Vol. 16 (Eds: C. Copéret, B. Chaudret), Springer-Verlag, New York, U.S.A **2005**, pp. 69-116.
(24) (a) *Ultrastructure Processing of Advanced Materials*; Uhlmann, D. R., Ulrich, D. R., Eds.; Wiley-Interscience: New York, 1992. (b) *Better Ceramics Through Chemistry V*; Materials Research Society Symposia Proceedings, Vol 271; Hampden-Smith, M. J., Klemperer, W. G., Brinker, C. J., Eds.; Materials Research Society: Pittsburgh, 1992. (c) *Inorganic Materials*; Bruce, D. W., O'Hare, D., Eds.; Wiley: New York, 1992. (d) Kahn, M. L.; Glaria, A.; Pages, C.; Mongo, M.; Macary, L. S.; Maisonnat, A.; Chadret, B. *J. Mater. Chem.* **2009**, 19, 4044.
(25) (a) Murugavel, R.; Sathiyendiran, M.; Walawalkar, M. G. *Inorg. Chem.* **2001**, 40, 427. (b) Sathiyendiran, M.; Murugavel, R. *Inrog. Chem.* **2002**, 41,6404. (c) Pothiraja, R.; Sathiyendiran, M.; Butcher, R. J.; Murugavel, R. *Inorg. Chem.* **2004**, 43, 7585. (d) Murugavel, R.; Choudhury, A.; Walawalkar, M. G.; Pothiraja, R.; Rao, C. N. R. *Chem. Rev.* **2008**, 108, 3549. (e) Murugavel, R.; Gogoi, N. *J. Organomet. Chem.* **2010**, 695, 916.
(26) (a) Meyer, F.; Hempelmann, R.; Mathur, S.; Veith, M. *J. Mater. Chem.* **1999**, 9, 1755. (b) Swamy, K. C. K.; Veith, M.; Huch, V.; Mathur, S. *Inorg. Chem.* **2003**, 42, 5837.
(27) Gier, T. E.; Stucky, G. D. *Nature* **1991**, 349, 508.
(28) Cao, G.; Hong, H-G.; Mallouk, T. E. *Acc. Chem. Res.* **1992**, 25, 420.
(29) Kimura, T. *Micropo. Mesopor. Mat.* **2005**, 77, 97.
(30) Brunauer, S.; Emmett, P. H.; Teller, E. *J. Am. Chem. Soc*. **1938**, 60, 309.
(31) Barrett, E. P.; Joyner, L. G.; Halenda, P. P. *J. Am. Chem. Soc*. **1951**, 73, 373.

(32) Zwierzak, A.; Kluba, M. *Tetrahedron* **1971**, 27, 3163.
(33) Dong, Y.; He, K.; Yin, L.; Zhang, A. *Nanotechnology* **2007**, 18, 435602.
(34) Taylor, C. M.; Watson, S. P.; Bryngelson, P. A.; Maroney, M. J. *Inorg. Chem*. **2003**, 42, 312.
(35) International Center for Diffraction Data "PDF-2", 2006; Card #27-1120.
(36) Given the inherent difficulty in determining gas adsorption surface areas for materials supported on Ni foam, electrochemically active surface areas were measured by the double layer capacitance method (See Appendix). Although this method involves certain assumptions that have raised questions regarding its applicability, it has been applied in studies of this kind, where electrode materials of a similar type are involved.
(37) Bard, A. J.; Faulkner, L. R. *Electrochemical Methods: Fundamentals and Applications*; Wiley; Ney York, 2001; pp 103.
(38) (a) Weil, M.; Puchberger, M.; Günne, J. A.; Weber, J. *Chem. Mater*. **2007**, 19, 5067. (b) Silva, M. A. P.; Franco, D. F.; Brandão, A. R.; Barud, H.; Dias Filho, F. A.; Ribeiro, S. J. L.; Messaddeq, Y.; de Oliveira, L. F. C. *Mater. Chem. Phys*. **2010**, 124, 547.
(39) (a) Vuurman, M. A.; Stufken, D. J.; Oskam, A.; Deo, G.; Wachs, I. E. *J. Chem. Soc. Faraday Trans*. **1996**, 92, 3259. (b) Boix, A.; Miró, E. E.; Lombardo, E. A.; Bañares, M. A.; Mariscal, R.; Fierro, J. L. G. *J. Catal*. **2003**, 217, 186. (c) Yang, J.; Liu, H.; Martens, W. N.; Frost, R. L. *J. Phys. Chem. C* **2010**, 114, 111. (d) Gupta, R. K.; Sinha, A. K.; Raja Sekhar, B. N.; Sricastava, A. K.; Singh, G.; Deb, S. K. *Appl. Phys. A* **2011**, 103, 13.
(40) Ho, S.-W.; Houalla, M.; Hercules, D. M. *J. Phys. Chem.* **1990**, 94, 6396.
(41) *Handbook of X-ray Photoelectron Spectra: A Reference Book of Standard Spectra for Identification*; Bomben, K. D., Moulder, J. F., Sobol, P. E., Stickel, W. F . Eds.; Perkin Elmer: Eden Prairie, 1992.
(42) Deltombe, E., Pourbaix, M., *Atlas of Electrochemical Equilibria in Aqueous Solutions*; Pourbaix, M., Ed.; National Association of Corrosion: Houston, TX, 1974; pp 504-515.
(43) The TOF for CoPi was reported in reference 12d. It should be noted that the TOF for CoPi was determined based on the assumption that all Co in the sample is participating in catalysis, and thus represents an absolute lower limit. The value for Co_3O_4 was measured by the methods described above, and an example calculation is given in the Appendix.

Chapter 3. Appendix

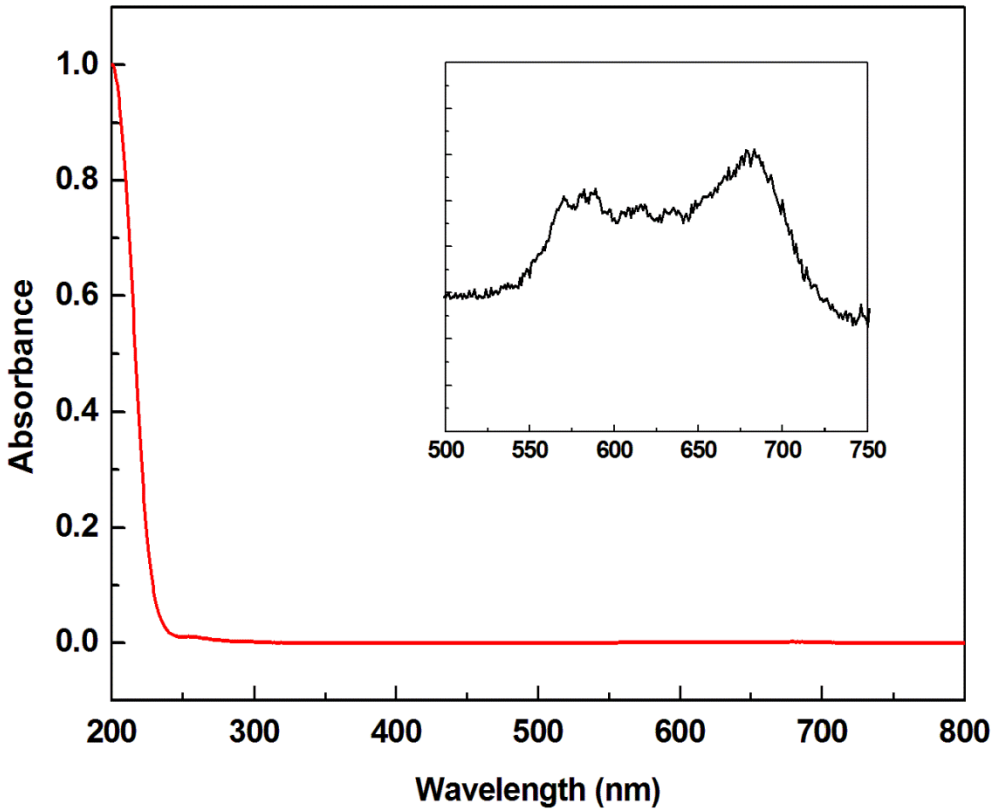

Figure A1. UV-vis spectrum of **1** in acetonitrile. The d-d transition region (inset) shows characteristic bands for Co^{II} in a pseudo-tetrahedral geometry,[A1] as observed in the known X-ray crystal structure.

Double-layer capacitance measurements for electrode roughness factor (R_f) determination

The electrode surface roughness factor (R_f), which corresponds to the electrochemically active surface area per physical electrode area, was determined by double-layer capacitance charging at a low-potential region where no redox activity is present. Observed current densities at various scan rates are plotted in Figure A2. The double-layer capacitance of the electrode was determined according to the following relationship.

$$C_{dl} = \frac{d_i}{d(\frac{\partial E}{\partial t})} \qquad (1)$$

Here, C_{dl} is the double-layer capacitance expressed as the slope of the current vs. the scan rate. Literature values for the capacitance of a smooth Ni surface and oxide-like surfaces (20 μF and 60 μF, respectively) were used in the calculations.[A2-A5] From multiple sets of experiments, average R_f values obtained for cobalt metaphosphate catalyst electrode and Ni foam were 25 and 30 respectively. (Units are cm^2 of electrochemically active surface area per cm^2 of physical surface area.) Similar experiments conducted on Co_3O_4 anode and amorphous cobalt phosphate electrodes yielded R_f values of 28 and 30, respectively. These values are much lower than those obtained through similar methods in pH 14 solutions (> 100) and the difference is attributed to much slower diffusion of the phosphate charge carrier compared to hydroxide (augmented by an overall buffer strength of 0.1 M vs. 1 M), thus leading to the inefficient use of the internal porous volume of the Ni foam.

Double layer capacitance measurements were also conducted on catalysts on glassy carbon (data displayed in Figure A3). The capacitance for the blank glassy carbon electrode was determined to be 41.38 $\mu F/cm^2$, and R_f values for $Co(PO_3)_2$, Co_3O_4, and CoPi were 1.25, 1.49, and 2.27, respectively. These similar R_f values indicate similar electrochemically active surface areas.

Turnover frequencies (TOFs) calculated from the number of surface sites obtained by the double-layer capacitance measurements range from 1.4 – 2.5 s^{-1}, which constitute the upper limit. In actual experiments the surface area utilized is probably larger.

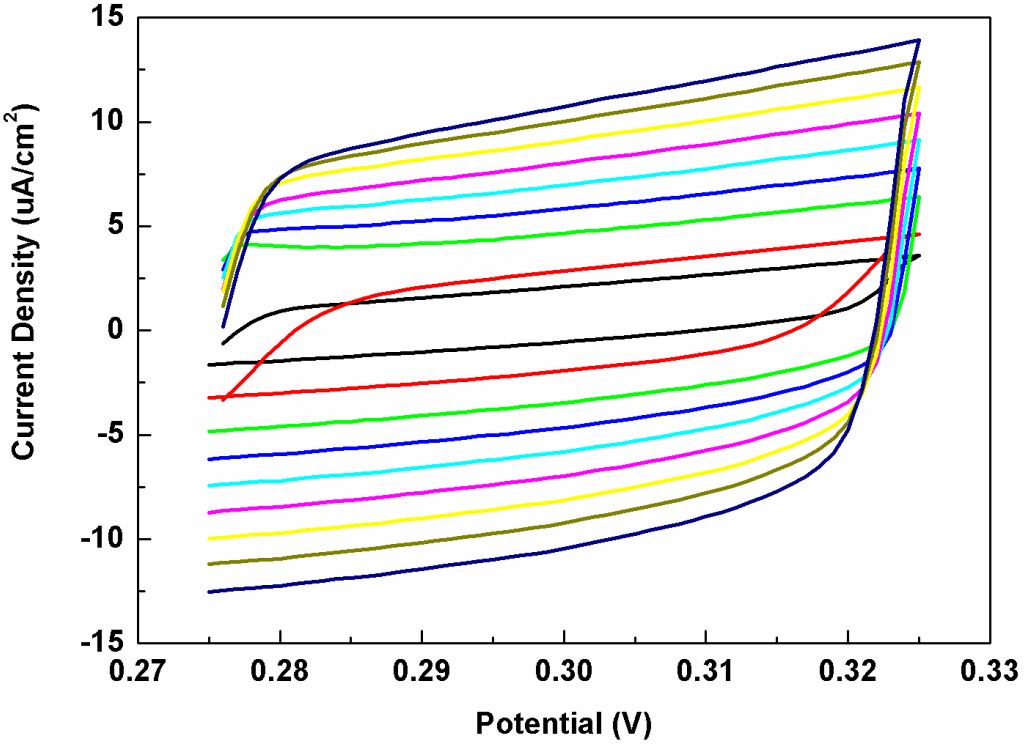

Figure A2. Cyclic voltammograms of the catalyst electrode in the low potential region at various scan rates (1-9 mV/s).

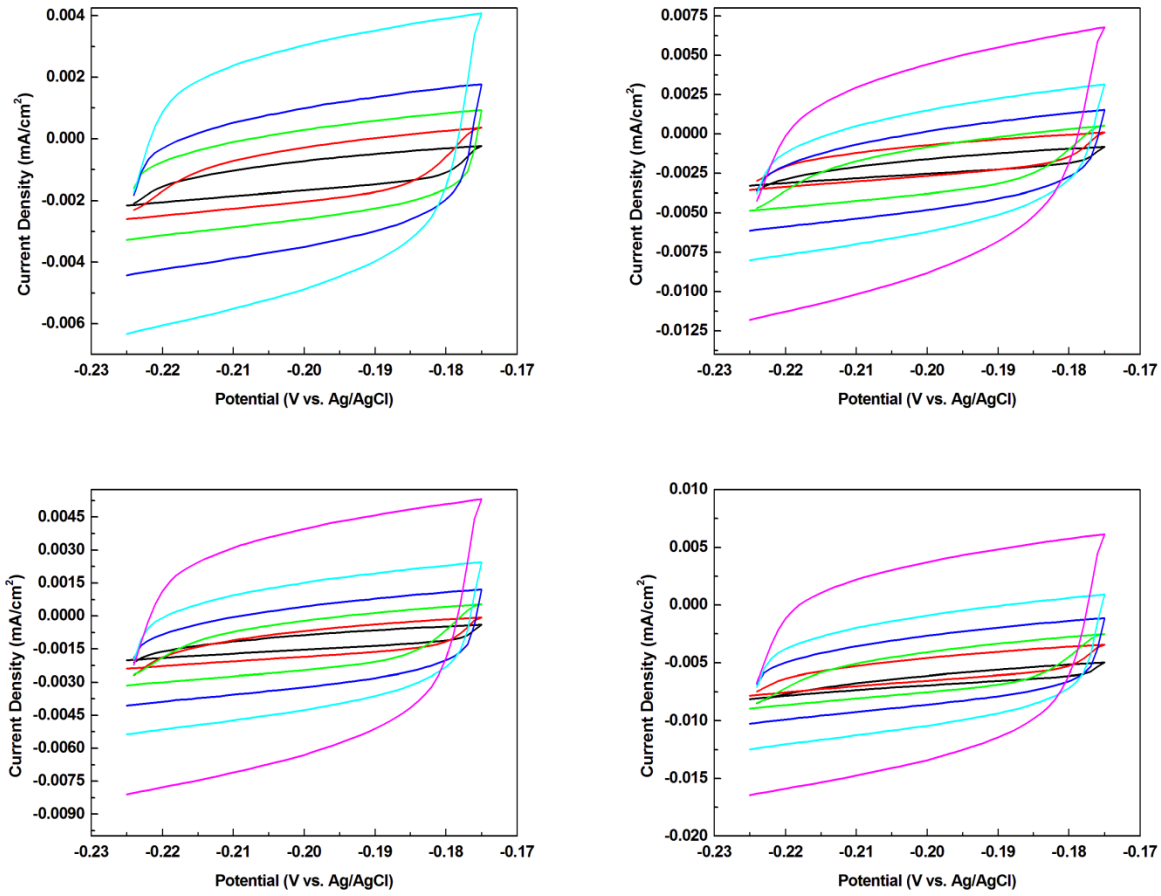

Figure A3. Cyclic voltammograms of the catalyst electrodes in the low potential region at various scan rates (5-100 mV/s). Data for glassy carbon (top left), $Co(PO_3)_2$ (top right), Co_3O_4 (bottom left), and CoPi (bottom right) are displayed.

Surface-site density and turnover frequency (TOF) calculations

In order to calculate the TOFs at various overpotentials, the number of active surface metal sites needs to be estimated. (TOF = [turnover number per unit time]/[# of active sites], where the turnover number is determined by the current density. Current densities (mA = mC/s) were converted to the number of electrons passed, and subsequently to the number of molecules of oxygen by division of four. The number of active surface sites was estimated the gas adsorption surface area. A Brunauer-Emmett-Teller (BET)[A6] surface area of 19.9 m^2/g was recorded, and from the known crystal structure,[A7,A8] the number of surface sites per unit area was determined ($3/nm^2$, as viewed down the [110] plane). Dividing the total surface area of the catalyst loading by the surface-site density, the total number of surface-sites can be obtained. Subsequently, the TOF can be obtained by dividing the TON per second by the total number of surface-sites. An example calculation is as follows:

For 1 mg of sample and current density of 8.01 mA/cm^2,

$$0.00801\,\frac{\mathrm{C}}{\mathrm{s}} \times \left[6.2415 \times 10^{18}\ \frac{\mathrm{e^-}}{\mathrm{C}}\right] \times \frac{\text{Turnover}}{4\ \mathrm{e^-}} = [1.25 \times 10^{16}]\ \text{Turnover/s}$$

$$0.001\ \mathrm{g} \times 19.9\ \frac{\mathrm{m^2}}{\mathrm{g}} \times \frac{(1 \times 10^{18})\ \mathrm{nm^2}}{1\ \mathrm{m^2}} \times \frac{3\ \text{Active Surface Sites}}{\mathrm{nm^2}} = [5.97 \times 10^{16}]\ \text{Active Surface Sites}$$

$$\frac{[1.25 \times 10^{16}]\ \text{Turnover/s}}{[5.97 \times 10^{16}]\ \text{Active Surface Sites}} = 0.209\ \frac{\text{Turnovers}}{\text{metal} \cdot \mathrm{s}}$$

Similar calculations carried out for the Co_3O_4 sample (20 nm, 25 m^2/g area) yielded a TOF of 0.0113 s^{-1}.[A9]

Alternatively, since surface rearrangement to oxide-type structure occurs during catalysis, the crystal structure of Co_3O_4 can also be used to calculate TOF. The number of surface exposed metal sites in this case is 6.1 per nm^2 (instead of 3 for $Co(PO_3)_2$),[A9] establishing a TOF of 0.103 $metal^{-1} \cdot s^{-1}$.

A complete utilization of the gas adsorption surface area occurs only at relatively low catalyst loadings on the electrode surfaces. This is evident in the plot of catalyst loading vs. current

density, in which at high loadings (> 0.6 mg/cm^2 for a flat glassy carbon electrode, Figure A4), saturation behavior occurs. A catalyst loading of 1 mg/cm^2 for Ni foam electrodes was chosen because it is a low loading level for this type of porous electrode, and has been shown to prevent exposure of significant amounts of bare Ni surface area.[A9]

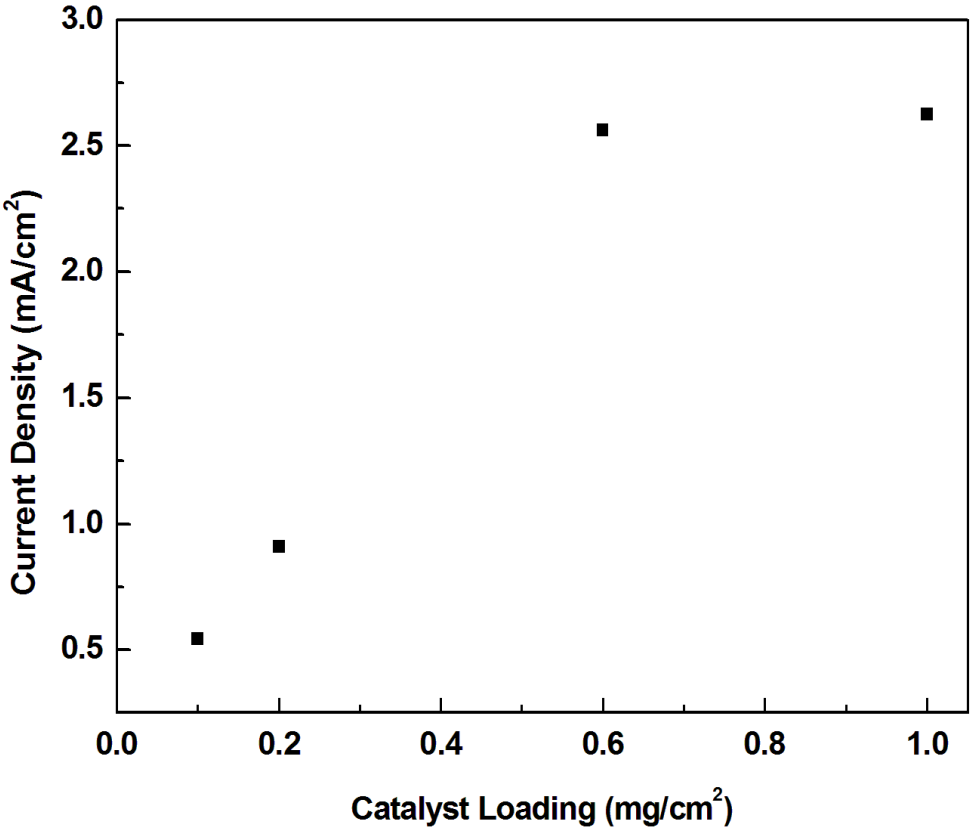

Figure A4. Current density (at 1.1 V vs. Ag/AgCl) plotted as a function of catalyst loading on a flat glassy carbon electrode. Saturation behavior is observed at high loadings (>0.6 mg/cm^2).

Measurement of Faradaic efficiency

Faradaic efficiency measurements were conducted in a gas-tight H-cell, with the headspace being monitored with an Ocean Optics Fospor-R O_2 probe. Headspace pressure was monitored by an Omega Engineering dial pressure gauge. Total volume of the H-cell with all ports closed was 137.5 mL, and the solution volume used was 90 mL. Background leak tests were performed multiple times, showing that less than 0.1 μmol O_2 leaked into the flask in the first half hour. Some leaking (up to 0.3 μmol) was observed when the system was left standing over two hours. All experiments were conducted for 40 mins, thus leaking in of O_2 was negligible. The buffer solutions used were degassed by bubbling N_2 through them for more than one hour. The presence of dissolved O_2 was accounted for by calculating the standard solubility in water at the experimental temperature and pressure.

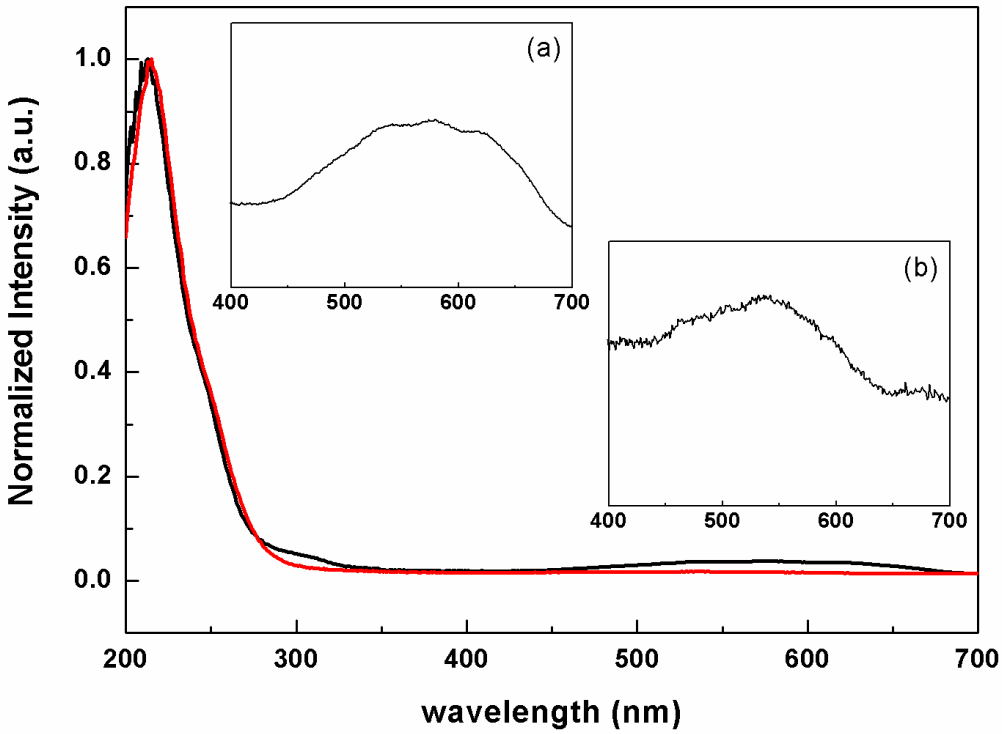

Figure A5. UV-Vis spectrum of $Co(PO_3)_2$. Inset shows the d-d transition region of the material before (a) and after (b) hydration. Characteristic peaks for tetrahedral Co^{II} and octahedral Co^{II} can be seen respectively.[A1]

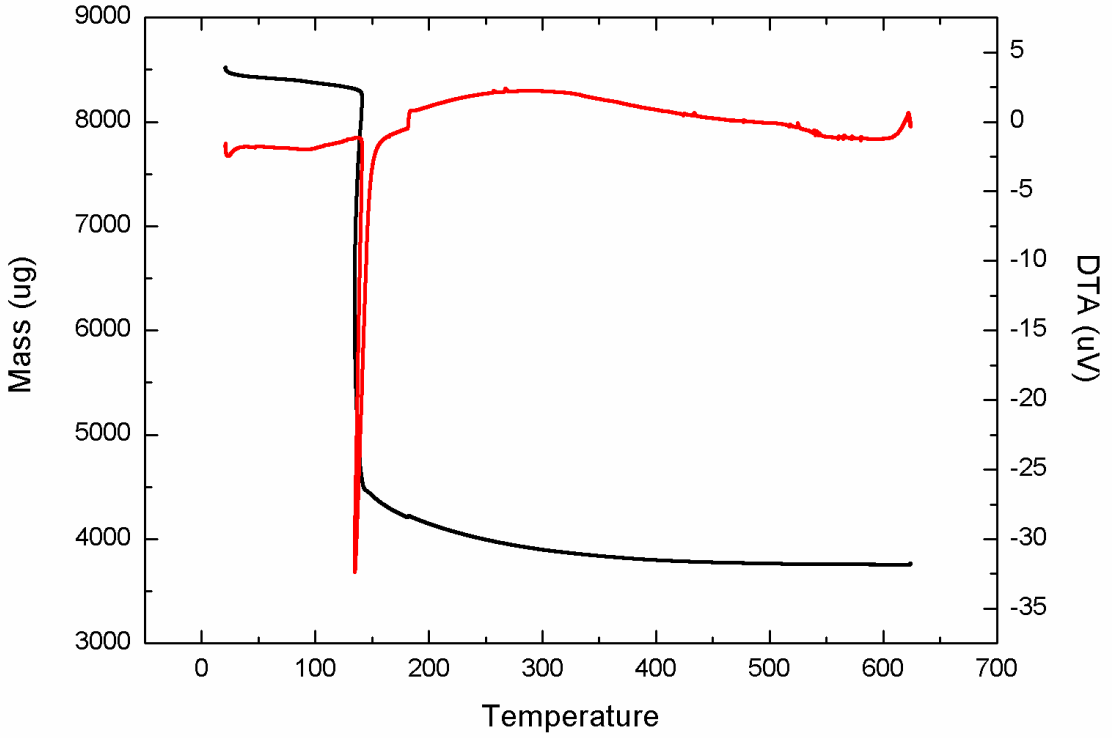

Figure A6. TGA (black) and DSC (red) traces of the transition from precursor **1** to $Co(PO_3)_2$. Sharp mass loss is observed at 138 ℃. Give ceramic yield (at a temp) and calculated yield for $Co(PO_3)_2$.

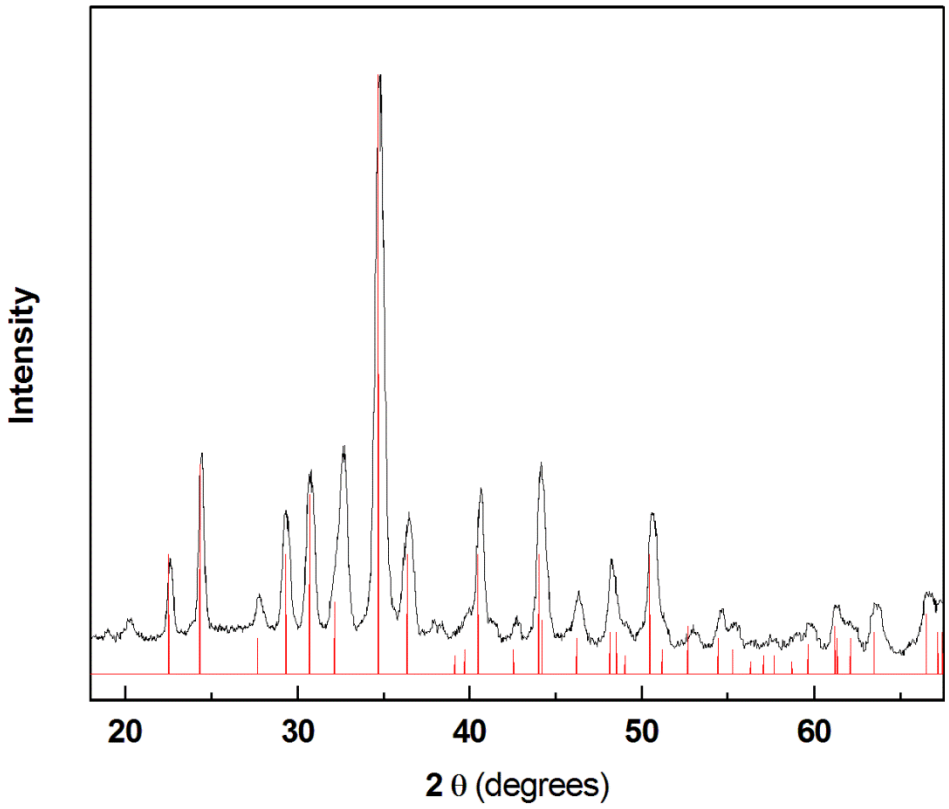

Figure A7. Powder X-ray diffraction pattern for $Co(PO_3)_2$ nanoparticles (black) and simulated pattern (red).

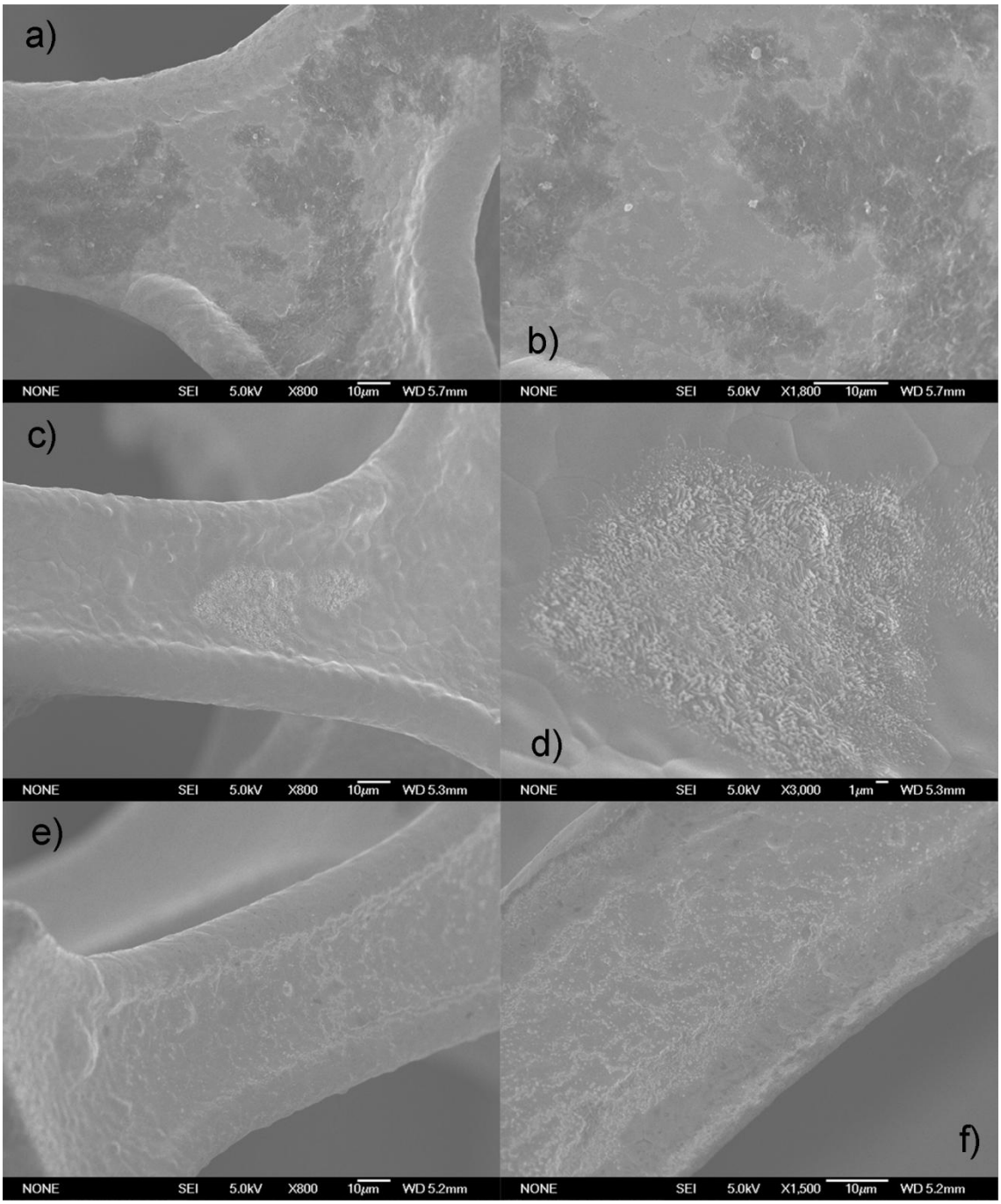

Figure A8. Scanning electron microscopy images of Ni foam deposited $Co(PO_3)_2$ before catalysis (a, b), after catalysis (c, d), and Co_3O_4 (e, f). All samples exhibit similar surface coverage on Ni foam. SEM images of CoPi on Ni foam can be found in reference A12.

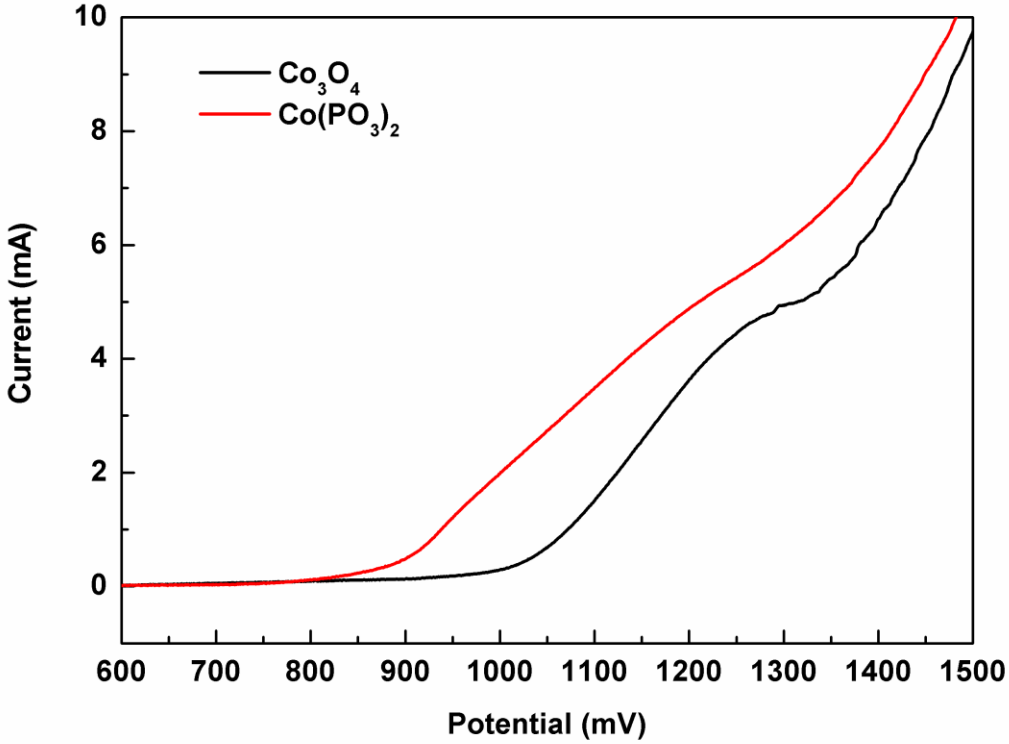

Figure A9. Linear sweep voltammogram of $Co(PO_3)_2$ and Co_3O_4 at a scan rate of 1 mV/s. The precatalytic oxidation of $Co(PO_3)_2$ can be resolved from water oxidation catalysis.

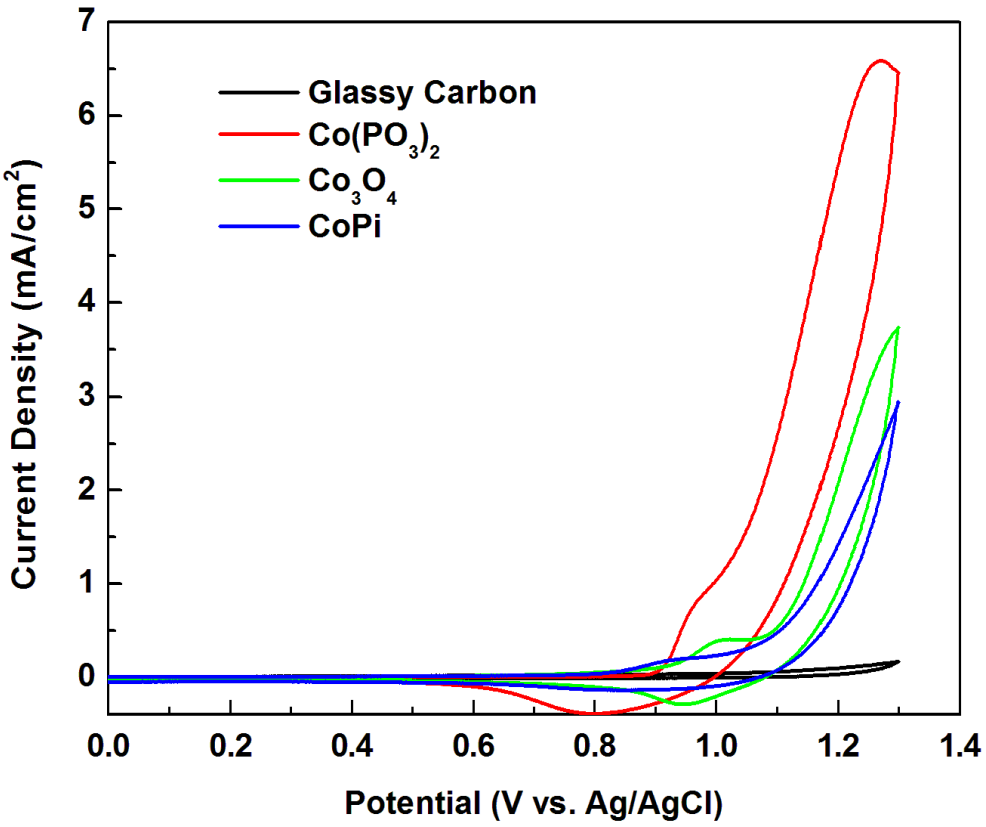

Figure A10. Cyclic voltammogram of $Co(PO_3)_2$, Co_3O_4, and CoPi on glassy carbon at a scan rate of 100 mV/s.

Determination of Catalytic Onset Overpotential

The catalytic onset overpotentials for all catalytic systems were determined by extrapolating the linear catalysis region of the LSV curves from glassy carbon electrode data (fit lines shown in Figure A9) and finding the intercept with the exchange current. The formula for the exchange current plot derived from the data points in the low potential region (0.4 to 0.7 V vs. Ag/AgCl) was $i = 0.0043\ V - 0.0021$, where i is in mA and V is in Volts. The formula of the catalysis plot for $Co(PO_3)_2$ was $i = 6.0242\ V - 5.8615$. Finding the intercept of these two plots yielded an onset potential of 0.973 V vs. Ag/AgCl, which at pH 6.4 is 313 mV overpotential. Similar analyses for Co_3O_4 and CoPi yielded onset overpotentials of 414 mV and 434 mV, respectively.

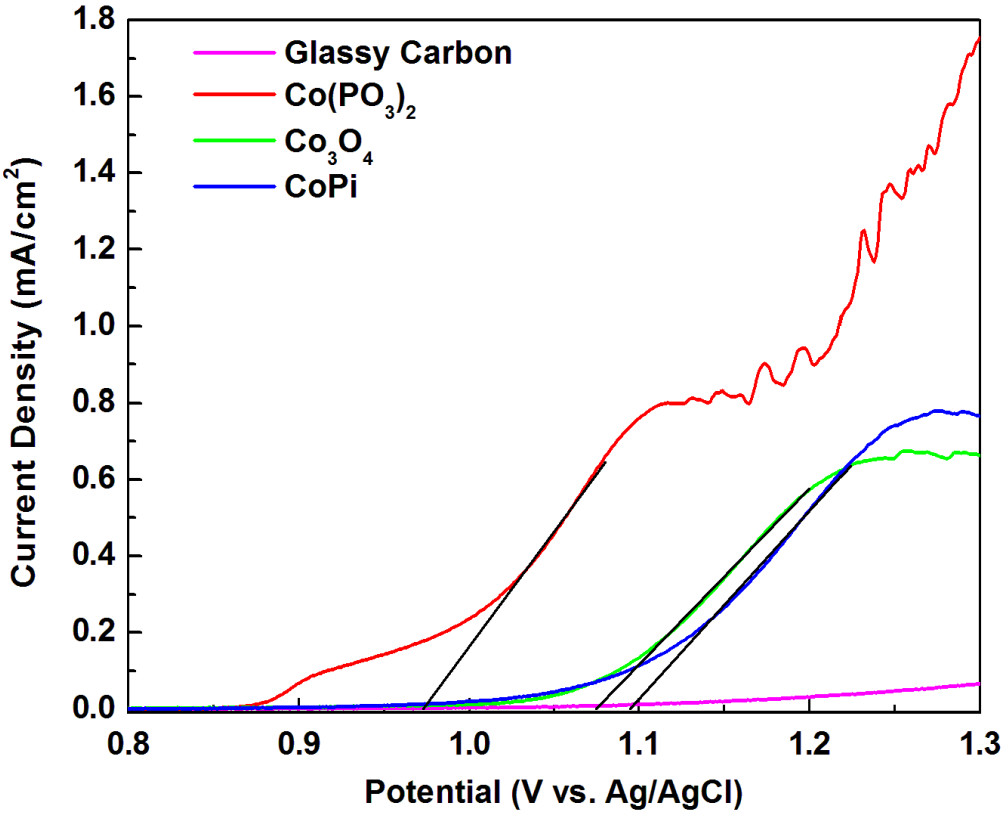

Figure A11. Linear sweep voltammogram of $Co(PO_3)_2$, Co_3O_4, and CoPi on glassy carbon at a scan rate of 1 mV/s, with catalytic Tafel plot fitted onto linear catalysis region.

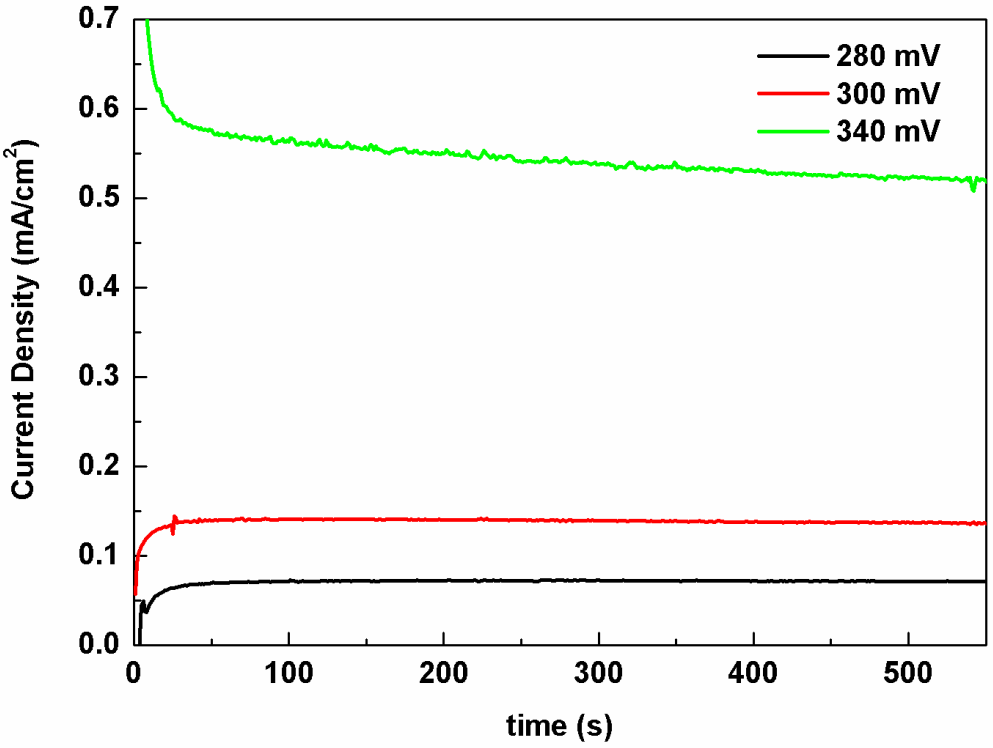

Figure A12 Constant potential electrolysis curves at low overpotentials (η < 400 mV) are shown. Current densities observed at such overpotentials are 72.3, 140.2, and 541 μA, respectively.

Table A1. Steady-state current densities at various overpotentials for blank Ni foam and the catalyst electrodes. Background currents at near thermodynamic potential (η = 100 mV) were 42 $\mu A/cm^2$ and 19 $\mu A/cm^2$ for Ni and $Co(PO_3)_2$, respectively.

η (mV)	Ni Foam	$Co(PO_3)_2$	Co_3O_4	$CoPi^{A10}$
240	49.1	28.1	30.4	44.0
250	49.1	33.4	30.4	43.7
270	49.5	46.2	30.2	52.9
280	51.6	72.3	34.8	66.2
300	54.3	140	40.3	89.1
340	52.1	541	164	177
390	65.4	2590	645	657
440	91.7	7134	1328	1448

All current density values expressed in $\mu A/cm^2$

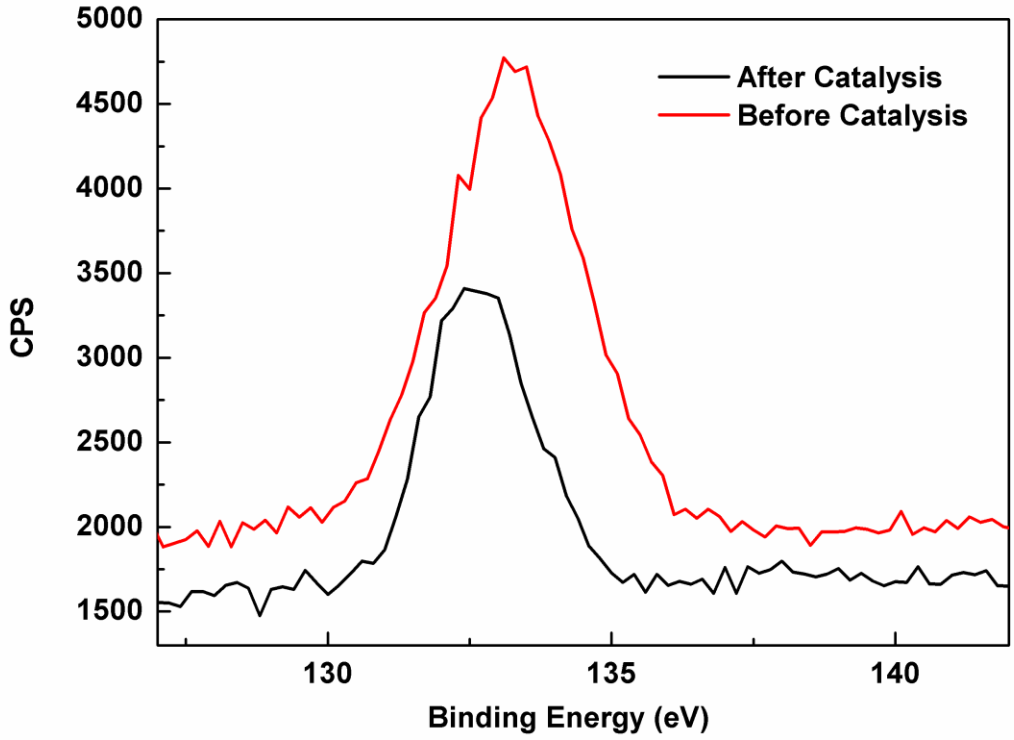

Figure A13. Phosphorous region of the XPS before and after catalysis. A slight shift in the peak at ca. 133 eV is attributed to partial conversion of the metaphosphate to phosphate during restructuring of the surface-sites.[A11]

Table A2. Atomic distribution of Co, P, and O in pre-catalytic and post-catalytic samples, obtained by integration of XPS peaks (2p for Co and P, 1s for O).

Element	Pre-catalytic sample	Post-catalytic sample
Co	10.26	27.28
P	19.75	6.403
O	69.98	66.31

All values expressed as a percentage.

References

(A1) Taylor, C. M.; Watson, S. P.; Bryngelson, P. A.; Maroney, M. J. *Inorg. Chem*. **2003**, 42, 312.
(A2) Levin, S.; Smith, A. L. *Discuss. Faraday Soc*. **1971**, 52, 290.
(A3) Marsan, B.; Fradette, N.; Beaudoin, G. *J. Electrochem. Soc*. **1992**, 139 (7), 1889.
(A4) Koninck, M. D.; Poirier, S.; Marsan, B. *J. Electrochem. Soc*. **2006**, 153 (11), A2103
(A5) Karimi Sherverdani, R.; Lasia, A. *J. Appl. Electrochem*. **1999**, 29, 979.
(A6) Brunauer, S.; Emmett, P. H.; Teller, E. *J. Am. Chem. Soc*. **1938**, 60, 309.
(A7) Averbuch-Pouchot, P. M. T.; Bagieu-Beucher, D. M. *Acta Cryst.* **1983**, C39, 25.
(A8) Rothammel, W.; Burzlaff, H. *Acta Cryst.* **1989**, C45, 551.
(A9) Esswein, A. J.; McMurdo, M. J.; Ross, P. N.; Bell, A. T.; Tilley, T. D. *J. Phys. Chem. C* **2009**, 113, 15068.
(A10) Kanan, M. W.; Nocera, D. G. *Science* **2008,** 321, 1072.
(A11) *Handbook of X-ray Photoelectron Spectra: A Reference Book of Standard Spectra for Identification*, (Eds: K. D. Bomben, J. F. Moulder, P. E. Sobol, W. F. Stickel), Perkin Elmer, Eden Prairie, U.S.A, **1992**.
(A12) Esswein, A. J.; Surendranath, Y. S.; Reece, S. Y.; Nocera, D. G. *Energy Environ. Sci.* **2011**, 4, 499.

Chapter 4. Molecular Cobalt Electrocatalyst for Proton Reduction at Low Overpotential

Introduction

Solar driven water splitting for chemical energy storage is an area of active research, given the potential application of such technology for solving current energy problems.[1,2] Water splitting couples the oxidation of water with the reduction of protons to form hydrogen fuel. Platinum is an excellent catalyst for the hydrogen evolution reaction (HER); however, due to its scarcity, great effort is being directed toward finding cheaper and more earth abundant alternatives. Many first-row metal catalysts have been developed, including hydrogenase mimics[3-5] and other types of complexes.[6-10] One of the challenges for HER catalyst design is achieving a good catalytic rate at a modest overpotential. Thus, many of the synthetic catalysts exhibit rapid rates, but only at potentials much higher than the thermodynamic potential for acid reduction.[3-7,9] Herein we report two trimetallic cobalt complexes, one of which exhibits an onset for HER at overpotentials as low as 25 mV. Appreciable catalytic rates are achieved at $\eta > 75$ mV, and experimental evidence suggests that the catalysis occurs homogeneously.

Results and Discussion

The tricobalt complex $[Co_3(C_5H_9O_2)_6][BF_4]_2$ (**1**) was synthesized by reaction of $Co[N(SiMe_3)_2]_2$ with 3 equivalents of 3-hydroxy-3-methyl-2-butanone ($HOCMe_2COMe$), accompanied by an *in situ* oxidation of cobalt with an equivalent of $AgBF_4$ as shown in Scheme 1. Red crystals of **1** were isolated in 85 % yield by cooling the reaction solution to -80 ˚C.

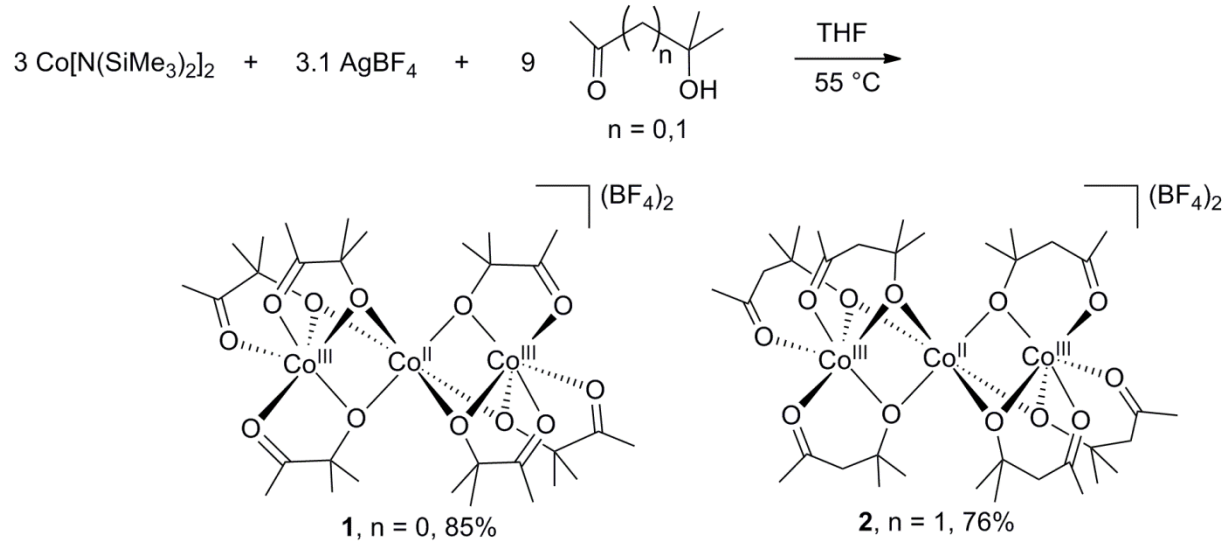

Scheme 1. Synthesis of compounds **1** and **2**

The structure of **1** (Figure 1) may be described as containing two pseudo-octahedral, tris(chelate) Co^{III} complexes that serve as tridentate ligands for a central Co^{II} ion. Both

$Co^{III}[OCMe_2COMe]_3$ moieties are complexed to Co^{II} by sharing of an octahedral face comprised of three alkoxy oxygen atoms. Note that several related trinuclear $2Co^{III}/Co^{II}$ complexes have been reported.[11,12]

The analogous complex $[Co_3(C_6H_{11}O_2)_6][BF_4]_2$ (**2**) was synthesized similarly, using 4-hydroxy-4-methyl-2-pentanone ($HOCMe_2CH_2COMe$) as the ligand precursor. X-ray quality crystals of this complex were not obtained, but it is believed to have a structure analogous to that of **1**, on the basis of combustion analysis and spectroscopic evidence (NMR and IR). For example, paramagnetically shifted resonances for the methyl groups of **2**, at 66.73 and -95.41 ppm, are similar to the corresponding resonances of **1** at 70.70 and -97.14 ppm. A peak unique to **2** at -7.04 ppm is assigned to the methylene protons (see Figure A1). Infrared spectra of **1** and **2** also exhibit similar features, most notably symmetric and asymmetric C-O stretches for the bridging alkoxy groups (1054, 875 cm^{-1} for **2** and 1042, 885 cm^{-1} for **1**), consistent with literature values for such bridging alkoxides in transition metal complexes.[13,14] The ν(C=O) stretches for **1** and **2** both appear at 1658 cm^{-1}. Also, the UV-vis spectra of **1** and **2** exhibit similar broad charge transfer bands (340 nm for **1** and 380 nm for **2**; Figure S11) which give them a red color.

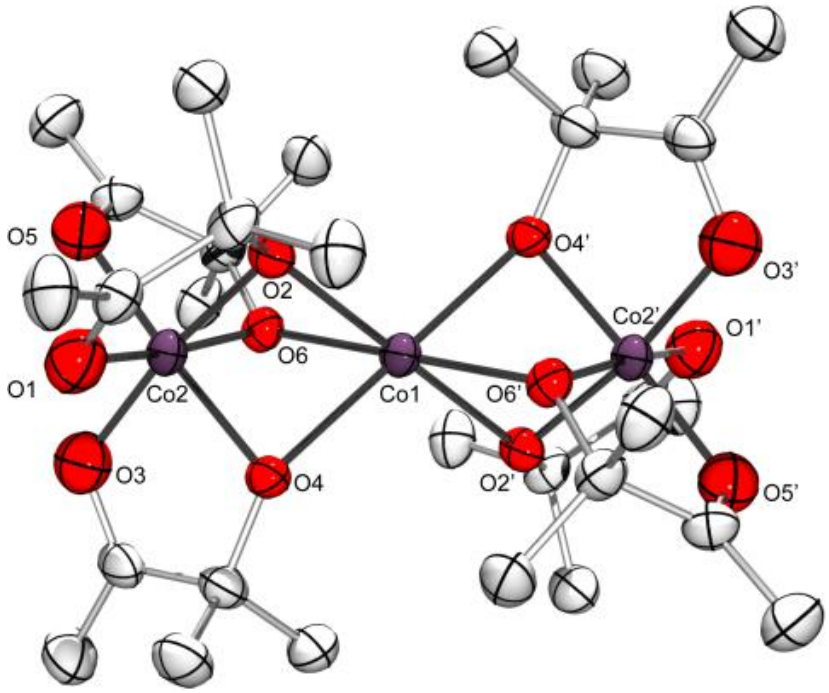

Figure 1. Structure of **1** determined by single-crystal X-ray diffraction. The thermal ellipsoids are shown at the 50 % probability level. Hydrogen atoms and THF molecules are omitted for clarity.

The redox behavior of **1** and **2** is unexceptional in the absence of acid. Compound **2** displays only one, quasireversible redox event at ca. 0.37 V vs. $Fc^{+/0}$ in acetonitrile (Figure A2 inset; all potentials are referenced to $Fc^{+/0}$), which is assigned to the $Co^{III/II}$ couple for the central cobalt ion. The $Co^{III/II}$ couple of **2** is similar to the oxidation potential of Ag^+ measured in a less polar solvent (0.41 V in THF),[15] which explains why the central Co^{II} is not oxidized by $AgBF_4$.

Compound **1** displayed no noticeable redox events (in scan rate ranges of 1 mV/s to 100 mV/s) before reaching potentials too oxidizing or reducing to induce decomposition. Presumably, the corresponding $Co^{III/II}$ couple for **1** is not readily discernible because it coincides with the oxidative decomposition occurring at ca. 0.65 V.

In the presence of tosic acid, cathodic current enhancements are observed in the cyclic voltammograms (CVs) of **2** in acetonitrile (0.4 mM) with 0.1 M $[N^nBu_4]PF_6$ as a supporting electrolyte (Figure 2). A linear growth in the catalytic current is observed with incremental increases in the acid concentration (Figure A12).

Noticeably, the CV of **2** displays an onset for the catalytic current very near the reported thermodynamic potential (E°) of tosic acid reduction at -0.65 V in acetonitrile.[16] Faradaic efficiency measurements were conducted by comparing the headspace H_2 concentration measured by GC to the charge passed in constant potential electrolysis experiments (see the Appendix and Figures A3, A4 for details). Faradaic efficiencies of 84%, 83%, and 86% were recorded for electrolyses performed at overpotentials (η; η = E - E°) of 25 mV, 75 mV, and 125 mV, respectively. Faradaic efficiencies of greater than 93% were recorded for electrolyses at η ≥ 150 mV. Electrolyses were performed such that more than 10 Coulombs passed before the GC analyses.

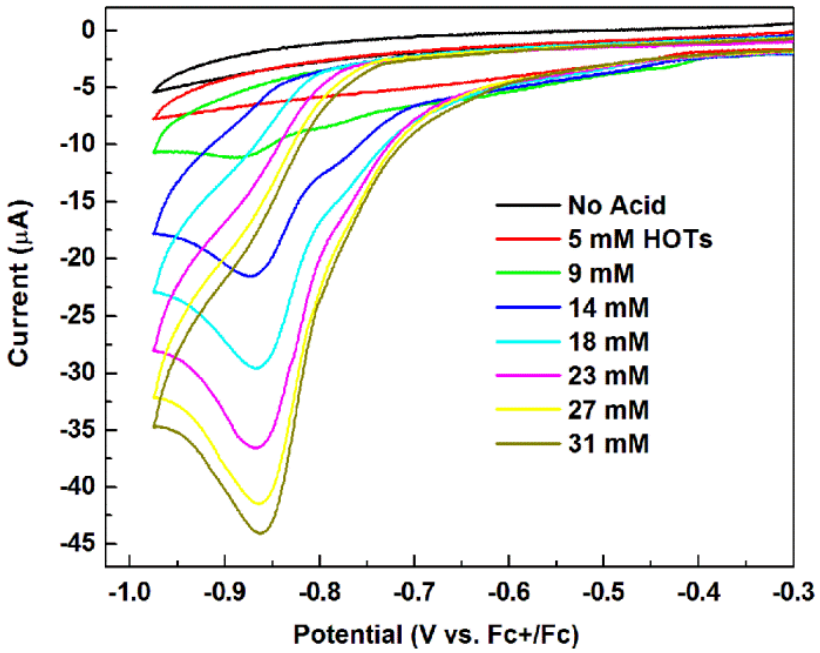

Figure 2. Cyclic voltammogram of **2** in the presence of tosic acid. A linear growth in the current with added amounts of acid was observed, and the onset overpotential for the reduction of tosic acid is close to the thermodynamic value.

Turnover frequencies (TOFs) for the catalyst were estimated by using equation 1 derived

by Kubiak and coworkers for homogeneous electrocatalytic systems assuming an EC' mechanism (See the Appendix for detailed calculations).[17]

$$\mathrm{TOF} = \frac{1}{D_c}\left(\frac{j_{lim}}{\mathrm{nF[C]}}\right)^2 \quad (1)$$

The diffusion coefficient for compound **2** was measured electrochemically to be 6.0 x 10^{-6} $cm^2 \cdot s^{-1}$ (see the Appendix). From equation 1, the calculated TOF of **2** at η = 150 mV was ca. 80 s^{-1}. This estimated TOF is comparable to other cobalt catalysts found in the literature;[8,9] however, the catalytic onset of ca. η = 25 mV is among the lowest reported and is close to that of a platinum electrode.[10,16] Notably, Gray and Winkler have recently reported Co(triphos) compounds (triphos = 1,1,1-tris(diphenylphosphenomethyl)ethane) that reduce protons at overpotentials as low as 15 mV.[10] Various control experiments indicated that complex **2** is required for the electrocatalysis. Thus, no detectable amounts of H_2 were produced at η = 150 mV from 25 mM tosic acid acetonitrile solutions containing $HOCMe_2CH_2COMe$, $Co(NO_3)_2$, or $Co(OTs)_2$. Compound **1** was subjected to identical reaction conditions and was shown to be active for proton reduction catalysis, but at high overpotentials (η > 200 mV; see the Appendix and Figure A6).

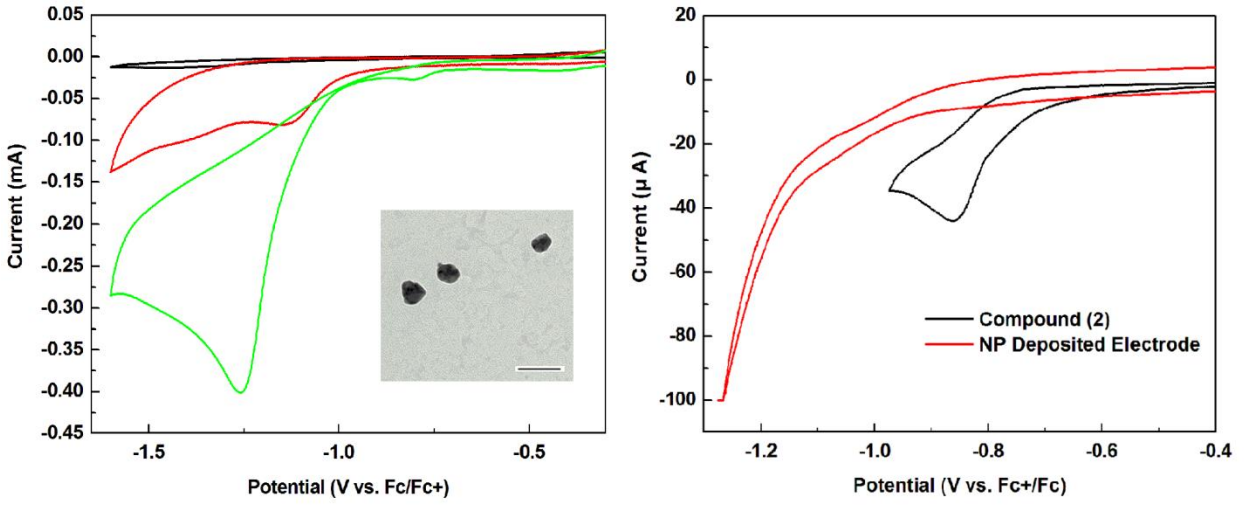

Figure 3. Cyclic voltammogram of **2** in the presence of tosic acid at potentials more negative than its stability limit (left). Large current enhancement was observed due to electroplating of cobalt nanoparticles (shown in inset; scale bar 100 nm). The acid concentrations are 0 mM, 5 mM, and 9 mM for black, red, and green traces, respectively. CV of compound **2** in catalysis conditions and that of a glassy carbon electrode with pre-deposited NPs (right).

Recently, Savéant and coworkers reported that the active species for a family of molecular chlathrochelate cobalt catalysts for proton reduction were in fact cobalt-containing nanoparticles generated on the electrode surface.[18] Thus, several experiments were conducted to investigate the possible conversion of **2** to nanostructured or insoluble materials, and to

determine the homogeneity of the catalysis. A rinse test was performed, whereby the glassy carbon electrode used for catalysis was removed from the reaction solution, rinsed gently with acetonitrile, and then placed in a fresh solution with supporting electrolyte and tosic acid. A voltammogram obtained after this procedure was identical to that obtained with a new glassy carbon electrode in the same solution. Additional experiments designed to identify any nanoparticles that form during catalysis utilized transmission electron microscopy (TEM). Catalysis was performed using a TEM grid as an electrode, which was subsequently analyzed by TEM. No visible particle formation occurred after application of potentials less reducing than -0.99 V. Catalyst decomposition was forced by driving the potential beyond the stability limit of the catalyst (< -1.0 V), in which case a large current was observed along with deposition of particles on the TEM grid (Figure 3).

Nanoparticles of cobalt on glassy carbon electrodes were deliberately prepared by applying -1.4 V to a clean glassy carbon electrode in a solution of **2** with 20 mM tosic acid. The electrode was then rinsed with acetonitrile and placed into a 20 mM tosic acid solution in the absence of **2**, and the nanoparticles on the electrode yielded the voltammogram displayed in Figure 3. The deposited particles were not responsible for proton reduction catalysis at low overpotentials, suggested by the absence of a current response at potentials less than -1.0 V, and well within the range in which compound **2** exhibited catalysis.

A further test of the homogeneity of electrocatalysis involved a Koutecky-Levich analysis using a rotating disk electrode. A Koutecky-Levich plot of **2** at η = 125 mV is displayed in Figure A8 and the voltammograms at various rotating rates are plotted in Figure A7. The observed deviation from linearity in the Levich plot for **2** is characteristic of homogeneous catalysis, because the diffusion limited current is reached at low rotation rates (600 rpm).[19] Electrode-bound catalysts typically exhibit linear behavior to rotation rates higher than 1000 rpm.[19] Thus, the tests described above strongly suggest that the proton reduction catalysis by **2** occurs homogeneously.

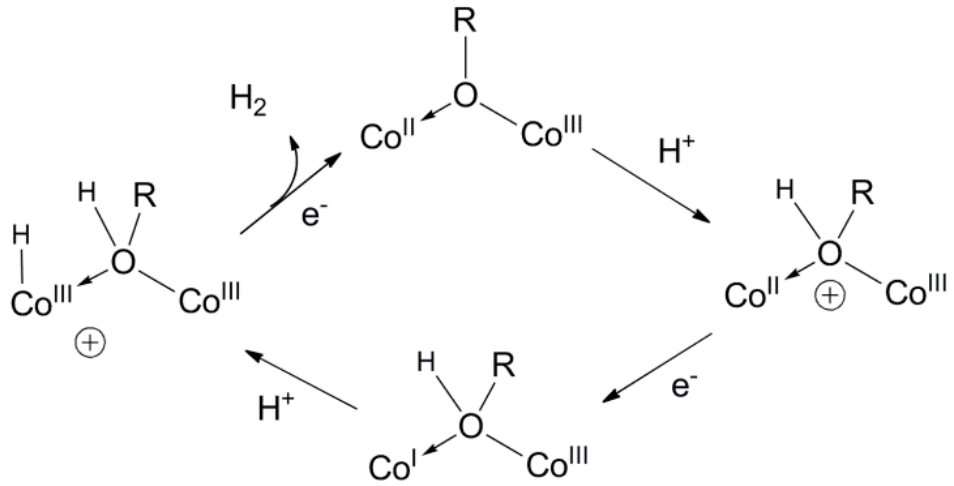

Figure 4. Proposed mechanism for the proton reduction catalysis of **2**.

In the presence of one equivalent of tosic acid, compound **2** displays a reduction event at ca. -0.7 V, observed electrochemically by differential pulse voltammetry (DPV; Figure A9). Since this reduction is not observed in the absence of acid, it is attributed to a protonated form of **2**. In the presence of additional acid, a catalytic reduction wave grows at -0.7 V, indicating that this catalysis is intiated by the protonation of **2**. Thus, a possible catalytic cycle consistent with this observation is displayed in Figure 4. In this scenario, protonation of **2** precedes reduction of the central cobalt to Co^{I}. This reduced cobalt center is then protonated to produce a Co^{III} hyride, which would then undergo a coupling reaction with a nearby, oxygen-bound proton to form H_2. The formation of a Co^{III} hydride from Co^{I} has frequently been proposed in the literature, and a Co^{III} hydride has been spectroscopically observed in proton reduction.[10]

The results described above provide an intriguing structural type for consideration in the design and synthesis of new electrocatalysts for proton reduction. Importantly, the structures of **1** and **2** are relatively simple, and involve a central Co^{II} cation sandwiched by neutral, tridentate ligands. Notably, a wide variety of analogous structures should be readily generated by addition of neutral, tridentate donors to a source of the Co^{II} cation. In an initial effort to pursue this theme, the known, dicationic bis[tri(pyrazolyl)methane] complex of cobalt was synthesized as reported in the literature.[20] This complex, $[Co(tpm)_2][BF_4]_2$ (tpm = tri(pyrazolyl)methane), is a catalyst for tosic acid reduction in acetonitrile (1-4 mM) and exhibits electrochemical behavior similar to that of **1**, while displaying catalysis at $\eta > 150$ mV (Figure S10). Note, however, that this complex is fundamentally different from **1** and **2**, in that the nitrogen donors of the tpm ligands lack available lone pairs for binding protons, and this may explain the higher onset potential for catalysis. The $[Co(tpm)_2][BF_4]_2$ complex also exhibits limited stability with tosic acid concentrations higher than 10 mM. It is presumed that the Co^{III} in compound **2** increases the basicity of the bridging alkoxy oxygen, enabling the facile binding of protons and the subsequent coupling to the neighboring hydride.

Conclusions

In summary, the trimetallic cobalt complex **2** functions as an efficient catalyst for the proton reduction reaction, operating at a low onset overpotential of 25 mV. Related trimetallic complexes should be of interest as electrocatalysts. For example, Chaudhuri and coworkers have reported the synthesis of valence-trapped compounds similar in structure to **1** and **2**, using bicyclic octahedral Cr^{III} metalloligands that incorporate various central metal cations, including Mn^{II}, Co^{II} and Ni^{II}.[21]

Experimental

General. All manipulations were conducted under an inert nitrogen atmosphere using standard Schlenk techniques or a Vacuum Atmospheres drybox, unless otherwise stated. Chemicals were purchased from Aldrich and used as received. Dry, oxygen free solvents were used throughout. The compound $Co[N(SiMe_3)_2]_2$[22] was synthesized as reported in the literature. Carbon, hydrogen, and nitrogen elemental analyses were performed at the College of Chemistry microanalysis laboratory at the University of California, Berkeley. FTIR spectra were obtained on a Thermo Nicolet 6700 FTIR spectrometer. The UV-Vis spectra were acquired using a Varian Cary 300 series spectrometer. Transmission electron microscopy (TEM) was carried out on a Philips Tecnai 12 transmission electron microscope operating at 200 kV. Inductively coupled plasma optical emission spectroscopy (ICP-OES) for cobalt ion detection in post catalytic solutions was performed on a Perkin-Elmer ICP-OES Optima 7000 DV. Standard solutions were purchased from Perkin-Elmer and used as received. Electrochemical data were recorded on a Bioanalytical Systems model EC epsilon computer-controlled potentiostat. Unless otherwise stated, all measurements were conducted in a 25 mL glass cell with a three-electrode configuration. Electrochemistry experiments were performed in HPLC grade acetonitrile solutions with 0.1 M $[N^nBu_4]PF_6$. The reference electrode used was 0.1 M $Ag/Ag(NO)_3$ in acetonitrile and the reference was calibrated relative to ferrocene/ferrocenium in order to correct for any potential drifts for every data collection. Solution resistance in CV and LSV experiments was corrected for by the iR compensation algorithm, using software in the EC epsilon potentiostat. Polished platinum wire was used as an auxiliary electrode, and glassy carbon working electrode with a 3 mm diameter was utilized. Rotating disk electrode experiments were performed using the Bioanalytical Systems model RDE-2 unit. Faradaic efficiencies were determined by observing H_2 production by Agilent GC using a gas separation column. An aliquot of headspace gas (100 μL) was extracted with a gas-tight syringe after the electrolysis experiment and injected into a GC sample port manually. Solution ^1H NMR and ^{19}F NMR spectra were recorded at 400 MHz using a Bruker AVQ-400 spectrometer. Chemical shifts for ^1H NMR spectra were referenced internally to the residual solvent proton signal relative to tetramethylsilane. Chemical shifts for ^{19}F NMR spectra were referenced internally to the residual solvent proton signal relative to trichloro-fluoro-methane. X-ray diffraction data were collected using a Bruker AXS three-circle diffractometer coupled to a CCD detector with graphite-monochromated Mo Kα radiation (λ = 0.71073 Å). The structures were solved by direct methods using SHELXS and refined against F^2 on all data by full-matrix least squares with SHELXL-97. All non-hydrogen atoms were refined anisotropically; hydrogen atoms were included into the model at their geometrically calculated positions and refined using a riding model. Experimental details of the crystal structure for compound **(1)** are given in Table A1-A5.

Synthesis of $[Co_3(C_5H_9O_2)_6][BF_4]_2$ (1). In a typical synthesis, $Co[N(SiMe_3)_2]_2$ (380 mg, 1 mmol) was dissolved in THF (ca. 30 mL). A THF (20 mL) solution of $AgBF_4$ (136 mg, 0.7 mmol) was

then added. After stirring the mixture at room temperature for 10 min, 307 mg (3 mmol) of 3-hydroxy-3-methyl-2-butanone ($HOCMe_2COMe$) was added dropwise. The reaction mixture was then heated to 55 °C for 8 h. A slow color change to red was observed. The solution was filtered and the solvent was removed under vacuum and the resulting solid was washed with hexanes three times (30 mL each wash) and ether three times (30 mL each wash). The product was obtained in 85% yield by recrystallization in THF by cooling to -78 °C under N_2. The identical compound was obtained in similar yields when ferrocenium tetrafluoroborate was employed as the oxidant. Anal. Calcd: C, 37.65; H, 5.69; Co, 18.47. Found: C, 37.21; H, 5.70; Co, 18.00. ^{1}H NMR (400.13 MHz, CD_3CN): δ = 70.70 (s), 14.27 (s, THF), 12.91 (s, THF), -97.14 (s). ^{19}F NMR (376.49 MHz, CD_3CN): δ = -147.9 (s). IR (KBr, cm^{-1}) 3295 (m), 2979 (m), 2932 (m), 1658 (s), 1463 (m), 1437 (m), 1380 (s), 1356 (m), 1286 (w), 1170 (s), 1042 (s), 963 (bs), 885 (m), 842 (m), 764 (s).

Synthesis of $[Co_3(C_6H_{11}O_2)_6][BF_4]_2$ (2). Synthetic procedures were identical to those used for **1**, with 4-hydroxy-4-methyl-2-pentanone ($HOCMe_2CH_2COMe$) as the source of the ligand. The solvent was removed under vacuum and the resulting solid was washed with hexanes three times (30 mL each wash) and ether three times (30 mL each wash). Analytically pure product was obtained in 76% yield. Anal. Calcd: C, 41.52; H, 6.39; Co, 16.98. Found: C, 41.90; H, 6.72; Co, 17.01. ^{1}H NMR (400.13 MHz, CD_3CN): δ = 66.73 (s), 36.01 (s, THF), 13.12 (s, THF), -7.04 (s), -95.41 (s). ^{19}F NMR (376.49 MHz, CD_3CN): δ = -148.2 (s). IR (KBr, cm^{-1}) 3285 (w), 2969 (w), 1658 (s), 1594 (m), 1522 (w), 1466 (m), 1429 (m), 1374 (m), 1285 (w), 1247 (w), 1223 (w), 1054 (s), 1026 (s), 875 (s), 837 (s), 752 (s).

References

(1) Gray, H. B. *Nat. Chem.* **2009**, 1, 7.
(2) Turner, J. A. *Science*, **2004**, 305, 972
(3) Marr, A. C.; Spencer, D. J. E.; Schroder, M. *Coord. Chem. Rev.*, **2001**, 219, 1055.
(4) Gloaguen, F.; Rauchfuss, T. B. *Chem. Soc. Rev.*, **2009**, 38, 100.
(5) Wang, M.; Chen, L.; Sun, L. *Energy Environ. Sci.*, **2012**, 5, 6763.
(6) Dubois, M. R.; Dubois, D. L. *Acc. Chem. Res.*, **2009**, 42, 1974.
(7) Helm, M. L.; Stewart, M. P.; Bullock, R. M.; Dubois, M. R.; Dubois, D. L. *Science*, **2011**, 333, 863.
(8) Hu, X.; Brunschwig, B. S.; Peters, J. C. *J. Am. Chem. Soc.*, **2007**, 129, 8988.
(9) Dempsey, J. L.; Brunschwig, B. S.; Winkler, J. R.; Gray, H. B. *Acc. Chem. Res.*, **2009**, 42, 1995.
(10) Marinescu, S. C.; Winkler, J. R.; Gray, H. B. *Proc. Nat. Acad. Sci. USA*, **2012**, 109, 15127.
(11) Cotton, F. A.; Hugel, R.; Eiss, R. *Inorg. Chem*. **1968**, 7, 18.
(12) Bertrand, J. A.; Kelley, J. A.; Vassian, E. G. *J. Am. Chem. Soc*. **1969**, 91, 2394.
(13) Bradley, D. C., Mehrotra, R. C., Rothwell, I. P., Singh, A. *Alkoxo and Aryloxo Derivatives of Metals*, Academic Press, San Diego, 2001.
(14) Nakamoto, K. *Infrared and Raman Spectra of Inorganic and Coordination Compounds*, Wiley, Hoboken, 2009.
(15) Connelly, N. G.; Geiger, W. E. *Chem. Rev.*, **1996**, 96, 877.
(16) Felton, G. A. N.; Glass, R. S.; Lichtenberger, D. L.; Evans, D. H. *Inorg. Chem.*, **2006**, 45, 9181.
(17) Sathrum, A. J.; Kubiak, C. P. *J. Phys. Chem. Lett.*, **2011**, 2, 2372.
(18) Anxolabéhère-Mallart, E.; Costentin, C.; Fournier, M.; Nowak, S.; Robert, M.; Savéant, J.-M. *J. Am. Chem. Soc.*, **2012**, 134, 6104.
(19) Bard, A. J., Faulkner, L. R. *Electrochemical Methods: Fundamentals and Applications 2nd Ed.*, Wiley, New York, 2001.
(20) Sheets, J. R.; Schultz, F. A. *Polyhedron*, **2004**, 23, 1037.
(21) Burdinski, D.; Birkelbach, F.; Weyhermüller, T.; Flörke, U.; Haupt, H.-J.; Lengen, M.; Trautwein, A. X.; Bill, E.; Wieghardt, K.; Chaudhuri, P. *Inorg. Chem.*, **1998**, 37, 1009.
(22) Burger, H.; Wannagat, U. *Monatsh. Chem.* **1963**, 94, 1007.

Chapter 4. Appendix

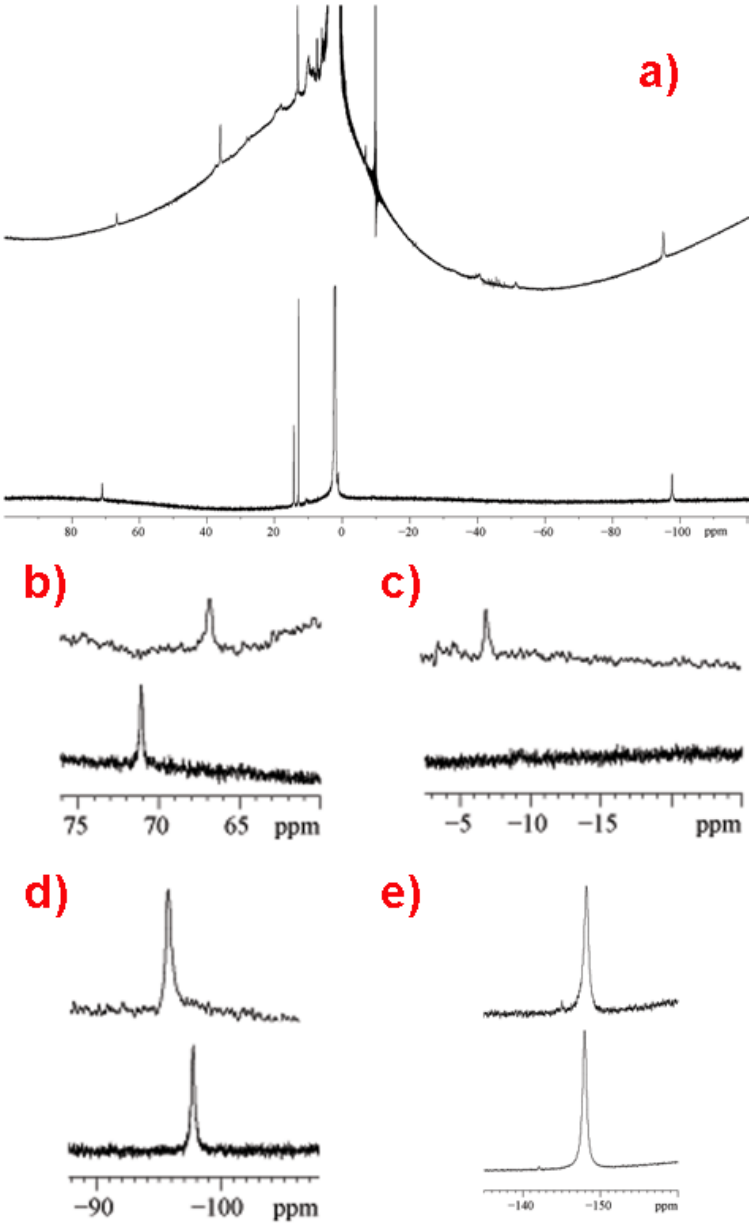

Figure A1. a) Paramagnetic ^{1}HNMR spectra of **1** (bottom) and **2** (top). Important sections of the spectra are highlighted in b), c), and d). Two of the methyl group protons on the ligand are displayed in b) and d), respectively, and the corresponding signals for **1** and **2** exhibit similar chemical shifts. Methylene protons unique to **2** appear at ca. -7.04 ppm, as shown in c). ^{19}FNMR spectra of **1** (bottom) and **2** (top) are displayed in e). Signals at ca. -148 ppm appear at a nearly identical chemical shift and are clearly distinct from that of $Co(BF_4)_2$, which appears at -134 ppm.

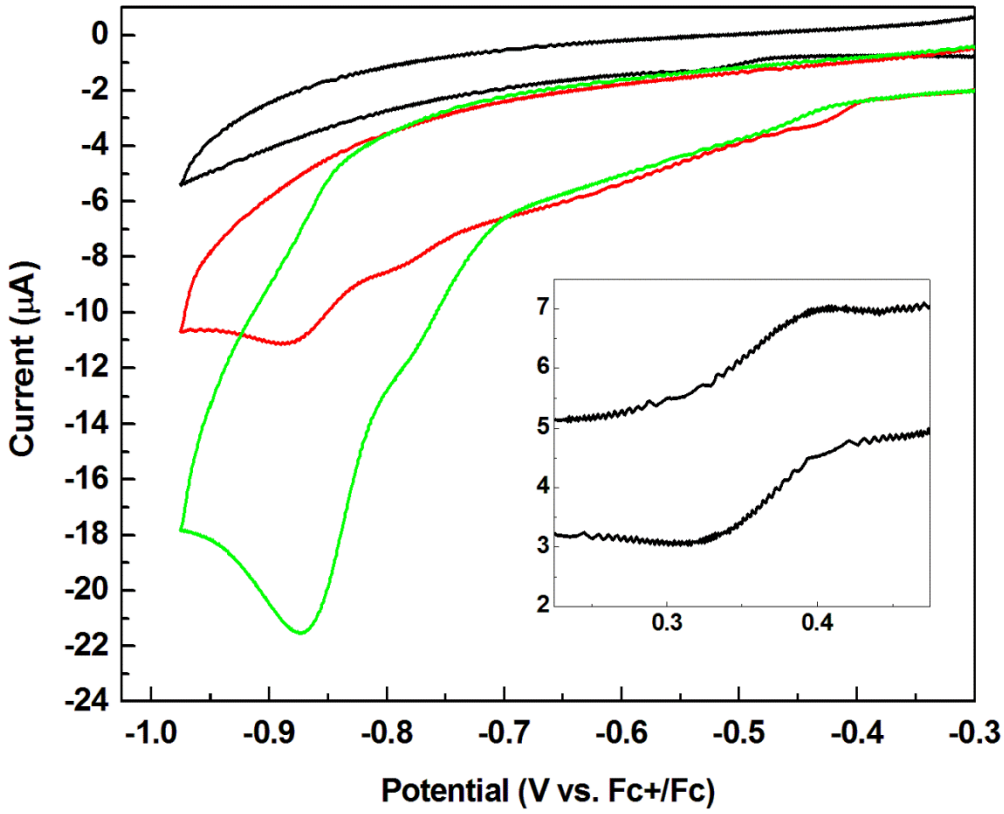

Figure A2. CV of **2** in the presence of HOTs (0 mM, 5 mM, and 9 mM). Shown in the inset is the reversible $Co^{III/II}$ couple.

Faradaic Efficiency Calculation

Faradaic efficiencies for the proton reduction catalyses by compound **2** were calculated simply by dividing the GC measured quantity of H_2 by the theoretical amount of H_2 based on the charge passed during electrolyses. The theoretical amount of H_2 was calculated by the following equation:

$$\text{Total charge passed during electrolysis [C]} \times \frac{6.241 \times 10^{18}\ \text{e}-}{1\ \text{C}} \times \frac{1\ \text{H}_2}{2\ \text{e}-} \times \frac{1\ \text{mol H}_2}{6.022 \times 10^{23}\ \text{H}_2} = \text{Theoretical H}_2\ \text{Yield [mol H}_2\text{]}$$

Generally, GC measurements were made after ca. 10 C had passed in an electrolysis experiment.

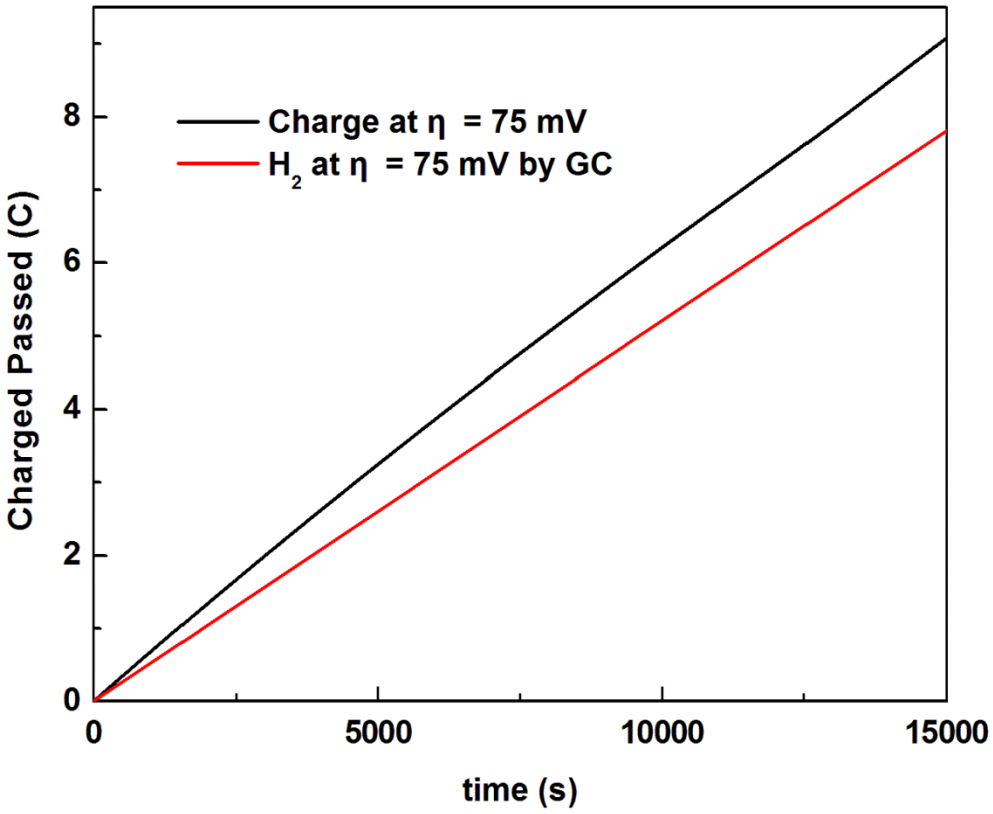

Figure A3. Charge passed (black trace) at an electrolysis experiment performed at η = 75 mV. The amount of H_2 observed by GC measurement was converted to the amount of charge required to produce the observed amount of H_2, and plotted in red. The Faradaic efficiency calculated for this electrolysis experiment is 83 %.

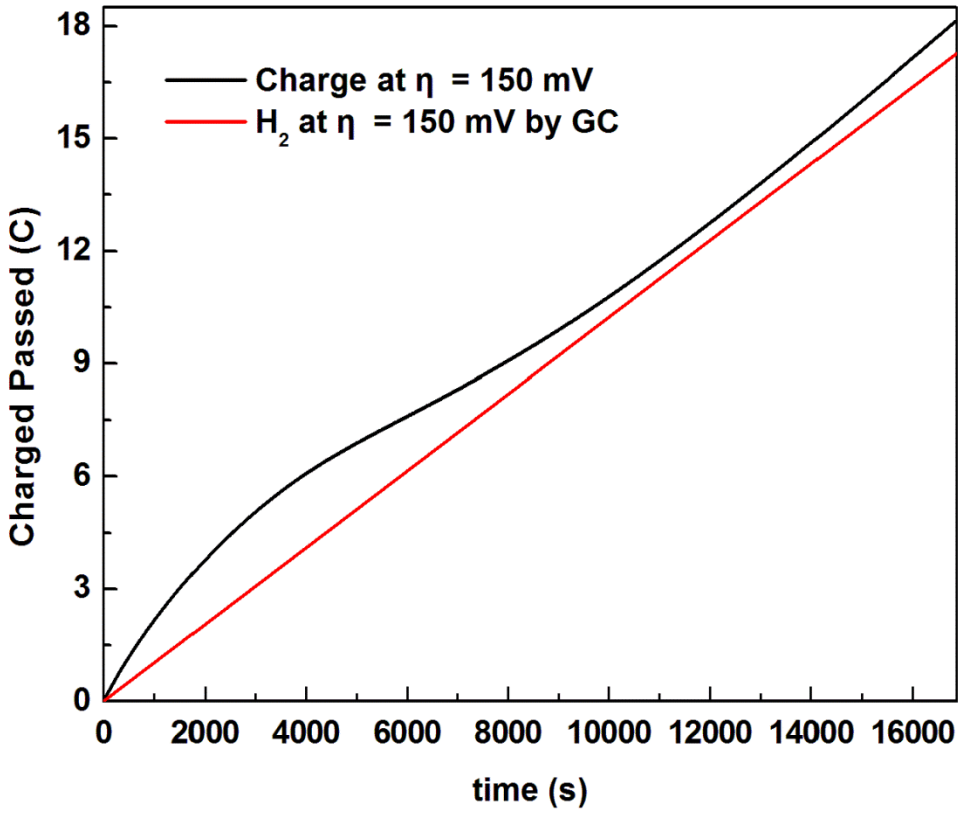

Figure A4. Charge passed (black trace) at an electrolysis experiment performed at η =125 mV. The amount of H_2 observed by GC measurement was converted to the amount of charge required to produce the observed amount of H_2, and plotted in red. The Faradaic efficiency calculated for this electrolysis experiment is 86 %.

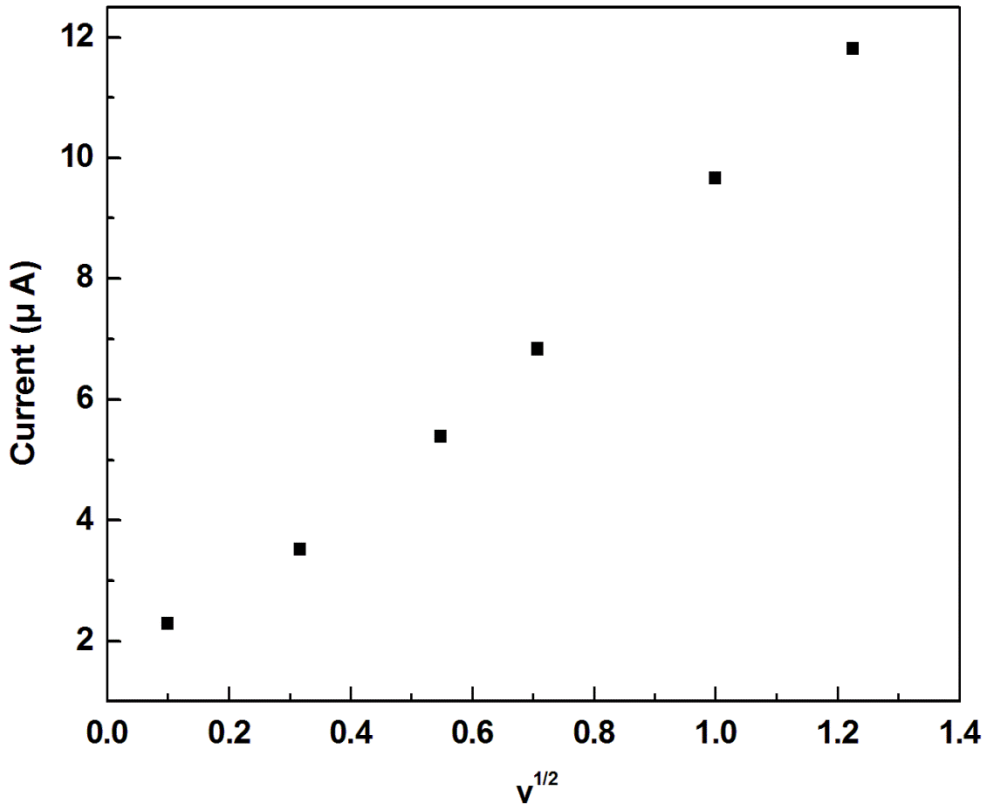

Figure A5. Anodic peak current for the $Co^{III/II}$ in compound **2** is plotted as a function of the squared root of the scan rate. The data was collected in order to estimate the diffusion coefficient for the complex (*vide infra*).

Diffusion Coefficient and TOF Estimation

The diffusion coefficient for compound **2** in the reaction solution was estimated electrochemically. The $Co^{III/II}$ couple was measured at varying scan rates (data in Figure A5), and the diffusion coefficient for compound **2** was deduced from the data according to the following relationship:

$$i_p = 0.4463 \left(\frac{F^3}{RT}\right)^{1/2} n^{3/2} A D^{1/2} C v^{1/2}$$

In the above equation, i_p is the peak current of the electrochemical event of interest (in this case, $Co^{II} \rightarrow Co^{III}$), F is Faraday's constant, n is the number of electrons involved in the electrochemical event of interest, A is the area of the electrode, C is the concentration of the analyte, D is the diffusion coefficient of the analyte, and v is the scan rate. For detailed derivation of the equation, refer to chapter 6 of reference A2.

The diffusion coefficient of **2** obtained from the data presented in Figure A5 by the mathematical relationship described above is ca. 6.0 x 10^{-6} cm^2 s^{-1}.

The TOF of proton reduction catalysis by **2** was calculated by the following expression derived by Kubiak and coworkers for a homogeneous catalytic system assuming an EC' mechanism.[A2]

$$\mathrm{TOF} = \frac{1}{D_c}\left(\frac{j_{lim}}{nF[C]}\right)^2$$

D_c is the diffusion coefficient of the catalyst (obtained in calculations above). j_{lim} is the limiting current density at diffusion limited potentials, and in our case a peak current at η = 150 mV was selected. An example calculation is as follows:

$$\mathrm{TOF} = \frac{1}{(6.0 \times 10^{-6})}\left(\frac{0.0017\ \mathrm{A/cm}}{2\ \mathrm{e} - \times\ 96485\ \mathrm{C/mol} \times (4 \times 10^{-7})\mathrm{mol/cm^3}}\right)^2 = 80.5\ \mathrm{s^{-1}}$$

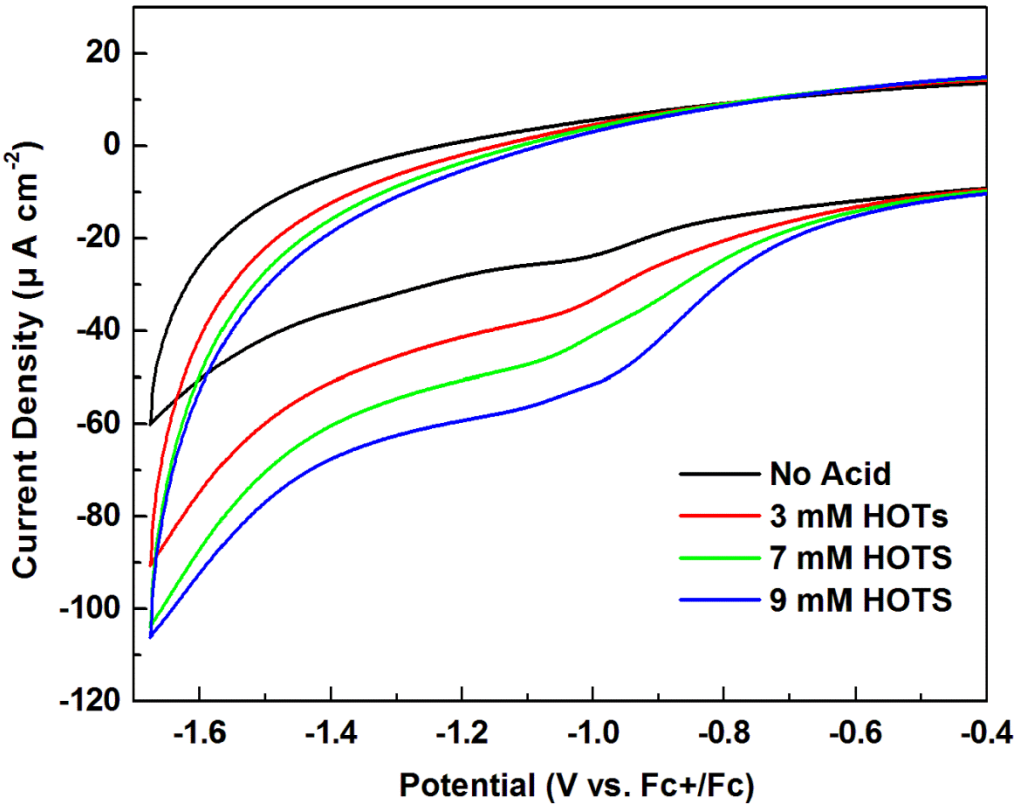

Figure A6. CV of **1** in the presence of HOTs. The catalytic onset for this compound was at a higher overpotential than that compared to **2**. H_2 was observed at $\eta > 200$ mV.

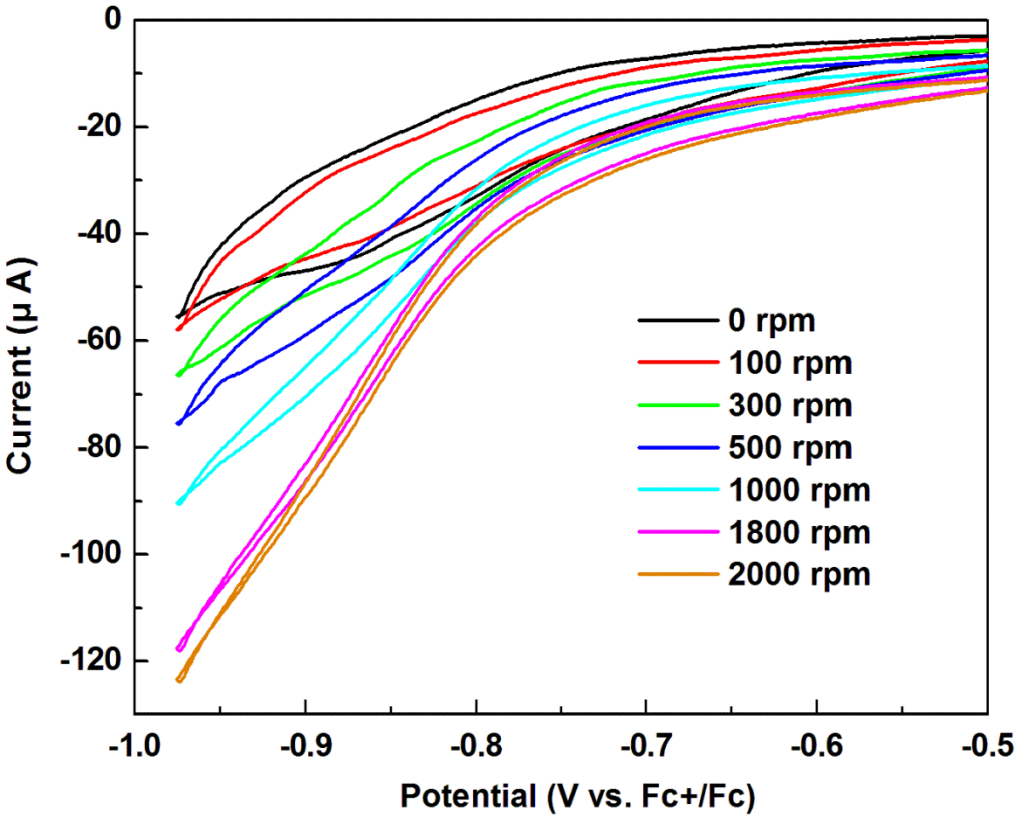

Figure A7. Proton reduction catalysis by compound **2** at various rotation rates of the rotating disk electrode (RDE). The RDE data was collected in order to construct the Koutecky-Levich plot displayed in Figure A8.

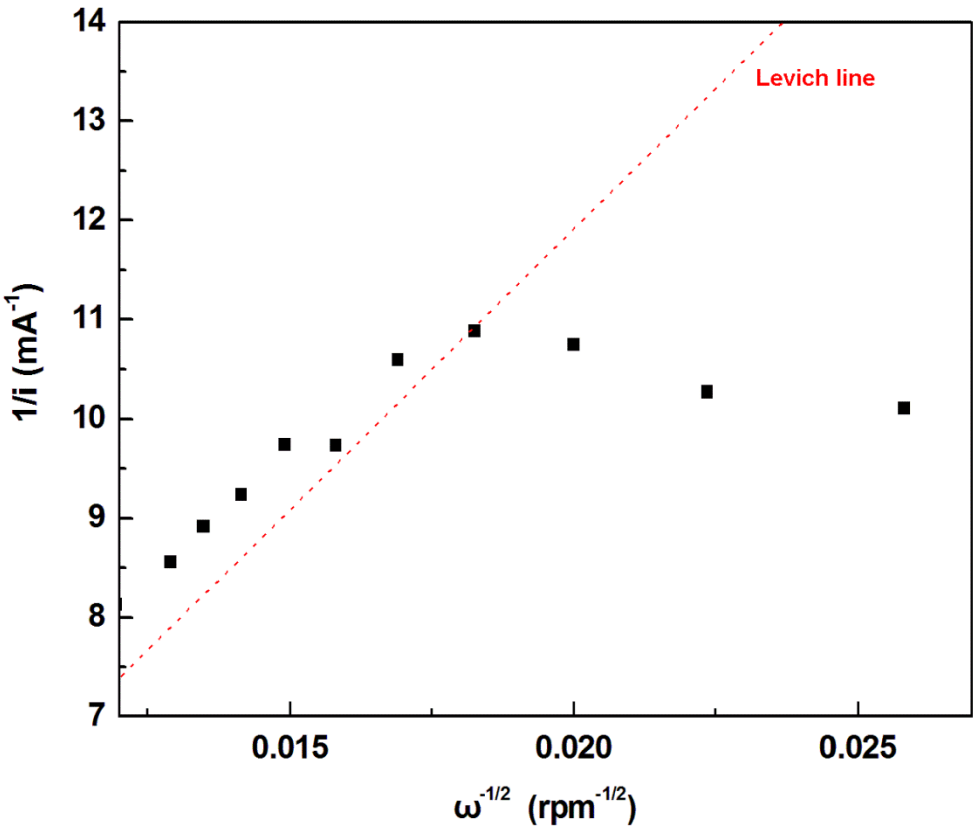

Figure A8. The Koutecky-Levich plot for the proton reduction catalysis of **2**. The deviation from the linear Levich line suggests that the concentration profile of the species responsible for the current changes as the diffusion layer thickness is varied due to the rotation rate. Such behavior is less likely to be observed for electrode-bound active species. For a detailed discussion, see reference A2.

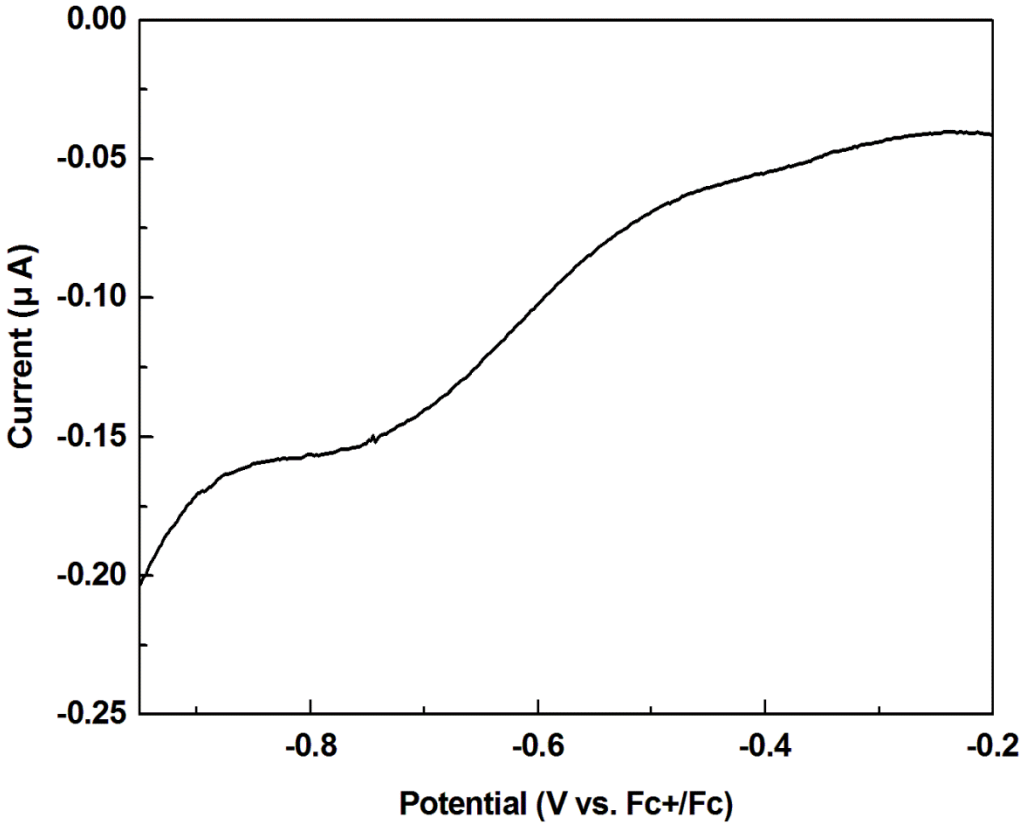

Figure A9. DPV trace of **2** with stoichiometric amount of acid. The reduction event for the protonated form of **2** can be seen at ca -710 mV, on top of which the catalytic current grow upon addition of acid.

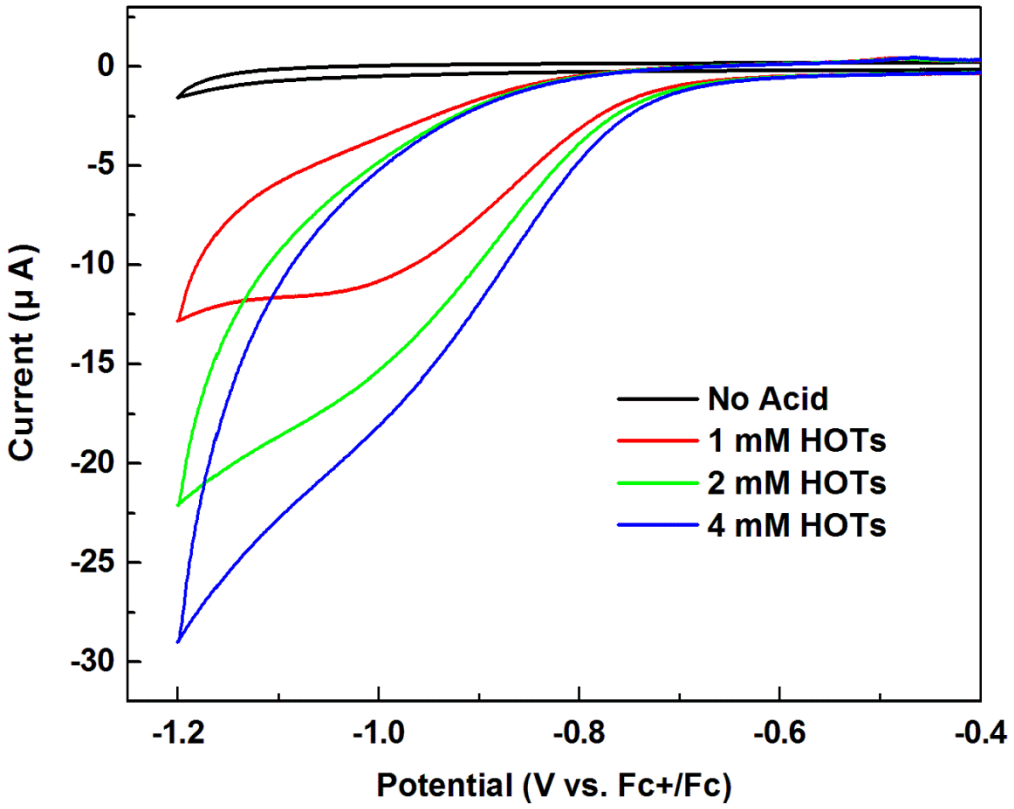

Figure A10. CV of $[Co(tpm)_2]\cdot 2BF_4$ in the presence of HOTs. Proton reduction is observed at high overpotentials, similar to that for **1**.

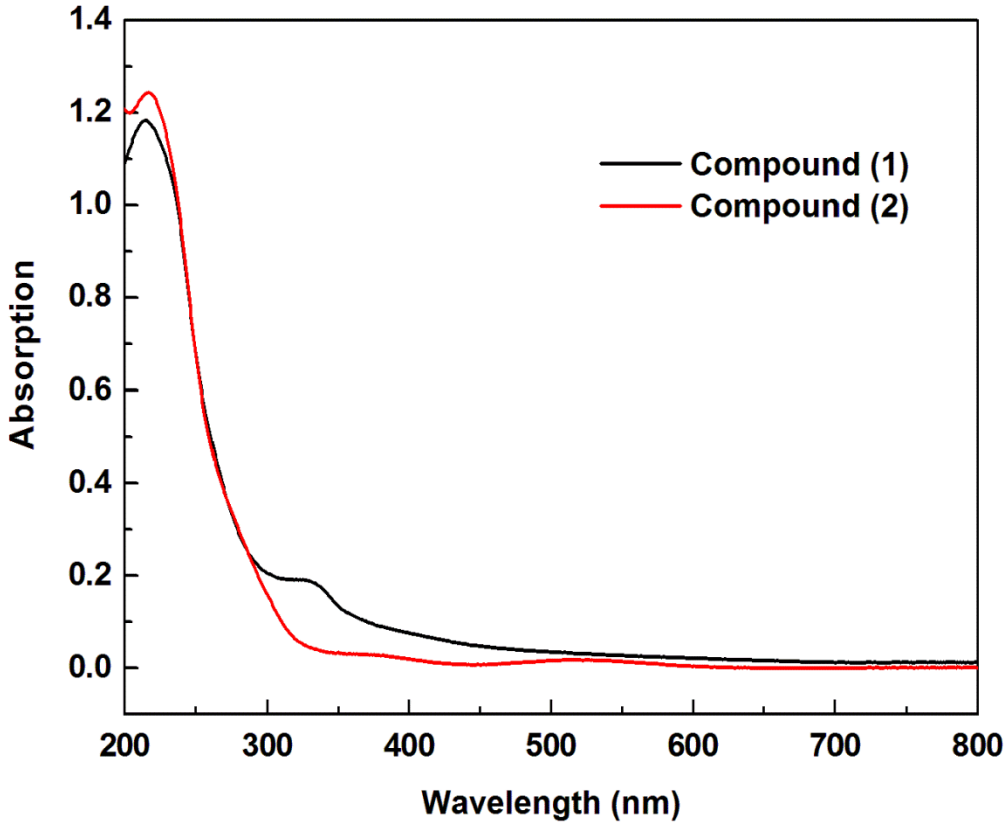

Figure A11. UV-vis spectra of compounds **1** and **2**.

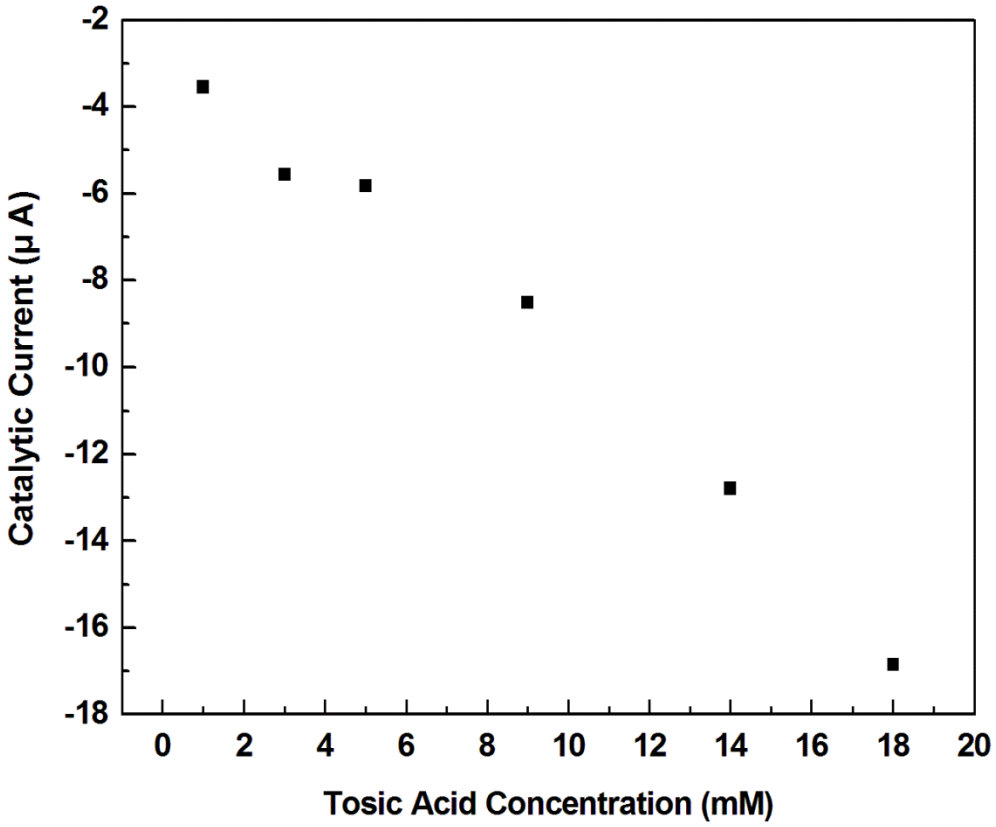

Figure A12. The catalytic current as a function of tosic acid concentration. A linear growth in current was observed.

Table A1. Crystal data and structure refinement for **1**.

Identification code	shelxl	
Empirical formula	C54 H102 B2 Co3 F8 O18	
Formula weight	1389.77	
Temperature	138(2) K	
Wavelength	0.71073 Å	
Crystal system	Triclinic	
Space group	P -1	
Unit cell dimensions	a = 9.938(2) Å	a= 102.448(4)°.
	b = 12.360(3) Å	b= 98.325(4)°.
	c = 15.263(4) Å	g = 105.752(4)°.
Volume	1720.3(7) $Å^3$	
Z	1	
Density (calculated)	1.34 Mg/m^3	
Absorption coefficient	0.798 mm^{-1}	
F(000)	733	
Crystal size	0.10 x 0.10 x 0.03 mm^3	
Theta range for data collection	1.40 to 25.42°.	
Index ranges	-11<=h<=11, -14<=k<=14, -18<=l<=18	
Reflections collected	39368	
Independent reflections	6275 [R(int) = 0.0930]	
Completeness to theta = 25.42°	99.0 %	
Absorption correction	Semi-empirical from equivalents	
Max. and min. transmission	0.9700 and 0.9047	
Refinement method	Full-matrix least-squares on F^2	
Data / restraints / parameters	6275 / 0 / 394	
Goodness-of-fit on F^2	1.021	
Final R indices [I>2sigma(I)]	R1 = 0.0656, wR2 = 0.1548	
R indices (all data)	R1 = 0.1107, wR2 = 0.1825	
Largest diff. peak and hole	0.837 and -0.709 e.$Å^{-3}$	

Table A2. Atomic coordinates (x 10^4) and equivalent isotropic displacement parameters (Å ^{2}x 10^3) for **1**. U(eq) is defined as one third of the trace of the orthogonalized U^{ij} tensor.

	x	y	z	U(eq)
C(1)	7382(6)	4515(4)	4789(4)	45(1)
C(2)	7043(5)	3476(4)	5172(3)	34(1)
C(3)	7305(5)	2363(4)	4732(3)	34(1)
C(4)	8917(5)	2602(5)	4826(4)	44(1)
C(5)	6537(6)	1931(4)	3724(3)	43(1)
C(6)	2986(6)	2566(5)	7642(4)	53(2)
C(7)	3874(5)	2311(4)	6961(4)	37(1)
C(8)	3219(5)	1745(4)	5953(3)	35(1)
C(9)	2739(6)	2639(5)	5539(4)	46(1)
C(10)	1972(5)	665(5)	5851(4)	44(1)
C(11)	9466(6)	2004(5)	8182(4)	49(2)
C(12)	8190(5)	1760(5)	7451(3)	35(1)
C(13)	7046(5)	575(4)	7132(3)	34(1)
C(14)	6483(6)	286(5)	7966(3)	43(1)
C(15)	7715(6)	-324(5)	6697(4)	46(1)
C(16)	1795(12)	527(10)	9486(6)	124(4)
C(17)	3064(12)	149(12)	9498(7)	150(5)
C(18)	2754(11)	-778(9)	8748(9)	141(5)
C(19)	1305(10)	-989(8)	8212(7)	105(3)
C(20)	7713(13)	5318(9)	10008(8)	137(4)
C(21)	6725(16)	4655(10)	10448(7)	139(5)
C(22)	6430(13)	3428(8)	9935(5)	126(4)
C(24)	7213(9)	6623(6)	7086(5)	81(2)
C(25)	7356(8)	7260(6)	8075(5)	70(2)
C(26)	5834(8)	6906(6)	8189(5)	72(2)
C(27)	5245(8)	5690(6)	7600(5)	69(2)
C(105)	7931(9)	4477(8)	9231(7)	120(4)
O(1)	6525(4)	3505(3)	5891(3)	54(1)
O(2)	6780(3)	1509(3)	5196(2)	30(1)
O(3)	5250(4)	2568(3)	7205(3)	56(1)

O(4)	4282(3)	1443(3)	5508(2)	30(1)
O(5)	7962(4)	2533(3)	7066(3)	53(1)
O(6)	5902(3)	612(3)	6480(2)	29(1)
O(9)	6009(5)	5591(4)	6891(3)	70(1)
O(10)	6833(6)	3447(4)	9092(3)	85(2)
O(11)	833(7)	-112(5)	8644(4)	109(2)
Co(1)	5000	0	5000	28(1)
Co(2)	6154(1)	2095(1)	6257(1)	30(1)
F(1)	9927(5)	4439(5)	13358(3)	108(2)
F(2)	7963(5)	3748(4)	12297(3)	102(2)
F(3)	9980(8)	4455(9)	11935(5)	218(5)
F(4)	9052(7)	5606(4)	12680(5)	160(3)
B(1)	9222(8)	4548(7)	12560(5)	55(2)

Table A3. Bond lengths [Å] and angles [°] for **1**.

C(1)-C(2)	1.500(7)
C(2)-O(1)	1.276(6)
C(2)-C(3)	1.502(7)
C(3)-O(2)	1.421(5)
C(3)-C(5)	1.523(7)
C(3)-C(4)	1.527(7)
C(6)-C(7)	1.495(7)
C(7)-O(3)	1.294(6)
C(7)-C(8)	1.510(7)
C(8)-O(4)	1.424(6)
C(8)-C(10)	1.516(7)
C(8)-C(9)	1.532(7)
C(11)-C(12)	1.476(7)
C(12)-O(5)	1.277(6)
C(12)-C(13)	1.518(7)
C(13)-O(6)	1.416(6)
C(13)-C(15)	1.526(7)
C(13)-C(14)	1.536(7)
C(16)-O(11)	1.410(10)
C(16)-C(17)	1.457(13)
C(17)-C(18)	1.363(12)
C(18)-C(19)	1.475(12)
C(19)-O(11)	1.374(9)
C(20)-C(21)	1.441(14)
C(20)-C(105)	1.484(12)
C(21)-C(22)	1.477(13)
C(22)-O(10)	1.405(9)
C(24)-O(9)	1.432(7)
C(24)-C(25)	1.511(9)
C(25)-C(26)	1.503(10)
C(26)-C(27)	1.481(9)
C(27)-O(9)	1.412(7)
C(105)-O(10)	1.385(9)

O(1)-Co(2)	1.902(4)
O(2)-Co(2)	1.888(3)
O(2)-Co(1)	2.124(3)
O(3)-Co(2)	1.882(4)
O(4)-Co(2)	1.895(3)
O(4)-Co(1)	2.132(3)
O(5)-Co(2)	1.894(4)
O(6)-Co(2)	1.892(3)
O(6)-Co(1)	2.188(3)
Co(1)-O(2)#1	2.124(3)
Co(1)-O(4)#1	2.132(3)
Co(1)-O(6)#1	2.188(3)
Co(1)-Co(2)#1	2.7036(8)
Co(1)-Co(2)	2.7036(8)
F(1)-B(1)	1.367(8)
F(2)-B(1)	1.310(8)
F(3)-B(1)	1.303(9)
F(4)-B(1)	1.341(9)

O(1)-C(2)-C(1)	121.1(5)
O(1)-C(2)-C(3)	117.2(4)
C(1)-C(2)-C(3)	121.7(4)
O(2)-C(3)-C(2)	109.1(4)
O(2)-C(3)-C(5)	109.7(4)
C(2)-C(3)-C(5)	109.8(4)
O(2)-C(3)-C(4)	109.1(4)
C(2)-C(3)-C(4)	108.5(4)
C(5)-C(3)-C(4)	110.7(4)
O(3)-C(7)-C(6)	121.6(5)
O(3)-C(7)-C(8)	116.4(4)
C(6)-C(7)-C(8)	122.0(5)
O(4)-C(8)-C(7)	108.9(4)
O(4)-C(8)-C(10)	110.4(4)
C(7)-C(8)-C(10)	109.2(4)
O(4)-C(8)-C(9)	108.5(4)

C(7)-C(8)-C(9)	108.1(4)
C(10)-C(8)-C(9)	111.6(4)
O(5)-C(12)-C(11)	122.4(5)
O(5)-C(12)-C(13)	116.0(4)
C(11)-C(12)-C(13)	121.6(5)
O(6)-C(13)-C(12)	109.5(4)
O(6)-C(13)-C(15)	110.1(4)
C(12)-C(13)-C(15)	108.4(4)
O(6)-C(13)-C(14)	109.1(4)
C(12)-C(13)-C(14)	108.5(4)
C(15)-C(13)-C(14)	111.2(4)
O(11)-C(16)-C(17)	107.0(8)
C(18)-C(17)-C(16)	106.9(9)
C(17)-C(18)-C(19)	109.4(9)
O(11)-C(19)-C(18)	105.9(7)
C(21)-C(20)-C(105)	107.3(9)
C(20)-C(21)-C(22)	104.5(9)
O(10)-C(22)-C(21)	106.7(8)
O(9)-C(24)-C(25)	105.7(5)
C(26)-C(25)-C(24)	102.2(6)
C(27)-C(26)-C(25)	102.7(6)
O(9)-C(27)-C(26)	107.7(6)
O(10)-C(105)-C(20)	105.6(8)
C(2)-O(1)-Co(2)	114.5(4)
C(3)-O(2)-Co(2)	113.6(3)
C(3)-O(2)-Co(1)	139.2(3)
Co(2)-O(2)-Co(1)	84.53(12)
C(7)-O(3)-Co(2)	114.9(4)
C(8)-O(4)-Co(2)	113.2(3)
C(8)-O(4)-Co(1)	142.1(3)
Co(2)-O(4)-Co(1)	84.11(12)
C(12)-O(5)-Co(2)	115.5(3)
C(13)-O(6)-Co(2)	113.7(3)
C(13)-O(6)-Co(1)	139.9(3)
Co(2)-O(6)-Co(1)	82.65(11)

C(27)-O(9)-C(24)	109.2(5)
C(105)-O(10)-C(22)	107.7(6)
C(19)-O(11)-C(16)	109.8(7)
O(2)#1-Co(1)-O(2)	180.00(13)
O(2)#1-Co(1)-O(4)#1	74.56(12)
O(2)-Co(1)-O(4)#1	105.44(12)
O(2)#1-Co(1)-O(4)	105.44(12)
O(2)-Co(1)-O(4)	74.56(12)
O(4)#1-Co(1)-O(4)	180.00(17)
O(2)#1-Co(1)-O(6)#1	73.98(11)
O(2)-Co(1)-O(6)#1	106.02(11)
O(4)#1-Co(1)-O(6)#1	73.67(12)
O(4)-Co(1)-O(6)#1	106.33(12)
O(2)#1-Co(1)-O(6)	106.02(11)
O(2)-Co(1)-O(6)	73.98(11)
O(4)#1-Co(1)-O(6)	106.33(12)
O(4)-Co(1)-O(6)	73.67(12)
O(6)#1-Co(1)-O(6)	180.000(1)
O(2)#1-Co(1)-Co(2)#1	44.03(8)
O(2)-Co(1)-Co(2)#1	135.97(8)
O(4)#1-Co(1)-Co(2)#1	44.21(8)
O(4)-Co(1)-Co(2)#1	135.79(8)
O(6)#1-Co(1)-Co(2)#1	43.96(8)
O(6)-Co(1)-Co(2)#1	136.04(8)
O(2)#1-Co(1)-Co(2)	135.97(8)
O(2)-Co(1)-Co(2)	44.03(8)
O(4)#1-Co(1)-Co(2)	135.79(8)
O(4)-Co(1)-Co(2)	44.21(8)
O(6)#1-Co(1)-Co(2)	136.04(8)
O(6)-Co(1)-Co(2)	43.96(8)
Co(2)#1-Co(1)-Co(2)	180.0
O(3)-Co(2)-O(2)	171.35(16)
O(3)-Co(2)-O(6)	92.21(16)
O(2)-Co(2)-O(6)	86.71(13)
O(3)-Co(2)-O(5)	93.28(18)

O(2)-Co(2)-O(5)	95.17(16)
O(6)-Co(2)-O(5)	85.00(16)
O(3)-Co(2)-O(4)	85.45(16)
O(2)-Co(2)-O(4)	85.92(14)
O(6)-Co(2)-O(4)	86.30(13)
O(5)-Co(2)-O(4)	171.16(16)
O(3)-Co(2)-O(1)	96.03(18)
O(2)-Co(2)-O(1)	85.09(16)
O(6)-Co(2)-O(1)	171.76(16)
O(5)-Co(2)-O(1)	94.88(17)
O(4)-Co(2)-O(1)	93.96(15)
O(3)-Co(2)-Co(1)	121.65(12)
O(2)-Co(2)-Co(1)	51.44(9)
O(6)-Co(2)-Co(1)	53.38(9)
O(5)-Co(2)-Co(1)	122.94(13)
O(4)-Co(2)-Co(1)	51.67(10)
O(1)-Co(2)-Co(1)	120.95(12)
F(3)-B(1)-F(2)	111.5(8)
F(3)-B(1)-F(4)	106.4(7)
F(2)-B(1)-F(4)	109.3(6)
F(3)-B(1)-F(1)	109.8(7)
F(2)-B(1)-F(1)	108.9(6)
F(4)-B(1)-F(1)	110.9(7)

Symmetry transformations used to generate equivalent atoms:

#1 -x+1,-y,-z+1

Table A4. Anisotropic displacement parameters (Å ^{2}x 10^3) for **1**. The anisotropic displacement factor exponent takes the form: $-2p^2[h^2a^{*2}U^{11} + ... + 2 h k a^* b^* U^{12}]$

	U^{11}	U^{22}	U^{33}	U^{23}	U^{13}	U^{12}
C(1)	58(4)	27(3)	48(3)	12(2)	12(3)	5(3)
C(2)	32(3)	30(3)	36(3)	10(2)	7(2)	3(2)
C(3)	31(3)	27(3)	41(3)	14(2)	8(2)	2(2)
C(4)	38(3)	34(3)	56(3)	11(3)	17(3)	6(2)
C(5)	51(3)	35(3)	38(3)	11(2)	12(3)	4(3)
C(6)	52(4)	49(4)	57(4)	5(3)	23(3)	13(3)
C(7)	35(3)	24(3)	54(3)	8(2)	17(2)	10(2)
C(8)	34(3)	34(3)	40(3)	9(2)	13(2)	15(2)
C(9)	47(3)	42(3)	59(4)	16(3)	12(3)	25(3)
C(10)	32(3)	38(3)	57(3)	8(3)	11(3)	7(2)
C(11)	37(3)	48(3)	54(3)	13(3)	0(3)	7(3)
C(12)	32(3)	38(3)	39(3)	15(2)	8(2)	13(2)
C(13)	30(3)	32(3)	39(3)	11(2)	2(2)	8(2)
C(14)	42(3)	42(3)	39(3)	14(2)	4(2)	3(3)
C(15)	46(3)	37(3)	51(3)	7(3)	1(3)	19(3)
C(16)	136(9)	156(10)	78(6)	-11(6)	2(6)	87(8)
C(17)	125(9)	236(15)	84(7)	-11(8)	-11(6)	109(10)
C(18)	85(7)	115(9)	184(12)	-40(8)	3(7)	45(6)
C(19)	102(7)	82(6)	118(7)	-7(5)	8(6)	42(6)
C(20)	143(10)	72(7)	131(9)	-38(6)	7(8)	-6(6)
C(21)	216(15)	135(10)	77(7)	11(7)	17(8)	95(10)
C(22)	218(12)	95(7)	51(5)	15(5)	42(6)	26(7)
C(24)	102(6)	41(4)	97(6)	11(4)	46(5)	14(4)
C(25)	84(5)	39(4)	76(5)	10(3)	16(4)	8(4)
C(26)	98(6)	49(4)	73(5)	10(3)	34(4)	24(4)
C(27)	67(4)	62(4)	74(5)	4(4)	20(4)	23(4)
C(105)	63(5)	86(6)	151(9)	-35(6)	12(5)	-14(5)
O(1)	50(2)	45(2)	61(3)	14(2)	7(2)	10(2)
O(2)	30(2)	24(2)	38(2)	11(1)	12(1)	8(1)
O(3)	55(3)	42(2)	68(3)	16(2)	16(2)	11(2)

O(4)	25(2)	25(2)	41(2)	8(1)	8(1)	7(1)
O(5)	51(2)	52(3)	54(2)	10(2)	15(2)	13(2)
O(6)	29(2)	23(2)	35(2)	10(1)	5(1)	6(1)
O(9)	82(3)	43(3)	81(3)	2(2)	31(3)	19(2)
O(10)	103(4)	76(3)	44(3)	-4(2)	5(3)	-4(3)
O(11)	114(5)	101(4)	100(4)	-13(4)	-19(4)	68(4)
Co(1)	26(1)	22(1)	35(1)	7(1)	7(1)	5(1)
Co(2)	29(1)	22(1)	36(1)	6(1)	7(1)	5(1)
F(1)	102(4)	126(4)	99(3)	43(3)	2(3)	44(3)
F(2)	79(3)	61(3)	139(4)	32(3)	5(3)	-15(2)
F(3)	185(7)	430(14)	209(7)	229(9)	159(6)	193(8)
F(4)	156(5)	51(3)	222(7)	38(4)	-73(5)	7(3)
B(1)	43(4)	49(4)	69(5)	25(4)	4(4)	8(3)

Table A5. Hydrogen coordinates (x 10^4) and isotropic displacement parameters (Å ^{2}x 10^3) for **1**.

	x	y	z	U(eq)
H(1A)	6598	4416	4279	68
H(1B)	8271	4586	4567	68
H(1C)	7500	5221	5271	68
H(4A)	9394	2898	5478	65
H(4B)	9283	3185	4501	65
H(4C)	9107	1878	4560	65
H(5A)	6592	1151	3462	64
H(5B)	6994	2468	3387	64
H(5C)	5530	1896	3672	64
H(6A)	2353	1832	7693	80
H(6B)	2409	3030	7437	80
H(6C)	3615	3004	8243	80
H(9A)	3574	3311	5596	69
H(9B)	2057	2898	5868	69
H(9C)	2279	2280	4888	69
H(10A)	1598	255	5198	66
H(10B)	1215	893	6113	66
H(10C)	2297	147	6175	66
H(11A)	10179	2733	8190	73
H(11B)	9874	1363	8062	73
H(11C)	9191	2079	8778	73
H(14A)	6139	913	8265	65
H(14B)	7256	211	8403	65
H(14C)	5693	-451	7764	65
H(15A)	6971	-1081	6432	68
H(15B)	8443	-397	7168	68
H(15C)	8162	-72	6212	68
H(16A)	1355	372	10007	149
H(16B)	2053	1373	9538	149

H(17A)	3894	790	9469	180
H(17B)	3299	-83	10069	180
H(18A)	2802	-1481	8947	169
H(18B)	3464	-615	8362	169
H(19A)	1337	-964	7571	126
H(19B)	663	-1761	8203	126
H(20A)	8635	5754	10450	164
H(20B)	7316	5884	9781	164
H(21A)	5834	4873	10406	166
H(21B)	7158	4787	11104	166
H(22A)	6989	3045	10283	151
H(22B)	5399	2993	9831	151
H(24A)	7047	7113	6673	97
H(24B)	8091	6418	7004	97
H(25A)	7979	7006	8500	84
H(25B)	7746	8115	8178	84
H(26A)	5792	6939	8838	87
H(26B)	5310	7409	7974	87
H(27A)	5357	5138	7967	83
H(27B)	4214	5507	7336	83
H(10D)	7884	4762	8673	143
H(10E)	8874	4359	9386	143

References

(A1) Bard, A. J., Faulkner, L. R. *Electrochemical Methods: Fundamentals and Applications 2nd Ed.*, Wiley, New York, 2001.

(A2) Sathrum, A. J., Kubiak, C. P. *J. Phys. Chem. Lett.*, **2011**, 2, 2372.